JEBEL TAYS OPHIOLITIC THRUST SHEET, SAUDI ARABIA: TECTONIC SETTING, PETROGENESIS AND GEOCHRONOLOGICAL FRAMEWORK

A thesis presented by Grant Michael Cox

to

The Discipline of Geology and Geophysics
in partial fulfilment of the requirements
for the degree of Bachelor of Science (Honours)

University of Adelaide
Adelaide, South Australia.

October, 2009

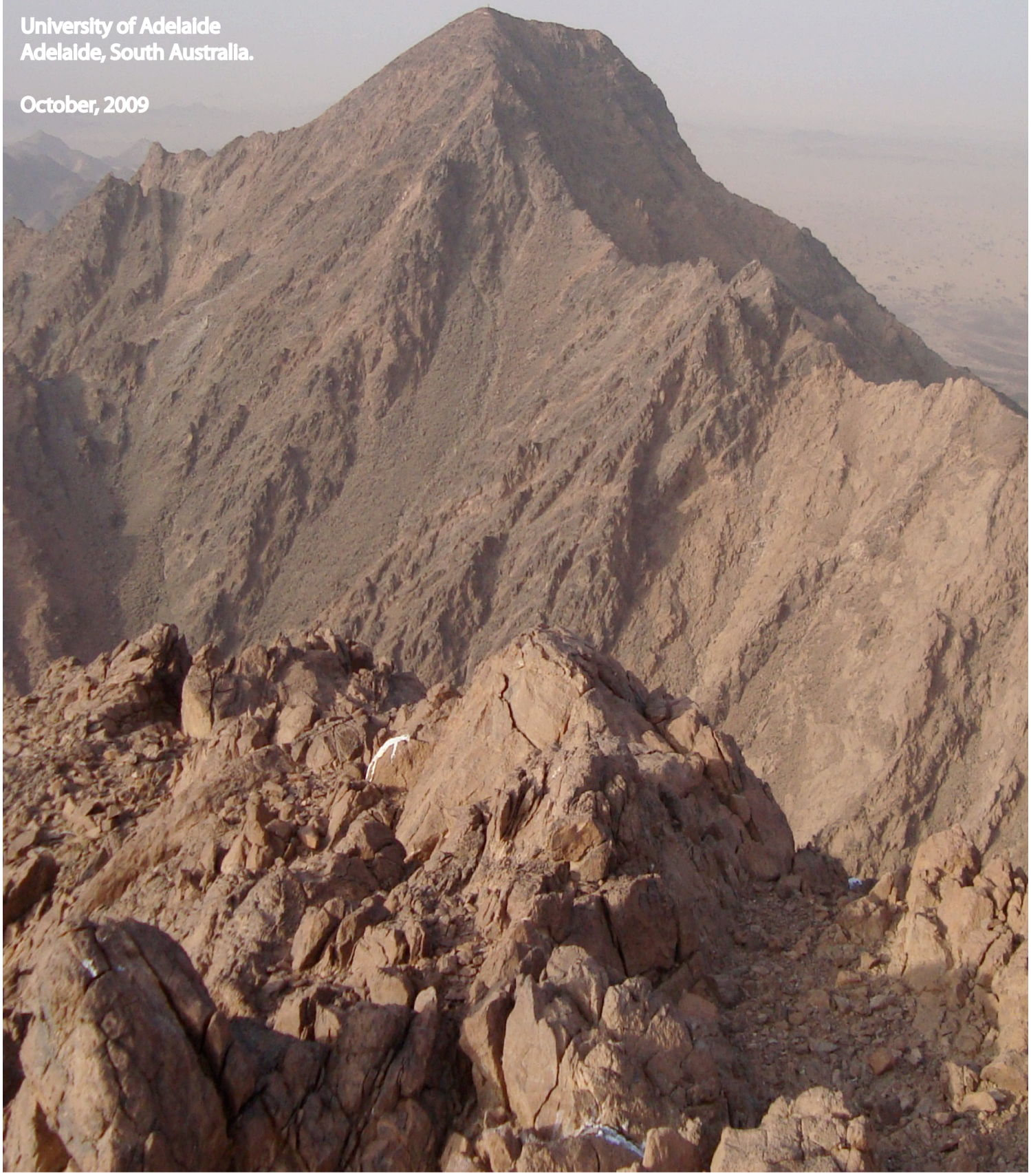

Cover Art:
Photo of the summit of Jebel Tays, rocks in foreground are massive carbonates while those in background are serpentinised ultramafics.

Abstract

The Arabian Nubian Shield (ANS) records multiple episodes of terrane amalgamation associated with the closure of the Mozambique Ocean and the amalgamation of Gondwana. Evidence for such amalgamation events are recorded by repeated ophiolite decorated sutures across the ANS. The Jebel Tays ophiolite is situated in the eastern portion of the ANS, within the Ad Dawadimi basin and surrounded by the Abt schist. This basin separates the Afif and Ar Rayn arc terranes and represents one of the last terrane amalgamation events affecting the exposed ANS. I identify mafic magmatism associated with Jebel Tays as a low titanium island arc tholeiite with forearc affinity (boninitic), this is in contrast to the island arc tholeiite magmatism of the nearby Halaban ophiolite. Furthermore, I place robust zircon ages on mafic magmatism of 678 ± 5.1 Ma for the gabbros of Jebel Tays and 674.4 ± 5.7 Ma for the Halaban ophiolite. Based on the stratigraphy and structure of Jebel Tays and the sub-greenschist nature of the thrust contacts I propose that Jebel Tays represents a forearc ophiolitic thrust sheet. Its obduction was associated with extensive serpentinite mud volcanism within a forearc environment associated with a west dipping subducting slab. From detrital zircons obtained from the Abt Formation I constrain deposition of the Ad Dawadimi basin sediments to ca 600 Ma making them Ediacaran in age, a date that coincides with a new LA-ICP-MS monazite metamorphic age of 599.8 ± 5.8 Ma obtained from a trondhjemite that cross cuts the Jebel Tays body, which is in agreement with previously published $^{40}Ar/^{39}Ar$ ages which I interpret as a metamorphic age associated with final basin closure and the amalgamation of the Afif and Ar Rayn Terranes.

Acknowledgements

Thanks go to the Saudi Geological Survey and especially Fayek Kattan, Nawaf N. Al Remee, Wadee A. Kashghari and Mubarak Al Nahdi, without their help none of this project would have been possible. Alan Collins, John Foden and Galen Halverson my principal supervisors were invaluable in providing research guidance and advise and their review of this manuscript improved it immensely. Benjamin Wade and Angus Netting of Adelaide Microscopy along with David Bruce and John Stanley of Adelaide University helped with the geochemical analysis. Thankyou to Martin Hand, Karin Barovich, Benjamin Wade and David Kelsey whose advise was sought and was graciously given. Lastly thankyou to David Nettle and Christopher Lewis for the many conversations about the regional geology of the area, which helped to place this research into a wider geological context.

Table of Contents

1 INTRODUCTION

The Arabian portion of the Arabian Nubian Shield (ANS) (Fig. 1) has been shown through a combination of isotope chemistry and geological relations between fault bounded blocks to be comprised of 16 accreted terranes. Based on Pb, Sr, Nd and O isotopes, and U-Pb geochronologies, a number of workers have managed to simplify the various ANS terranes into the western and eastern arc terranes, both of which are of oceanic affinity (Stoeser and Camp, 1985; Stoeser and Frost, 2006). Many of the observed terrane sutures are ophiolite decorated and their strike changes dramatically across the ANS (Fig. 1), from east-west orientated in the far western Shield to north-south orientated in the eastern Shield. The dominant Neoproterozoic ages of the Shield correlates with the closure of the Mozambique Ocean and the amalgamation of Gondwana (Collins and Pisarevsky, 2005). Based on a transition from Type I to Type II Pb signatures, the Hulayfah-Ad Dafinah fault (Fig. 1) which separates the western and eastern arc terranes, is considered a suture of special importance, if not the principle Mozambique Ocean suture (Stoeser and Frost, 2006).

This study focuses on the ophiolitic rocks of the Ad Dawadimi basin, specifically ultramafic and mafic rocks of Jebel Tays (Mount Goat), a locally prominent out cropping of hills within the southern part of the basin. The Ad Dawadimi basin is situated in the far eastern portion of the Shield and separates the Afif and Ar Rayn Terranes. The eastern margin of the basin is delineated by the Al Amar fault zone which separates the Ad Dawadimi from the Ar Rayn Terrane. In the west the basin is separated from the Afif Terrane by the extensively ophiolite decorated Halaban-Zarghat fault zone. The basin itself is composed of rocks of the Abt Formation described as pelitic schist and greywacke, ophiolitic mélange zones and syn and post orogenic granites (Delfour, 1979). The ANS youngs from west to east across the Shield (Johnson, 2006; Johnson and Kattan, 2008), thus the Ad Dawadimi preserves one of the last accretion events to affect the exposed Shield.

Previous work within the eastern part of the ANS is limited. Al-Shanti & Gass (1983) investigated the so called mélange zones of the Ad Dawadimi basin including Jebel Tays and proposed that the rocks of Jebel Tays had forearc characteristics and attributed this magmatism to arc splitting (Afif and Ar Rayn Terranes) and back-arc basin opening. Later work on the trondhjemite that intrudes Jebel Tays produced a $^{87}Rb/^{86}Sr$ age of 620 ± 40 Ma and its genesis was attributed to the partial melting of lower crustal mafics at the base of an oceanic island arc (Al-Shanti et al., 1984).

Regionally, research has focussed on identifying the larger tectonic setting of the Ad Dawadimi basin and providing a robust geochronological framework for the area. Based on ca 680 Ma and 600 Ma $^{40}Ar/^{39}Ar$ ages from the metamorphic sole of the Halaban ophiolite, Al-Saleh *et al.* (1998) and Al-Saleh *et al.* (2001b) proposed basin closure by 680 Ma and collision of the Arabian craton with a large continental landmass east of the Ar Rayn Terrane at 600 Ma.

Laser ablation inductively coupled mass spectrometry (LA-ICP-MS) has been used to obtain U-Pb ages on zircons and monazites obtained from the principal igneous rocks exposed at Jebel Tays and the Halaban ophiolite. Furthermore, the geochemistry of the exposed rocks of Jebel Tays is obtained through a combination of trace element solution inductively coupled mass spectrometry (ICP-MS), major and minor element X-Ray fluorescence spectroscopy (XRF), Sm/Nd isotope systematics via thermal ionisation mass spectroscopy (TIMS) and $\delta^{13}C$ values of exposed carbonates via isotope ratio mass spectroscopy (IRMS). Here in I present a detailed structural, geochemical and geochronological framework for protolith emplacement and obduction of the Jebel Tays ophiolite and constrain the depositional age of the Abt Formation to provide greater insight into how this area relates to the amalgamation of the Afif and Ar Rayn Terranes and implications for the amalgamation of Gondwana.

2 ANALYTICAL METHODS

2.1 Major Element Geochemistry

Major element analysis (SiO_2, MgO, Fe_2O_3, MnO, CaO, TiO_2, Na_2O, K_2O and P_2O_5) was carried out on fused glass disks. Fused disks were prepared from rock samples cut so as to remove weathered surfaces and then cut into approximately 5 cm^3 fragments using a diamond bladed rock saw. The rocks were crushed to rock chips on a standard iron jawed crusher. The resulting chips where milled in a tungsten carbide mill (this mill is a possible source of Ta contamination) until the powder could pass a 75 μm mesh. Approximately 6 g of powder was heated to 130°C for 4 hours to remove free water, the sample was then weighed and ignited at 960°C for 3 hours. Loss on ignition was calculated. Approximately 1 g of the ignited sample was combined with ca 4 g of a lithium borate flux and fused into a glass disk in a Pt/Au crucible and mold. The resulting fused glass disk was analysed on a Phillips PW1480 XRF spectrometer. XRF analysis of Sr and Zr was carried out on pressed pellets prepared from ca 6 g of non-ignited sample powder combined with 0.8 mL of an EtOH/polyvinyl acetate binder. Reproducibility of the results was measured against the JB-2 international standard and VHG house standard. Mean totals across 46 samples was 99.08%

2.2 Trace Element Geochemistry

Rock powder (see section 2.1) was weighed to ca 0.05g in cleaned teflon bombs, double distilled HF (4 mL / 25M) and HNO_3 (2 mL / 7M) was added and evaporated to dryness. Further HF (4 mL / 25M) and HNO_3 (2 mL / 7M) were added, the bombs were sealed in steel pressure cylinders and heated to 190°C for 120 hours then allowed to cool and evaporated to dryness. HNO_3 (6 mL / 7M) was added and pressure heated at 190°C for a further 48 hours and evaporated to dryness. The resulting precipitate was dissolved in HNO_3 (10mL / 0.5M) and split into 2 x 5 mL aliquots. An in-house basalt standard (TASBAS) and a procedural blank were prepared in an identical manner and

the resulting solutions were analysed on a Agilent 7500 ICP-MS. Element counts per second (cps) were converted to concentration (ppm) through the fitting of measured cps to a calibration curve constructed from series of multi-element standard solutions. Corrections to measured cps were made through the use of Indium as an internal standard and through the bracketing of samples by the TASBAS in-house standard. Reproducibility of reported elements was measured against the TASBAS in-house standard as well as the Basalt Hawaiian Volcanic Observatory (BHVO-1) and Cody Shale (SCo-1) international standards, results for these international standards can be found in appendix 11.8 and 11.9.

2.3 Radiogenic Isotope Geochemistry

Rock powder (see section 2.1) was weighed (ca 0.02 g) into cleaned teflon bombs, double distilled HF (4 mL / 25M) and HNO_3 (2 mL / 7M) was added and evaporated to dryness. Further HF (4 mL / 25M) and HNO_3 (2 mL / 7M) was added, the bombs were sealed in steel pressure cylinders and heated to 190°C for 120 hours then allowed to cool and evaporated to dryness. HCl (6 mL / 6M) was added and pressure heated at 190°C for a further 48 hours and evaporated to dryness. Nd and Sm were separated via column chromatography. Nd and Sm concentrations along with $^{143}Nd/^{144}Nd$, $^{150}Nd/^{144}Nd$, $^{147}Sm/^{149}Sm$ and $^{152}Sm/^{149}Sm$ were calculated by isotope dilution via the method described in Wade *et al.* (2008). Isotopic ratios were measured on a Finigan MAT 262 thermal ionisation mass spectrometer. The Nd international standard JNDi-1 (Tanaka et al., 2000) returned a mean value of 0.51226464 ± 0.000176154 (n=5) while the TASBAS in-house standard returned a value of 0.5129692 (n=1). Blanks showed negligible Nd. Epsilon Nd values were calculated based on the $^{143}Nd/^{144}Nd$ and $^{147}Sm/^{144}Nd$ depleted mantle values of Goldstein *et al. (1984)*.

2.4 Stable Isotope Geochemistry

Carbonate rocks were cut and the clean surfaces micro-drilled to produce a fine powder, approximately 4 mg of powder was loaded into cleaned tin bombs and flash combusted in a Fisons VG Isochrom Elemental Analyser at 1330°C in a quartz combustion tube packed with chromium oxide and silvered cobaltous oxide separated by quartz chips. The resulting gas stream was passed through a copper filled reducing column, the gas species were separated in a gas chromatography column and passed through a magnesium perchlorate water trap. The isotopic composition of the resulting purified CO_2 gas stream was measured on a Fisons VG Optima isotope ratio mass spectrometer (IRMS) operating in continuous flow mode. The resulting isotopic measurements were corrected for machine fractionation by the measurement of several in-house standards (UA-Sucrose, UA-Glycine, UA-Glutamic Acid and ANUP3-$CaCO_3$) as well as the NIST/NBS lithium carbonate standard (L-SVEC) that span the $\delta^{13}C$ range of -2.40 to -46.60. The accepted $\delta^{13}C$ of these standards were plotted against measured $\delta^{13}C$, a linear regression of this data produced a R^2 value better than 0.99 and the sample $\delta^{13}C$ were corrected based on this linear regression equation. All $\delta^{13}C$ values are reported with respect to the Vienna Pee Dee Belemnite standard as per mil deviations.

2.5 Geochronology

Whole rock samples where crushed to a medium to coarse powder and sieved into three fractions of ≤75 μm , ≥75 μm - ≤425 μm, and a ≥425 μm. The ≥75 μm - ≤425 μm fraction was panned to concentrate zircons and/or monazites and the resulting heavy fraction underwent a methylene iodine heavy liquid separation to produce a mineral fraction containing only those minerals with a density greater than 3.3 g cm^{-3}. The resulting heavy liquid separate was washed with acetone and dried. Zircons and monazites were then hand picked and mounted in an epoxy resin (tradename ~ Epoxicure). The epoxy mounts were polished to expose the mounted minerals, carbon

coated and imaged via cathodoluminescence and back scattered electrons (acc. V 12kV, spot size 7) on a Phillips XL20 scanning electron microscope.

Ablation of zircons and monazites was performed with a New Wave Research Nd:YAG laser (zircon: spot size = 30 μm / frequency = 5Hz / intensity = 75%) (monazite: spot size = 15 μm / frequency = 5Hz / intensity = 75%) with isotope ratios measured ($^{206}Pb/^{238}U$, $^{207}Pb/^{235}U$, $^{207}Pb/^{206}Pb$ and $^{208}Pb/^{232}Th$) on an Agilent 7500 series ICP-MS. Ablation and machine fractionation was corrected for against the known GJ zircon (Jackson et al., 2004) and MAdel monazite standards (TIMS normalisation data: $^{207}Pb/^{206}Pb$ = 490.7 Ma, $^{206}Pb/^{238}U$ = 514.8 Ma and $^{207}Pb/^{235}U$ = 510.4 Ma (Payne et al., 2008)). Age calculations of individual zircons and monazites utilised the real-time correction program 'Glitter' (Jackson et al., 2004). Concordia diagrams, weighted average ages and probability distribution plots where constructed using the ISOPLOT software (Ludwig, 2009). Crystallisation ages are calculated from $^{206}Pb/^{238}U$ ages. With respect to detrital data $^{206}Pb/^{207}Pb$ ages are used for detrital zircons older than 1Ga and $^{206}Pb/^{238}U$ used for detrital zircons younger than 1Ga.

3 STRATIGRAPHY & STRUCTURE

3.1 Jebel Tays Stratigraphy

The ultramafic/mafic complex centred around the locally prominent peak of Jebel Tays trends north-south and has the approximate dimensions of 4 km in width by 27 km in length and covers an area of approximately 108 km^2 most of which is covered by Quaternary regolith. Detailed descriptions of the observed stratigraphy are detailed in Table 1.

Table 1. Descriptions of the major identified lithologies of Jebel Tays

Jebel Tays Trondhjemite Intrusive (plutonic) rock found cross cutting both mafic and ultramafic sequences. Medium grey in colour and dominated by plagioclase, quartz and lesser amounts of epidote. Dated at 632 ± 8.0 Ma (this study).
Spine Gabbro These gabbros are named from the local Bedouin tradition of referring to the hills that these gabbros form as the spine of Tays. These gabbros are almost exclusively surrounded by serpentinite and range from isotropic to pervasively foliated and exhibit minor to moderate serpentinite alteration. Gabbros are composed of hornblende, plagioclase and olivine and show a sub-ophitic texture. These gabbros are dated at 678 ± 5.1 Ma (this study). Gabbros are cross cut by mafic dykes of boninitic affinity and the plutonic trondhjemite.
Serpentinised Ultramafics In the west and in the lower sections of Jebel Tays the serpentinite occurs as an mélange like body with serpentinite boulders and cobbles along with basalt clasts in a sheared serpentinite mud matrix interpreted as classic serpentinite mud volcanism. Elsewhere serpentinite is generally fine grained and displays classic snake skin texture and ranges from massive to highly sheared. Rare cumulates include amphibolite and harzburgite. Ultramafics are cross cut by mafic dykes of boninitic affinity and the plutonic trondhjemite.
Carbonates Orange massive carbonates composed of magnesite, calcite and quartz formed exclusively on serpentinised ultramafics. Carbonates cut by coarse euhedral carbonate veins.
Fluid Flow Zone Discrete zone of pseudomorphed euhedral pyrite developed in serpentinite and carbonate.
Abt Formation East of Jebel Tays the Abt Formation is a fine grained pelitic schist with interbeds of cobble to pebbly conglomerate, contains a prominent steeply dipping foliation that is co-incident with bedding. In the west the Abt Formation is a calcareous silt which grades to silt towards the west. Graded bedding east of Jebel Tays suggest formation youngs to the west. Metamorphosed up to greenschist facies.

The northern part of the mapped area (that part north of latitude 23° 04' N) is most varied and is dominated by serpentinite composed of larger serpentinised boulders, cobbles and pebbles in a fine grained serpentinised mud (Fig. 2). Originally this mélange like lithology was thought to be restricted to a discrete zone east of Jebel Tays (Al-Shanti and Gass, 1983) but the

same lithology can be seen in the steep gorges that extend from the summit of Jebel Tays. These serpentinite zones enclose both fine-grained massive and sheared serpentinised rocks and lesser amounts of isotropic and sheared gabbro and basalt blocks. The gabbros strike broadly north-south and serpentinite is generally found at the base of these outcrops. Carbonates are also prominent in this northern region and form the steep escarpments of Jebel Tays and form exclusively on top of serpentinite. Intruding all of the above serpentinites, gabbros and carbonates is an isotropic trondhjemite, two major plutonic intrusions are mapped. The major part of this body intrudes directly below the summit of Jebel Tays, this body has fine-grained chilled margins and a large sunken roof pendent can be observed (Fig. 2) indicating that this is indeed the upper most portion of this intrusive body.

Unlike in the north, the southern area is dominated by isotropic and gneissic gabbros that form locally prominent hills, serpentinite can be found at the base of many of these outcrops but is often obscured by scree and Quaternary cover. The carbonates found in the north are totally lacking and the trondhjemite intrusion has only limited surface expression. The lack of serpentinite and the lower aspect of these outcrops are most likely due to the lack of carbonate cover that has provided a more resistant cap to the serpentinite exposures seen in the north. Jebel Tays is unrewarding in terms of igneous stratigraphy and while Jebel Tays has been mapped regionally as rocks of ophiolitic origin (Delfour, 1979), no Penrose type stratigraphy (Anonymous, 1972) is observed.

Immediately to the east and west of Jebel Tays are meta-sedimentary rocks of the Abt Formation. Those exposed in the east grade from a conglomerate composed of well rounded elongated cobble-sized sub-volcanic clasts (as evidenced by graphic intergrowth of quartz and alkali feldspar) and rarer angular carbonate clasts set within a fine grained silt matrix that grades to a pebbly conglomerate and then into siltstone immediately in structural contact with the ultramafic/mafic rocks of Jebel Tays. The Abt Formation contains a

prominent fabric that is parallel to bedding, normal grading suggests younging is to the west, and the presence of chlorite and muscovite forming pressure shadows around cobble clasts (Fig. 3B) is evidence for metamorphism up to low greenschist facies. This lithology contrasts with the Abt Formation in the west which grades from a highly calcareous siltstone (Fig. 3A) to a non-calcareous siltstone.

3.2 Structure

3.2.1 Thrust Contacts

Two main thrusts are observed at Jebel Tays, an eastern thrust in which serpentinised rocks have been thrust over the Abt Formation and a westerly thrust in which the Abt Formation has been thrust over serpentinised rocks. The easterly thrust is sub vertical along most of its exposure, the surface expression of this easterly thrust is limited to ca 300 metres and it is only in a single section that it appears as a sub-horizontal basal thrust (Fig. 5A). Kinematics along this contact preserve evidence for both top to the east and dextral movement (Fig. 5 C&D). The western thrust is steep and dips towards the west, unlike the eastern thrust it is characterised by extensive quartz veining and small scale asymmetric folds within the Abt Formation that reveal top to the east movement (Fig. 5 F&G).

No mechanical contact is found internally within the ultramafic/mafic complex, however, a discrete (ca 100m) linear zone of serpentinite and carbonate containing large (ca 3mm) euhedral pseudomorphs of pyrite can be traced from north-east to south-west across the exposure (Fig. 3D). This pyrite growth is not related to serpentinisation or carbonatisation as it is not found in other serpentinite or carbonate exposures. These features are commensurate with a structural shear or fault origin for this mineral assemblage, the fact that it does not have the appearance of a mechanical boundary is most likely related to the rheology of the host serpentinite and carbonate.

The other geological relationship in the area is the cross cutting of this ultramafic/mafic complex by trondhjemitic rocks. Both plutonic type intrusives as well as dykes are observed. While the Abt Formation is also cross cut by dykes these are not trondhjemtic. From field observations the trondhjemite intrusions are limited to the ultramafic/mafic complex, implying a pre-basin closure for this intrusion, this is supported by geochronology (see section 7). Thus these intrusives have been carried to their present crustal position along the same mapped thrust structures rather than their intrusion post thrusting.

Based on these three mapped structures, Figure 4 is a schematic cross section showing the key mechanical boundaries that are observed. It can be seen from the solid geology map of the area (Fig. 6) that extrapolating these boundaries further north and south is problematic due to extensive scree slopes and Quaternary cover, however, it is logical that the major thrusts extend north and south separating the Abt Formation from the ultramafic/mafic rocks.

3.2.2 Structural History

Conglomerate beds of the Abt Formation contain orientated cobble clasts that have lent themselves to R_f/ϕ analysis (Chew, 2003; Dunnet, 1969) allowing the quantification of strain and for a robust determination of the finite strain ellipse. Key measurements and calculations required for such analysis are:

R_f	Measured ratio of long axis to short axis of conglomerate clasts.
ϕ	Measured angular difference between long axis angle and angle of maximum extension.
R_i	Calculated initial ratio of long axis to short axis.
θ	Calculated initial angular difference between long axis angle and angle of maximum extension.
R_s	Calculated ratio of long axis to short axis of the strain ellipse.

This method relies on R_f, the shape of the final ellipse, which is determined by the combination of the initial ellipse shape (R_i), its initial orientation (θ), the

shape of the finite strain ellipse (R_s) and its orientation (ϕ') and importantly an assumption that the cobble clasts originally had no preferred orientation but have subsequently developed a non-random orientation. A test of this assumption can be made based on a calculated index of symmetry, the basis of this test involves a numerical symmetry calculation based on the equation:

$$I_{sym} = 1 - [\, | n_a - n_b | + | n_c - n_d |]/N \text{ (Lisle, 1985)}$$

where n = number of clasts in each quadrant

N = total number of clasts

This test relies on the knowledge that if an initial preferred orientation existed it would produce asymmetry in the resulting deformed clasts about $\phi = 0$. From the data acquired an I_{syn} value of 0.79 (100% symmetrical produces $I_{sym} = 1$) was obtained indicating an initial random orientation. Based on this test of symmetry a plot of R_f vs. ln ϕ was produced (Fig. 7A) which shows a tight symmetrical grouping of data around a constant value of ϕ and characterised by a harmonic mean (mean of calculated R_f) of 2.905 along a vector mean (mean ϕ) of 4.912 which equates to a mean elongation direction of 189° (south). The strain ellipse was calculated by the iterative process of modifying R_s to produce the most random distribution of initial clast orientation (i.e. random χ^2 distribution). With reference to Figure 7B it can be seen that χ^2 was minimised at $R_s = 3$ which is very close to the calculated mean R_f indicating that the mean orientation of the clasts is a very good approximation of the finite strain ellipse.

From this statistical treatment of cobble clast orientation and axial ratios the finite strain ellipse is characterised by a north-south orientated S_1 with a axial ratio of 3. Quantification of strain is possible based on the relationship of $R_i = [R_{f(max)}/R_{f(min)}]^{0.5}$ which produces a $R_{i(max)} = 2.7$, this equates to a minimum 10% extension of the cobble clasts. Equating the finite strain ellipse to an orientated paleo stress field results in an east-west orientated σ_1.

Foliation data presents a more complicated history of deformation, Figure 8 presents poles to foliation planes obtained from across the ultramafic/mafic complex and adjacent Abt Formation. A first order interpretation of these data reveal that foliations are broadly north-south orientated and dip steeply towards the west. Furthermore, a girdle fitted to these data would indicate that the foliation fabric has been folded around an axis orientated along 107↔287 suggestive of north-south shortening. While foliations do indeed show an overall north-south strike, the foliation data is more complex and 3 deformation fabrics are present, the apparent north-south shortening axis is an artefact of the stereonet presentation.

A detailed form surface map is shown in Figure 9 revealing the 3 distinct deformation fabrics. The S1 fabric is broadly north-south orientated and dips steeply to the west, this broad pattern is complicated in the north-east of the area where S1 has been folded (D2) around an axis orientated along 045↔225. In the south gabbros that contain this S1 fabric also contain small metre scale conjugate fault sets that suggests that this S1 fabric is associated with an east-west orientated σ_1, a vertical σ_2 and a north-south orientated σ_3. S2 is interpreted as a shear fabric that is parallel to the axis of the D1 fold (NE-SW). This fabric is developed dominantly within serpentinite lithologies. Kinematics along the eastern thrust which is located within the mapped shear zone contains dextral SC fabrics and also contains top to the east kinematics. Also associated with S2 is the previously discussed mineral assemblage of serpentinite and/or carbonate with euhedral pyrite which is interpreted to be associated with fluid flow. As with D1, D2 is also commensurate with an east-west orientated σ_1. S3 is the fabric associated with the western thrust, is broadly north-south striking but in the north is orientated parallel to S2. Numerous asymmetric and thrusted folds reveal top to the east movement evidencing an east-west orientated σ_1 and vertical σ_3.

Whilst three fabrics are observed (S1, S2, S3), the associated deformation stress fields (D1, D2, D3) are all commensurate with an east-west orientated

σ_1. As previously discussed deformed cobble clasts also point to an east-west orientated σ_1. Thus all fabrics are compatible within the same orientated maximum principal stress but some of the observed kinematics require different orientations of σ_2 and σ_3. Such a requirement for multiple or alternating σ_2 and σ_3 are possibly accommodated by a combination of differing rheologies (S2 seems to be limited to serpentinite lithologies) and/or σ_2 and σ_3 being of similar magnitudes.

Previously the Jebel Tays structure has been interpreted as a series of thrusts developed within mélange along with a major synform that bisects the central mafic/ultramafic complex along a north-south axis, much akin to alpine style nappe structures (Al-Shanti and Gass, 1983; Johnson et al., 2004). From my mapping no evidence of this synform was observed, the Jebel Tays structure is bounded by two mechanical thrust contacts with the Abt and three prominent fabrics are present. All three fabrics are associated with a east-west orientated σ_1 and it is considered highly likely that D1 and D2 are broadly coeval in nature, D1 being related to east-west thrusting and D2 with dextral strike-slip shearing, this shearing is evidenced by the S2 fabric and the growth of euhedral pyrite aligned along one of these shear zones. This D2 shearing has reorientated S1 and may have also reorientated the principal thrust structures. The current observed stratigraphic relationships of lower crustal gabbros and ultramafics resting structurally on top of low greenschist facies sediments suggests that timing wise, the eastern thrust is the earliest fault structure, thus implying the western thrust is a latter structure. The alternative to this timing would imply thrusting of sediments onto the lower crustal gabbros and ultramafics before their thrusting from their lower crustal levels of emplacement. I consider this highly improbable. While this relative timing seems robust, absolute timing of the activation of the eastern and western thrusts is poorly constrained and could be separated by a significant period of time.

The observed stratigraphy of Jebel Tays, dominated by gabbro blocks and serpentinite mud volcanism, is best interpreted as an ophiolitic thrust sheet in which gabbroic blocks have been transported within a serpentinite mud matrix.

4 MAFIC, INTERMEDIATE AND ULTRAMAFIC SUITE

Mafic, intermediate and ultramafic rocks are volumetrically the most abundant rocks that crop out within the area and have undergone varying degrees of alteration, from modest greenschist facies fluid alteration and minor serpentinisation (gabbro), to wholesale serpentinisation and carbonatisation (ultramafics). In many cases these rocks contain a prominent tectonic fabric associated with basin closure and/or obduction.

4.1.1 Petrology

Gabbros range from isotropic to gneissic, the two samples examined in thin section are dominated by euhedral to sub euhedral green amphibole (hornblende) (50% / 2-3 mm) and plagioclase (30% / 2 mm), which is highly altered and with no evident twinning or zoning due to extensive masking of these common characteristics by a dusty alteration. Fractured sub-euhedral olivine (20%) is also present. The euhedral amphibole appears to be primary indicating a high H_2O% melt. Gabbros have a sub-ophitic texture. This mineral assemblage suggests this gabbro is best defined as a hornblende gabbro. Of the ultramafic cumulates, one is composed entirely of unaltered euhedral to sub-euhedral green amphibole (hornblende) which I interpret to be primary. The second cumulate sample is dominated by serpentine (~45%), CPX (~40% / 3-4 mm) exsolving OPX, magnetite (~10%) and chrome spinel (~5% / 2-3 mm). The serpentine displays a mesh texture and assuming most of this serpentine was olivine and/or OPX implies these cumulates are wehrlites or harzburgites. Photomicrographs are shown in Figure 10.

4.1.2 Ultramafic Major Element Geochemistry

Ultramafic rocks exposed within the Jebel Tays complex are widespread dominated by serpentinised peridotite, that are interpreted as originally to have formed in the mantle. One sample examined (S09-090 Lat: 23° 5' 52.87" N, Lon: 44° 58' 25.03" E) is most likely part of a cumulate sequence. Due to the extensive alteration, major element chemistry has focused primarily but

not exclusively on microprobe analysis of chrome spinels due to their resistance to alteration.

4.1.3 Mafic Suite Major Element Geochemistry

On a total alkali vs. silica diagram (Fig. 22C) (Le Maitre, 1989) the mafic to intermediate intrusive rocks plot as high silica gabbros and diorites while the extrusives, which are predominately found as cross-cutting dykes, have basaltic to andesitic compositions. Due to the low greenschist facies metamorphism and evidence for extensive fluid flow it is to be expected that major element compositions (particularly the alkalis) have suffered from alteration. Harker diagrams (Fig. 11A) show some variation that does not seem to be correlated with SiO_2 content. Al_2O_3 and Fe_2O_3T compositions show the most variation possibly suggesting a degree of major element post-emplacement alteration. I interpret this alteration to be a consequence of basin closure and/or obduction. Normative compositions for the intrusives (gabbros) characterise these as noritic gabbros (Fig. 12) (Streckeisen, 1974), however such calculations assume anhydrous conditions and in thin section these gabbros are dominated by amphibole. Thus these gabbros are best described as hornblende gabbros. While such compositions are possibly the result of cumulate processes, the lack of a Eu anomaly (discussed later) would seem to suggest that this composition is not related to crystal settling processes.

4.1.4 Mafic Suite Trace Element Geochemistry

Modified Harker diagrams utilising the relatively immobile Zr potentially allow for the argument that all mafic rocks represent a related igneous suite. It can be seen that the range in immobile Zr is small within the intrusive suite (gabbros) and that increasing Zr content is coupled to silica content suggestive of fractional crystallisation (Fig. 11B). This trend of small variations in trace element contents not unexpectedly persists from Zr through to Lu (Fig. 13). With reference to the full trace element plot (Fig. 13A) these rocks exhibit a fan like trend, pinned at the HREE end and then fanning towards the large ion lithophile elements. The pattern is consistent with fractional

crystallisation from a common parental magma, as opposed to parallel patterns for magmas related by differing percentage melting. The trace element abundances for both intrusives and extrusives show a large degree of variability in the LILE, which is consistent with greenschist facies metamorphism and fractional crystallisation. Broadly, intrusives show LILE/LREE depletion while extrusives show LILE/LREE enrichment, both show similar HREE patterns.

The trace element pattern for the intrusives (gabbros) in particular reveals marked depletion from Nb to Lu characterised by a distinctive positive gradient, these elements, particularly the HREE, are characterised by low partition co-efficients and thus considered immobile and stable under greenschist facies metamorphism. This suggests partial melting of a depleted ultramafic source in the absence of any evidence for garnet and or amphibole as residual phases, as such phases readily incorporate HREE such as Yb or Lu which would also produce HREE depletion (but not a positive gradient). This is further supported by moderately high Mg# of ca 0.60 (Mg#'s range between 0.53 to 0.74 across a silica range of 48%-52%, Mg# is broadly covariant with silica) and suggestive of a melt sourced from a mantle unlike that of modern MORB (Mg# 0.4 to 0.5) (Max Planck Institute, 2009) but in the range of modern island arcs. Another possibility for these elevated Mg#'s is that these gabbros are actually cumulates, however, due to the tendency of Eu to partition preferentially into plagioclase, mafic cumulates tend to exhibit Eu anomalies (positive or negative depending on where plagioclase resides) in their REE patterns, it can be seen with reference to Figure 13B that the analysed gabbros do not exhibit any prominent Eu anomaly.

4.1.5 Tectonic Discrimination & Petrogenesis

Tectonic discrimination of mafic rocks is largely based on major and trace element signatures of basalts, this is because undifferentiated volcanic rocks are more likely to approximate primary melt compositions. However, due to the scarcity of fine-grained volcanics at Jebel Tays, along with the extrusives

having very similar HREE patterns and concentrations to the intrusives and the observation that the intrusives show no cumulate textures, I include them in the following trace element discrimination diagrams.

Pearce (2008) and Pearce *et al.* (1984b) separate rocks of ophiolite affinity into two major classes, supra-subduction zone (SSZ) and intra-oceanic (MORB). MORB ophiolites are further sub-divided into C-MORB (contaminated i.e. sedimented ridge crests), N-MORB, E-MORB (enriched) and P-MORB (i.e. plume influenced ridge) while SSZ ophiolites are sub-divided into those with boninitic/island arc affinity or MORB/island arc affinity. These classes he argues can be distinguished by key trace and minor element abundances of Cr/Y, Th/Yb, Nb/Yb, Ti/Yb.

Cr/Y is a useful discriminant of rocks with Island Arc Tholeiitic (IAT) affinity and MORB (Pearce, 2008). Figure 14 shows the compositions of seven gabbroic and basaltic rock samples obtained from the Jebel Tays complex along with the superimposed fields of MORB, IAT and magmas of boninitic affinity.

Cr/Y values of all of the sampled mafic rocks plot within the field of IAT/boninite and they follow a trend consistent with magmas sourced from a previously depleted asthenosphere.

Heavy rare earth elements, particularly Yb, are often used as a proxy for melting depth and once again can be used to some extent to discriminate between MORB, IAT or OIB tectonic settings. The basis for this proxy is the high affinity of amphiboles and garnet for Y and Yb, which results in them being strongly partitioned into these phases. As amphibole and garnet, in particular, are strongly controlled by pressure and hence depth they thus become a melting depth proxy. It can be seen with reference to Figure 15 that on the basis of this proxy most samples plot within the MORB array suggesting melting at shallow depths.

Nb/Yb and Th/Yb ratios are also presented and are used to determine crustal input and/or source composition. Nb is generally held by the slab due to its strong affinity for Ti bearing phases such as rutile and thus concentrations are high in MORB. Thorium on the other hand is an indicator of crustal input due to it being enriched in the continental crust reservoir. The plot of Th/Yb vs. Nb/Yb (Fig. 15) provides an indication of source composition and/or crustal contamination. It can be seen that the mafic rocks from Jebel Tays produce a low angle vector away from the MORB array following a trajectory of increasing fractionation, this suggests a continental input. It has been argued that such low angle vectors are driven by fractional crystallisation processes associated with only minor sediment input (i.e. indicative of IAT), as opposed to major sediment input (i.e. continental arcs), which have a tendency to produce more oblique vectors (Pearce, 2008). Furthermore, this vector intercepts the MORB array well below N-MORB, due to the lack of evidence for extensive cumulate processes (i.e. no Eu anomaly) this again suggests a source more depleted than that for N-MORB.

These trace element plots discussed above present the apparent dichotomy of shallow MORB like depths of melting within a supra-subduction zone/arc setting. I suggest that this combination of features is unique to forearc melts and that these melts are best described as low Ti island arc tholeiites with boninitic affinity.

Some confusion exists surrounding the use of the term boninite in literature as its use alternates between its *senso stricto* form and a more general series or affinity form. Boninites *senso stricto* are volcanic to hyperbyssal rocks with high SiO_2 (>53% - therefore strictly andesites), high H_2O, and MgO concentrations (Mg# >0.6), low TiO_2 with respect to typical IAT basalts (Scotia arc mean = 1.2%) and include clinonenstatite (Falloon and Danyushevsky, 2000). They are named for their extensive occurrence on the Bonin Islands within the forearc of the Izu-Bonin-Mariana Arc (Macpherson and Hall, 2001). In contrast, rocks of boninitic affinity are mafic to intermediate rocks that show

similar features such as high SiO_2, high Al_2O_3/TiO_2 ratios (i.e. moderate to high Al_2O_3 and low TiO_2), depleted HFSE concentrations and importantly a LREE depletion in their normalised REE pattern. In this paper I use the term boninite in the affinity sense unless stated otherwise. Regardless of the use of the term, both boninites *senso stricto* and those of boninitic affinity require the unique conditions of high temperatures (>1100°C), water and melting of an already depleted mantle (i.e. refractory mantle) at shallow depths (Falloon and Danyushevsky, 2000), such conditions are widely considered unique to forearcs (Bedard et al., 1998; Falloon and Danyushevsky, 2000; Kim and Jacobi, 2002; Macpherson and Hall, 2001; Taylor et al., 1994). It can be seen with reference to Table 2 that the mafic rocks of Jebel Tays lie within the compositional field of *senso stricto* boninites and low Ti IAT.

Table 2. Comparison of *senso stricto* boninites with gabbros and basalts of the Jebel Tays complex, boninite data compiled from http://georoc.mpch-mainz.gwdg.de (Max Planck Institute, 2009)

	Boninites *(senso stricto)*			Jebel Tays Mafics		
	Mean (n=142)	Min	Max	Mean (n=8)	Min	Max
SiO_2 %	55.8	47.2	66.5	52.3	48.1	61.9
TiO_2 %	0.25	0.03	1.3	0.67	0.39	0.92
Mg#	0.71	0.42	0.89	0.58	0.39	0.70
Nb/Yb	1.3	0.21	18.8	1.3	0.18	3.25
TiO_2/Yb	0.26	0.09	1.08	0.59	0.31	1.15
Th/Yb	0.36	0.02	2.4	0.48	.006	1.74

Low Ti IAT, or rocks of boninitic affinity, as discussed previously, represent forearc magmatism sourced from a refractory mantle sequence, to further test this forearc connection for the mafics that crop out at Jebel Tays, the analysis of chrome spinels was undertaken to address both source composition as well as tectonic setting of genesis. The use of chrome spinels as a petrogenetic indicator is well established (Dare et al., 2009; Henderson and Suddaby, 1971; Malpas and Strong, 1974). They are proxies for both tectonic setting and melt source, and are commonly used as they are thought to be resistant to alteration, but see Power *et al.* (2000) for a caveat. Electron microprobe analysis was undertaken on 12 chrome spinels from a cumulate ultramafic,

the chrome spinels are characterised by a decrease in Cr_2O_3 and Al_2O_3 content towards the rims (Cr_2O_3: 39% at cores, 24% at rims / Al_2O_3 22% at cores, 2% at rims) and a commensurate increase in Fe_2O_3 at the rims (Fig. 16). These elemental maps clearly show this alteration with an exchange of Al^{3+} for Fe^{3+} at the grain boundaries. The nature of this alteration has been documented by O'Hanley (1996) and ascribed to sub-solidus reaction with serpentinite which results in the loss of Al and enrichment in Fe. All analysis used for petrographic discrimination is based on the composition of these unaltered cores. These elemental maps reinforce the work of Power *et al.* (2000) that chrome spinels can indeed undergo significant alteration.

Several tectonic discrimination diagrams exist for chrome spinels, the most commonly used being Cr# vs. Mg#. The basis for using Cr# and Mg# for tectonic discrimination relates to spinel chemistry being affected by the degree of partial melting of peridotite, specifically the melting of diopside. Variations in Cr# (Cr# = $[Cr^{3+} / (Cr^{3+} + Al^{3+})]$) is largely a function of Al content, which in mantle rocks is controlled by the melting of diopside - the major Al bearing phase in the mantle (Al occupies the Si site in a 4^+ valence state). As diopside is preferentially melted at higher temperatures than other mantle phases, residual spinels are depleted in Al (Al is the more incompatible phase) shifting the Cr# in spinels to higher values. Based on the melting of diopside to exhaustion, mid-ocean ridge depleted mantle have upper compositional limits of residual spinels of ca 0.50 (Dick and Bullen, 1984) and is largely governed by the reaction:

$$\text{Olivine} + \text{OPX} + \text{CPX} + \text{Sp} + \text{Melt} \Rightarrow \text{Olivine} + \text{OPX} + \text{Sp} + \text{Melt}$$

The CPX out reaction is considered a significant thermal boundary that limits high Cr# at mid ocean ridges and to a significant extent back-arc spreading ridges. Cumulate rocks are of course not residual sequences, in these cases Cr# above ca 0.50 require a mantle source already depleted in diopside to near or past this CPX out boundary (Barnes and Roeder, 2001).

Unaltered spinel cores from serpentinised cumulates plot (Fig. 17) within the field of forearc peridotites of Azer & Stern (2007) and in the transitional Type II (depleted to ultra depleted peridotite) of Dick & Bullen (1984). These spinels are at the absolute extreme end of Cr#'s that can theoretically be achieved by partial melting at mid ocean ridges (Dick and Bullen, 1984).

The content of Al in chrome spinels as an indicator for the degree of peridotite depletion has been applied to the Egyptian shield serpentinised peridotites (Azer and Stern, 2007). They argue that even with the extensive alteration of serpentinites, Al, Mg and Ca major element mobilisation is no greater than the hand specimen scale, thus they argue that it is possible to see through extensive serpentinite alteration to make inferences of peridotite composition. A first order test of element mobility is very low Na_2O and K_2O compositions, for the peridotite samples from Jebel Tays, Na_2O concentration is less than 0.13% and K_2O is below detection limits, the samples also show restricted range in CaO, MgO and Al_2O_3 which supports the work of Azer & Stern that apart from water and to a limited extent silica, very little has been added or subtracted from these rocks. This is further supported by the coherent trace element patterns of these serpentinites. The 2 serpentinite samples analysed (Fig. 18) plot as forearc peridotites with both low Al and Ca contents. This is a result of the same processes affecting chrome spinel chemistry discussed earlier, that is melting of peridotite to the exhaustion of diopside.

The idea that these mafic melts are derived from a refractory mantle source is further supported by Sm and Nd isotopes. Three isotropic gabbro samples provided present day ε_{Nd} values of 12.41, 14.63 and 0.09, this compares with a depleted mantle value today of 9.98. Age adjusted ε_{Nd} values for 677 Ma results in two of these samples ε_{Nd} values converging to 7.33 and 7.38 and the third to 4.01, these plot below (Fig. 19) the trend for the depleted mantle (DePaolo, 1980; Goldstein et al., 1984; Jacobsen and Wasserburg, 1979). These data result in depleted mantle model ages for these gabbros (460 Ma & 560 Ma) being significantly younger than their stratigraphic age of 677 ± 4.9

Ma (see section 7). Such ε_{Nd} values are difficult to explain but the fact that two independent samples converge to the same $\varepsilon_{Nd(T)}$ value in itself suggests that they are not a result of analytical error. The results indicate that in two of the samples these melts have higher Sm/Nd ratios than the depleted mantle reservoir, this is difficult to envisage considering that Sm is less incompatible than Nd. The relative incompatibilities of Sm and Nd requires that upon partial melting, Nd is preferentially partitioned into the melt phase, this results in melts having Sm/Nd ratios that are less than their source. This is why $^{143}Nd/^{144}Nd$ ratios, driven by the decay of ^{147}Sm to ^{143}Nd, normally evolve with gradients less steep than the depleted mantle. Other likely scenarios such as sediment assimilation may explain why these plot below the depleted mantle at their stratigraphic age, but does not explain the steep trajectory above the depleted mantle. One interpretation that the data supports is that the mantle underlying at least parts of the Arabian shield during the Neoproterozoic can not be described by the depleted mantle models of De Paolo (1980) and Jacobsen & Wasserburg (1979) and must have been more depleted than their models predict. This lends further support to our contention that these melts are of boninitic affinity as such a refractory mantle is a key requirement for their genesis (Falloon and Danyushevsky, 2000). This is not the only ANS ophiolite to have such strongly positive $\varepsilon_{Nd(T)}$ values, Stern *et al.* (2004), in their review of ANS Neoproterozoic ophiolites, also comes to the conclusion that due to the consistently strongly positive $\varepsilon_{Nd(T)}$ of ANS ophiolites, the ANS during the Neoproterozoic must have been underlaid by depleted mantle of harzburgitic composition. This interpretation was based on six other ANS ophiolites and the range of these $\varepsilon_{Nd(T)}$ values encompass the values obtained for the gabbros of Jebel Tays (Fig. 19). The third sample, which does not exhibit the steep $^{143}Nd/^{144}Nd$ trajectory observed in the other two samples is thought to be more substantially contaminated by subducted sediments.

Geochemically these mafic and ultramafic rocks have definitive forearc characteristics and the mafics are best described as low titanium island arc tholeiites with boninitic affinity. This type of mafic magmatism is well

documented (Bedard et al., 1998; Ishikawa et al., 2002; Kerrich et al., 1998; Kim and Jacobi, 2002; Melcher and Meisel, 2004) and in fact these magmas are very similar to the intermediate Ti-boninites of the Betts Cove ophiolite, Newfoundland (Fig. 20) (Bedard et al., 1998) and very much like the boninite series low Ti tholeiites of the Abitibi greenstone belt, Ontaria (Kerrich et al., 1998). What is evident from this plot is the positive gradient from Nd to Lu indicating REE fractionation. It is this positive gradient that provides the evidence for the two stage genesis of boninitic magmas, firstly, extraction of MORB like melts with increasing depletion of the MORB source from Lu to La. A second melt extraction from this depleted source then inherits this positive gradient and exhibits fractionated REE with respect to MORB (Kerrich et al., 1998). Boninites have also been known to show LILE/LREE enrichment due to the composition of the fluxing fluids resulting in U-shaped spider plot patterns, this REE pattern is not always present as it is specifically a function of fluxing fluid composition, though it can broadly be observed in Figure 20.

While no quantitative thermobarometry has been obtained for these rocks, probe analysis of plagioclase in these gabbros reveals that these plagioclases are bytownites ($An_{80\text{-}90\%}$) giving qualitative evidence for either a hot forearc setting, high H_2O content (this is evidenced by primary amphibole) or derived from a refractory source with a high Ca/Na ratio, all of which are necessary pre-requisites for boninitic forearc melts.

5 TRONDHJEMITE, TONALITE AND GRANODIORITE SUITE

Plagioclase rich rocks that fall within the TTG field (Fig. 22D) of Barker (1979) crop out within the Jebel Tays area and are found both as plutonic bodies and dykes that cross-cut both gabbroic and serpentinite sequences, neither dyke or plutonic exposures have a tectonic fabric.

5.1.1 Petrology

The coarse-grained trondhjemites contain highly altered plagioclase (~40% / 3-5 mm), alkali feldspar (~10% / 2-4 mm), interstitial quartz (30% / 1-2 mm), highly altered sub-euhedral to euhedral epidote (~15% / 1-2 mm) and euhedral titanite (~5% / 0.5-1 mm). Plagioclase is extensively saussuritized to muscovite and possibly epidote or zoisite and has a dusty appearance in plane-polarised light, even so relic oscillatory zoning and multiple twinning can still be observed (Fig. 21). Fine-grained varieties are essentially the same while both coarse and fine-grained varieties contain secondary chlorite. This primary mineral assemblage is that of an I-type granite and while these rocks do not contain a tectonic fabric, the mineral assemblage of epidote, muscovite and chlorite along with fluid flow redox boundaries (Fig. 3C) is clear evidence for post crystallisation metasomatism. It is not clear whether the euhedral epidote is primary or after amphibole, either way the presence of either of these minerals as primary suggests a high H_2O content of the primary melt.

5.1.2 Major Element Geochemistry

These TTG suite rocks are characterised by silica contents ranging between 65-70% and Mg# of ca 0.48. On the total alkali's vs. silica plot (Le Maitre, 1989), these rocks plot in the field of quartz diorite/dacites and while showing calc-alkaline affinity do not follow the calc-alkaline trend of increasing potassium enrichment towards syenite compositions (Fig. 22A). Individually these rocks show metaluminous to ever so slightly peraluminous character but overall are I-type in composition (Fig. 23B) indicating fractionation from a

mafic source with only small amounts of crustal input. Normative plots reveal that these rocks plot within the fields of trondhjemites and tonalites and generally close to the apex defined by trondhjemites - tonalites - adamellite (Fig. 22D). Early work on the classifications of TTG rocks done by Coleman (1975) to discriminate such rocks between oceanic plagiogranites and continental TTG's on the basis Al_2O_3 content is ambiguous in this case as they all plot along the line separating continental TTG's and oceanic plagiogranites.

5.1.3 Trace Element Geochemistry

The N-MORB normalised trace element spider plot (Fig. 23) exhibits LILE enrichment with a steep negative gradient from Cs to Ta indicative of continental crust input. However, the overall I-Type signature of these rocks suggests such sediment and/or continental crust input was not overwhelming. Furthermore, an Nb anomaly (depletion) indicative of subduction related melts is present. The basis of this widely used subduction signature is to this day not fully understood, one theory suggests it is related to contamination of these melts by continental derived material which have very low Nb concentrations. This argument, while persuasive, is a somewhat circular argument considering that it is generally believed that the continental crust is generated by arc magmas. Others hold that the anomaly is related to Nb being held back by ocean crust Ti bearing phases such as rutile (Plank, 2007), this however requires the pre-requisite of slab melting, extensive melt slab interaction or metasomatism by slab derived fluids. Regardless of the reason for Nb anomalies, Nb is a conservative element in subduction systems (Pearce and Peate, 1995) and Nb depletions are a persistent characteristic of SSZ melts.

Trace element concentrations from Nb to Eu are widely considered as proxies for either source composition or percentage melting (Pearce and Peate, 1995). This section of the trace element diagram reveals a flat gradient and represents a composition somewhere between that of N-MORB and E-MORB,

the exception to this is the striking positive Sr anomaly which is most likely a function of strontium's high affinity for plagioclase in these plagioclase rich rocks (Blundy and Wood, 1991). This flat MORB-like Nb to Eu signature can be interpreted as the result of either:

1. Small percentage melting of a depleted ultramafic source, such a source would need to be significantly more depleted than the source of MORB to explain it being enriched relative to MORB or
2. Significant melting of mafic rocks of a MORB composition

The heavy end of the REE plot (HREE/HFSE) shows marked depletion with respect to MORB and the magnitude of this depletion suggests melting at amphibolite or eclogite depths with garnet or amphibole as residual phases. Garnet and/or amphibole strongly partition heavy rare earth elements, such as Yb, resulting in a marked HFSE depletion of melts generated at these depths (Barth et al., 2002; Klein, 1994; Klemme et al., 2002). An alternative to this interpretation would be the partial melting of an even more depleted mafic source.

5.1.4 Tectonic Discrimination & Petrogenesis

The genesis of ophiolite associated TTG granitoids has generally been attributed to highly fractionated mid ocean ridge melts (i.e. plagiogranites) (Coleman, 1975; Spulber and Rutherford, 1983), however, trace element data does not support this interpretation. Two widely used discrimination diagrams involve Rb vs (Y+Nb) and Ta vs Yb, due to the conservative nature of Y, Nb and Ta in particular, these projections are considered to be largely alteration independent (Pearce et al., 1984a). The key benefit of the use of these diagrams is that while any single bivariant plot on it's own contains significant overlaps between fields, especially between volcanic arc granites and syn-collisional arc granites, such overlaps can be distinguished through the use of both. In the case of these plagioclase rich rocks the boundary between volcanic arc granites and ocean ridge granites contains very little overlap due to Y and Yb acting as a melting depth discriminant, with true oceanic

plagiogranites, by virtue of their tectonic setting being produced at shallow MORB like depths, Y and or Yb distinguishes such plagiogranites from volcanic arc TTG's.

While we have discussed in some detail the petrographic basis for these diagrams it is clear that these granitoids plot well away from the field of oceanic plagiogranites (ORG) (Fig. 24), this supports the HREE trace element abundances that suggest melting at depths not experienced at mid ocean ridges as well as geochronology which shows that these felsic rocks are 44 Ma younger than related gabbros, all incompatible with oceanic plagiogranite genesis.

Excluding extremely fractionated mafic melts as a likely petrogenetic model, other major models for TTG genesis involve the:

1. Anatexis of mafic crust at shallow to intermediate depths due to shearing (Koepke et al., 2007; Koepke et al., 2004; Zhang et al., 2009) or
2. The melting of the subducting slab at amphibolite or eclogite conditions, so called adakite melts (Martin, 1999).

Under many situations it would be possible to discriminate between anatexis of shallow mafic source rocks and slab melting on the basis of melting depth, but considering that the mafic rocks at Jebel Tays already show depletion across the HREE spectrum, this is likely to mask this important melting depth proxy. However, the positive gradient of the REE plot for the gabbros at Jebel Tays (Fig. 13) compared with the negative REE gradient of these trondhjemitic intrusives makes the exposed forearc gabbros of Jebel Tays an unlikely source rock candidate for anatexis. This leaves only slab melting as a logical model for the genesis of these trondhjemitic intrusives.

Martin (1999) identifies the key characteristics of adakites to be trondhjemitic affinity, low K_2O, high Na_2O and, importantly, fractionated and depleted REE requiring garnet and/or amphibole as residual phases, this depletion is the

result of garnet and amphiboles high affinity (k_D >>1) for HREE such as Y, Yb and Lu. Table 3 presents a comparison of what is considered “classic” adakitic geochemistry with those of the Jebel Tays trondhjemite intrusion. The petrogenetic basis for these so called “key characteristics” are:

- Sr enrichment is a result of the abundance of plagioclase with Sr partitioning into the Ca site in plagioclase.
- Comparatively high Mg#’s are deemed to be the result of interaction with the mantle wedge during ascent.
- Low Yb and Y are a result of melting with garnet and/or amphibole as residual phases.

Table 3. Key geochemical characteristics of adakites

	“Classic” Adakites (Martin, 1999)	Jebel Tays Trondhjemite
Sr (ppm)	>300 – 2000	592
Mg#.	~0.5	0.47
Yb (ppm)	≤1.8	0.39
Y (ppm)	≤18	4.7
K_2O/Na_2O	~0.5	2.63

It can be seen with reference to table 3 that the TTG granites of Jebel Tays are a good match for adakitic melts except the ratio of K_2O to Na_2O, its difference here, however, is likely to be a result of both K and Na being highly mobile in hydrothermal conditions, such alteration is evident in these rocks (Fig. 3C). The key geochemical discriminants for adakites are Sr/Y vs Y (Martin, 1999) and La/Yb vs Yb (Defant and Drummond, 1990), these separate adakites from other volcanic arc magmas. The basis of these trace element discriminant diagrams are high Sr/Y ratios which reflect low Y concentration suggestive of melting at depth and a lack of plagioclase fractionation which separates them from volcanic arc dacites. La/Yb ratios are again melting depth proxies. It can be seen with reference to Figure 25 that for both bivariant plots the TTG rocks from Jebel Tays plot within the compositional field of adakites. More specifically these rocks have the composition of high silica adakites (HSA) (Martin et al., 2005) which are

considered to be the result of slab melting and ascent of the melt through the mantle. This is different to low silica adakites (LSA) which have a more complicated but related petrogenesis involving slab melting, followed by this melt metasomatising the mantle wedge.

Adakitic melts are volumetrically rare in the post Archaean geological record and are considered to be the result of flat subduction of young oceanic crust or ridge subduction (Martin et al., 2005), how young is often debated and early work placed a 25 Myr age constraint on the subducting slab (Defant and Drummond, 1990). Further constraining the P-T conditions for adakite melting comes from adakitic migmatite inclusions within garnet bearing amphibolites that have recorded pressure-temperature conditions of 650-750°C at pressures between 9-11kbar (Sorensen, 1987; Sorensen, 1988), which equates to depths of 30 to 40km. However, recent work into the thermal structure of subducting slabs suggest that the young hot slab requirement may not be required. Better resolved modelled thermal structure of modern slabs based on non-Newtonian mantle rheology produce slab interface temperatures of ~800°C beneath the volcanic arc front and higher for younger slabs (van Keken and Kiefer, 2002), these results were based on the Honshu (fast cold slab) and Cascadia arcs (slow hot slab) respectively. This work is further supported by research into slab fluid temperatures, fluid melt inclusions predict slab fluid temperatures of up to 950°C (Plank et al., 2009) and is in contrast to early slab models which predicted slab interface temperatures of ≤ 600°C. Thus recent research lends support to slab melting in modern arcs being potentially far more widespread and not restricted to young oceanic lithosphere.

The process of how such melts migrate through the wedge into the lower crust is not well understood but due to the high Mg#'s (~0.50) of these felsic melts ascent through the mantle is considered the probable mechanism for such melts gaining high Mg# through the reaction of the melt with the surrounding peridotite (Rapp et al., 1999). This process is shown qualitatively in Figure 26.

It is argued that on the basis of Mg# alone this precludes other mechanisms for producing adakitic melts such as the melting of underplated mafics or the melting of mafics during shearing (Martin et al., 2005) as such models do not allow for significant interaction with a high Mg reservoir such as the mantle. The trondhjemite exposed at Jebel Tays has elevated Mg#'s (0.46) which suggests that it is not derived from the partial melting of mafic rocks from this region, either the gabbros exposed at Jebel Tays or those exposed at Halaban village. This conclusion is unequivocal considering the isotopic compositions of these rocks. The ε_{NdT} values of the two trondhjemite samples have values of 4.93 and 5.05 and do not intercept the ε_{Nd} trajectories at its crystallisation date of 632 ± 8.0 Ma of either of the regionally exposed mafics which precludes them as possible source rocks.

6 CARBONATES

6.1 Stable Isotope Geochemistry

Carbonates are widespread at Jebel Tays and are generally found as massive orange cap rocks forming on top of serpentinised ultramafics. Field relationships clearly indicate that these carbonates are an alteration product from a serpentinised ultramafic protolith. In several locations serpentinised ultramafics can be seen grading into carbonate, furthermore, in thin section carbonates show evidence of relic serpentinite mesh texture (Fig. 27). XRD analysis reveals that magnesite and calcite are the dominant phases which is to be expected considering the Mg rich nature of serpentinite.

While carbonates are exclusively associated with ultramafic rocks at least three different generations of carbonate can be distinguished based upon morphology and/or $\delta^{13}C$ values (Fig. 28). Table 4 below reveals a range in $\delta^{13}C_{PDB}$ from -12.29 to -4.95.

Table 4. $\delta^{13}C$ values of different generations of carbonates from the Jebel Tays massif.

Sample #	$\delta^{13}C_{PDB}$ (per mil)	Sample Type
S09-040	-12.02	Carbonate Vein
S09-058	-10.70	Carbonate Vein
S09-059	-12.29	Carbonate Vein
S09-018	-11.47	Carbonate Vein
S09-017	-10.89	Carbonate Vein
S09-025	-6.28	Massive Carbonate
S09-042	-5.61	Massive Carbonate
S09-032	-5.85	Massive Carbonate
S09-062	-5.19	Massive Carbonate + Pyrite
S09-063	-5.19	Massive Carbonate + Pyrite
S09-102	-4.95	Massive Carbonate + Pyrite
S09-091	-6.76	Cauliflower Carbonate Vein
S09-027	-7.69	Cauliflower Carbonate Vein
S09-030	-6.50	Cauliflower Carbonate Vein

The cauliflower carbonates are found as veins exclusively within the serpentinised mélange rocks and have a distinctive cauliflower morphology (Fig. 28B) and their $\delta^{13}C$ values are within the range of mantle derived carbon. Massive carbonates that form the orange rock that caps large parts of Jebel

Tays are volumetrically the most abundant carbonate and with a mean $\delta^{13}C$ value of -5.73, its isotopic composition is entirely consistent with a mantle derived carbon source (Javoy and Pineau, 1991; Javoy et al., 1986). It would seem that the fluid flow hosted zone of massive carbonate and pyrite is slightly isotopically heavier (≈0.60 per mil) than the massive carbonates that do not host pyrite, however, $\delta^{13}C$ values are still consistent with a mantle carbon source. Carbonate veins of coarse crystalline magnesite are found cross cutting the massive carbonates and while not abundant, are not rare. $\delta^{13}C$ values for these carbonate veins are significantly lighter than most reported mantle derived carbon, such isotopically light values are consistent with a carbon source derived from an organic carbon reservoir or from decarboxylation of a pre-existing carbonate.

6.1.1 Petrogenesis

What is immediately apparent from the $\delta^{13}C$ values for the massive carbonates, is that their isotopic signature is entirely consistent with a mantle source. Furthermore, field relationships between the carbonate and serpentinised rocks clearly indicates a sequence of alteration from ultramafic rock to serpentinite to carbonate. The reaction of ultramafic rock to serpentinite to carbonate is well understood and is of the general form:

$[(Fe,Mg,Ca)(Si, Al)_2O_6] + H_2O \Rightarrow Mg_3Si_2O_5(OH)_4$ [Reaction 1] (Fryer, 2002)

$Mg_3Si_2O_5(OH)_4 + 3CO_2 \Rightarrow 3MgCO_3 + 2SiO_2 + 2H_2O$ [Reaction 2]

The basis of this reaction is the influx of hydrothermal water into ultramafic rocks, the reaction is exothermic but requires elevated temperatures due to high activation energies. The reaction to form carbonates is simply the dehydration of serpentinite in the presence of CO_2, these reactions are essentially irreversible. What is clear is that reaction 2 proceeded while the rock body was still in communication with the mantle CO_2 reservoir. In regard

to the 0.6 per mil difference between massive carbonates and massive carbonate that host pyrite, I suggest that this small shift of $\delta^{13}C$ to heavier values is consistent with the interpretation of this discrete zone being a conduit for fluid flow (i.e. a fault).

Veins that cross cut the massive carbonates are isotopically light and are at the extreme range of those reported for the mantle carbon reservoir. As already discussed this suggests either carbon derived from an organic reservoir or decarboxylation of existing carbonate rocks. In all cases these veins are coarse crystalline and euhedral, suggestive of dissolution and recrystalisation in response to an increase in temperature and pressure, thus field relationships suggest that they have formed in response to a structural and/or metamorphic event. This would favour a shift to isotopically lighter compositions through decarboxylation. During this process the release of CO_2 from carbonates results in ^{13}C being preferentially incorporated into the gas phase and ^{12}C in the carbonate phase. Isotope fractionation of $\delta^{13}C$ in response to thermal decarboxylation has been found to increase exponentially with time, with fractionation factors ranging between $\Delta^{13}C_{siderite\text{-}CO2}$ ~1 to ≥5 per mil (Sharp et al., 2003), which is consistent with the observed $\Delta^{13}C$ of massive carbonates and carbonate veins, however, these reported $\Delta^{13}C$ are for the system siderite-CO_2 rather than system magnesite-CO_2. A possible driver for such decarboxylation would be the obduction of the Jebel Tays complex, this could be tested through isotopic dating (i.e. Sm-Nd, U-Pb) of the carbonate veins. The shift of the cauliflower carbonate veins, that are found exclusively within the serpentinite mélange, to values slightly lighter than the mantle reservoir may also be related to decarboxylation. The alternative to this interpretation is the reaction with an organic carbon reservoir, but this interpretation is hard to reconcile with the observed structural relationships.

7 GEOCHRONOLOGY

7.1 Abt Formation / Ad Dawadimi Basin

The Ad Dawadimi basin separates the volcanic arc terranes of the Afif and Ar Rayn and is bordered to the east by the Al Amar fault and to the west by the Halaban-Zharghat fault, the Abt Formation is the principle formation exposed within the basin. The Ad Dawadimi basin has been interpreted as a back-arc basin separating the Afif and Ar Rayn Terranes (Al-Shanti and Gass, 1983) and while the age spectrum obtained from a pebbly conglomerate sampled from the Abt Formation immediately adjacent to Jebel Tays is consistent with these zircons being derived from the Afif Terrane, an Ar Rayn component can not be excluded. The age data can be used to support both a back-arc basin model or micro-continent model. Figures 30 (A & B) present Concordia from a matrix supported pebble conglomerate and probability distribution data from 91 analysed zircons, of these 66 produced dates that were ≥ 90% concordant on the basis of their $^{207}Pb/^{235}U$ and $^{206}Pb/^{238}U$ ages. What is evident from the probability distribution plot is that this sample is dominated by Neoproterozoic and Paleoproterozoic source material. The youngest dated concordant zircon (≥90% concordant) produced a $^{206}Pb/^{238}U$ age of 596.1 ± 7.33 Ma (97% concordant) and this is supported by another two zircons with ages within error of this date, 602 ± 7.83 Ma and 606.2 ± 7.33 Ma respectively. These zircons all show oscillatory zoning characteristic of formation within a magma chamber. CL images of these zircons are shown (Fig. 29). The youngest dated zircon produced a $^{206}Pb/^{238}U$ age 548.2 ± 6.68 Ma, $^{207}Pb/^{235}U$ age of 628.4 ± 7.81 Ma and $^{207}Pb/^{206}Pb$ age of 929.4 ± 32.44 Ma. This grain is only 87% concordant and is interpreted to be an older grain that lost lead in the modern environment.

Another sample obtained from the Abt was a large (ca 20cm x 10cm) cobble clast from a matrix supported conglomerate. This was dated to obtain an igneous crystallisation age. This rock is a sub-volcanic granitoid with a graphic

intergrowth of quartz and alkali feldspar and prominent Nb depletion in its trace element pattern. Of 29 zircons analysed (Fig. 31) 13 provided ages that where better than 95% concordant with a mean $^{206}Pb/^{238}U$ age of 667.5 ± 4.9 Ma.

A compilation of ANS ages (Fig. 32) reveals a significant overlap between the Abt Neoproterozoic detrital population and the Afif and Ar Rayn Terranes which have significant populations of Neoproterozoic source rocks. However, the only known Paleoproterozoic ages for source rocks come from the Halfa (modern day Sudan) and the Khida terranes (a sub-terrane of the Afif) (Johnson and Woldehaimanot, 2003). Providence studies based solely on apparent age correlations are problematic and based solely on this age data one can not identify definitive source areas for these detrital zircons. However, at the very least it would seem highly probable that the Paleoproterozoic zircons are sourced from the Afif Terrane. The need for further data such as Hf and/or Nd isotopic correlations to firmly establish source regions has been established (Howard et al., 2009) and this would be particularly powerful as there is a wide spread of ε_{Nd} values across the ANS, ranging from -27 to +8.9 (Johnson and Woldehaimanot, 2003) and would potentially more clearly define source regions. This would have implications for the tectonic setting for the Ad Dawadimi basin that has been interpreted as both a back-arc basin and as a forearc mélange. Regardless of the likely source regions, the data is consistent with a maximum depositional age of ca 600 Ma making the Abt Ediacaran in age, this is in general agreement with previously published detrital work (Johnson and Kattan, 2008) but refutes work based on $^{40}Ar/^{39}Ar$ dating of metagabbros and amphibolites from the Halaban ophiolite that had been used to constrain the deposition of the Abt Formation to 680 Ma (Al-Saleh and Boyle, 2001b).

7.2 Jebel Tays Gabbro

As previously discussed, the gabbros of Jebel Tays are subduction related mafics (low Ti-IAT) with forearc affinity, thus dating of these rocks provides a timeframe for when primitive subduction magmatism was occurring.

Zircons obtained from a single gabbro sample were dated via LA-ICP-MS, the zircons on the whole were large (>200 μm) and while most were fractured their original euhedral shape could be observed. Many of the sampled zircons showed little to no zoning while others show a metamict appearance, the larger zircons however, revealed oscillatory zoning typical of an igneous origin (Fig. 33C).

The data consisted of 45 individual analysis spots along with 25 analysis spots on the GJ zircon standard. Figure 33A is a concordia plot for all 45 zircons, it is clear from these data that both lead loss, common lead and inheritance are present in the sample. However, the combination of these data produces a lower intercept age of 669.2 ± 2.8 Ma with a mean standard weighted deviation of 2.8, this MSWD provides statistical evidence of multiple zircon populations. Of the 45 analysed zircons, 17 produced dates that were better than 90% concordant and 15 were better than 95% concordant. Figure 33B is the concordia plot based on those zircons that were ≥95% concordant, this first pass filter removed the analysis spots that showed lead loss and inheritance revealing a tight grouping of concordant data that are all within error of each other. A mean weighted average $^{206}Pb/^{238}U$ age was calculated at 678 ± 5 Ma (2σ) and a MSWD of 0.62 providing evidence for a single zircon population. Figure 33C shows representative zircons of this group, they are all characterised by a euhedral shape, intermediate CL response and clear oscillatory zoning indicative of an igneous origin. Therefore we interpret this 678 ± 5 Ma (2σ) to be the crystallisation age for this gabbro.

7.3 Trondhjemitic, Tonalitic and Granodioritic Granite and Dykes

The intrusive and extrusive rocks of trondhjemitic, tonalitic and granodioritic composition appear un-metamorphosed (no fabric) and cross cut both the gabbro and ultramafic sequences of Jebel Tays. Figure 34A presents the concordia diagram for 48 analysed zircons, the spread up and down the concordia provides evidence of inheritance while a few zircons exhibit lead loss and a common lead trend is also evident. Interestingly, 5 zircons not shown on this concordia gave concordant Mesoproterozoic (1 zircon) Paleoproterozoic (2 zircons) and Neo/Mesoarchaean ages (2 zircons). Proterozoic dates are explained easily as much of the ANS is composed of Proterozoic terranes, however, the 2 Mesoarchaean ages, which are ≥95% concordant, are anomalous as no Archaean terranes are known in the ANS. The CL images for these zircons are shown in Figure 35 and reveal that the respective analyses came from oscillatory zoned areas and thus represent igneous crystallisation dates.

As a first pass filter on these data, Figure 34B is the concordia of those zircons that are ≥ 95% concordant, from this group a meaningless lower intercept age of 646 ± 34 Ma with a MSWD of 104 was obtained based on a common lead trend. A simple inspection of the concordia suggested at least three age groupings and a probability density plot of these zircons statistically confirms the visual appearance of three distinct population peaks. The youngest group produced a $^{206}Pb/^{238}U$ mean weighted age of 632.6 ± 8.0 Ma (2σ) with MSWD of 0.67 indicating that this peak statistically represents a single age population. This is further evidenced by zircon morphology and CL response that show a characteristic highly elongated euhedral morphology, high CL response and oscillatory zoning from this young zircon population (Fig. 36). This $^{206}Pb/^{238}U$ age of 632.6 ± 8.0 Ma is comprised of 11 individual zircons and is interpreted as the crystallisation age of this trondhjemite. This

crystallisation age supports a previous Rb-Sr whole rock age of 620 ± 40 Ma (Al-Shanti et al., 1984).

Further to the above crystallisation date, monazites were obtained from the fine grained chilled margin of the main body of the trondhjemite intrusion. While many of the analysed monazites showed common lead, these discordant grains, along with near concordant dates from other monazites produced a lower intercept age of 593 ± 15 Ma. Furthermore, a mean $^{206}Pb/^{238}U$ age of 599.8 ± 5.8 Ma (2σ) was obtained on 9 concordant analyses (Fig. 37).

Due to the lack of any metamorphic fabric in any of the exposed trondhjemites it could be argued that these are in fact igneous monazites, furthermore, by virtue of this interpretation we would have to draw the unlikely conclusion that all of the analysed zircons are inherited. However, the lack of any zoning in these monazites and the fact that the 599.8 ± 5.8 Ma age is within error of previous published $^{40}Ar/^{39}Ar$ dates of 596 ± 6 Ma and 611 ± 8 Ma that are interpreted as a regional metamorphic event (Al-Saleh et al., 1998) suggests these are metamorphic monazites. The growth of these monazites are most likely related to extensive fluid flow, evidence for this can be seen in a few rocks that show redox flow banding and the presence of epidote and muscovite revealed in thin section. The lack of a metamorphic fabric, considering the pervasive fabrics that permeate most ultramafic rocks can not be interpreted as these rocks post-dating basin closure, furthermore, this is not unique, many of the exposed gabbros are isotropic and contain no metamorphic fabric.

7.4 Halaban Diorite

To further constrain igneous activity within the Ad Dawadimi basin, diorites that form part of the Halaban ophiolite were dated. These rocks crop out along the roadside cutting immediately west of Halaban village and are located ca 64 km north-west of Jebel Tays. These rocks are volumetrically the most

abundant outcropping mafic rocks within the Ad Dawadimi basin and represent a component of one of the largest ophiolites of the ANS. Dating of 29 zircon grains produced ages with a spread between 643 Ma to 707 Ma (Fig. 38), most of which where close to concordant and most showed complex zoning. A lower intercept age of 667.3 ± 8.6 Ma was obtained. As previously, this data set was reduced to only those zircons that were ≥95% concordant resulting in 16 zircons with ages between 661 Ma to 707 Ma with a mean weighted $^{206}Pb/^{238}U$ age of 676.0 ± 6.9 Ma (2σ), once again a calculated intercept age produced an age of 676.2 ± 6.9 Ma with a MSWD of 1.8 but, as can be seen (Fig. 38), a considerable spread remained in the data. Utilising the youngest 11 zircons that lie within error of each other produced a mean weighted $^{206}Pb/^{238}U$ age of 674.4 ± 5.8 Ma (2σ) Ma with a MSWD of 0.53 statistically suggestive of a single zircon population. This age has been interpreted as the crystallisation age making the generation of these melts broadly coeval with the gabbros at Jebel Tays. This age is younger than a previous published intercept age of 694 ± 8 Ma based on 2 analysed zircons (Stacey et al., 1984) for a gabbro from the same region.

8 DISCUSSION

8.1 Geochronological Framework

It is widely documented that the basement terrane of the ANS generally youngs towards the east and represents a series of accreted island arcs associated with the amalgamation of Gondwana (Johnson and Kattan, 2008; Johnson and Woldehaimanot, 2003). The temporal importance of the Ad Dawadimi basin relates to:

1. Ad Dawadimi basin representing the youngest exposed accretion event of the exposed ANS and…
2. The depositional age of the Abt Formation has important implications for the age of the likely Neoproterozoic Jibilah basins that contain putative metazoan fossils (Nettle, 2009).

Figure 39 presents a compilation of age data from literature and this study. The importance of this study is that it provides robust age dates on the crystallisation of primitive mafic magmatism and adds a robust monazite date in support of previous $^{40}Ar/^{39}Ar$ ages.

Based on this compilation the following geochronological framework is proposed:

1. >700 Ma – Andean Style Arc Volcanism
   Associated with the Afif and Ar Rayn Terranes indicative of active subduction.
2. ca 680 Ma – 670 Ma – Ultramafic and Mafic Magmatism
   Represented by the Jebel Tays and Halaban ophiolites.
3. ca 680 Ma Metamorphic Event
   This $^{40}Ar/^{39}Ar$ age is based on amphiboles of the Halaban ophiolite and has been interpreted as basin closure and previously used to constrain the deposition of the Abt Formation (Al-Saleh et al., 1998). In light of detrital zircon data from the Abt Formation (this study) and the age of

primary magmatism associated with the Halaban ophiolite (this study) we interpret this $^{40}Ar/^{39}Ar$ date to be associated with the obduction of the Halaban ophiolite and thus does not represent basin closure. This interpretation is consistent with the view that most ophiolites are generally coeval with their metamorphic soles (Wakabayashi and Dilek, 2000).

4. ca 670 Ma – 630 Ma – Arc Volcanism
   Associated with the Ar Rayn Terrane and indicates active subduction outboard of the Ar Rayn.
5. ca 630 Ma – 600 Ma – Intrusion of Syn-collisional Granites
   Associated with final stages of collision between the Afif and Ar Rayn Terranes.
6. ca 600 Ma – Final Basin Closure
   Closure of the Ad Dawadimi basin, supported by numerous $^{40}Ar/^{39}Ar$ ages as well as a new monazite date (this study).

Due to the low temperature nature of the contact between Jebel Tays and the Abt Schist the timing of its obduction is poorly constrained but must be between ca 632 Ma (the crystallisation age of the intruding trondhjemite) and basin closure at ca 600 Ma.

8.2 Structural and Tectonic Interpretation of Jebel Tays

As discussed earlier, I interpret Jebel Tays as the product of forearc magmatism along with serpentinised peridotite, which has subsequently been transported within a serpentinite mud matrix along west dipping thrust structures. Previously bodies such as Jebel Tays would most likely be characterised as mélanges, however, significant work has been done on the occurrence of serpentinites within forearc trenches, from such work it would seem that the formation of such serpentinised ultramafic/mafic bodies are the result of serpentine mud volcanism in convergent margin tectonic settings. Fryer *et al.* (2000) describe these bodies as chaotic mélanges that have virtually no contact aureole (sub-greenschist) with their surrounding rocks, display extensive internal shearing and contain clasts of mafic rocks. The serpentinite mélange that protrudes east of the main body (Fig. 6) of Jebel Tays and forms much of the mélange in the gullies that cut into the main body is a perfect example of just such an occurrence. Figure 40 clearly shows examples of entrained mafic and ultramafic clasts within highly sheared fine grained serpentinite mud.

Such occurrences of forearc serpentinite mud volcanism are observed within the Mariana trench where dredge samples composed of serpentinised peridotite have been obtained from large (20km x 50km x 3km) edifices that stretch out along the Izu-Bonin-Mariana IBM volcanic front (Fryer, 2002). Such large edifices suggest that such serpentinisation can be widespread and that significant amounts of mantle material is either exposed or brought to the surface in deep forearc trenches.

The mechanism Fryer (2000) invokes for such serpentinite mud volcanism involves serpentinised mud flowing up fault controlled horst and graben structures in the overriding plate entraining mafic clasts on its ways before being deposited on top of forearc sediments. This explains the western serpentinite mélange and much of the main body of Jebel Tays but seems

inadequate for the kilometre scale gabbroic bodies exposed north and south of Jebel Tays. However, research as part of the ODP (Leg 125) (Fryer, 1992) found that many of the horst blocks are actually highly faulted serpentinised mantle and lower crustal intrusives. While admittedly speculative we envisage that in the case of Jebel Tays these horst blocks are gabbroic blocks that have been thrusted up and over the forearc Abt sediments, at the same time serpentinite mud has flowed up associated faults and as serpentinite diapirs to form the volumetrically abundant serpentinite mud and mélange. Schematically this model is shown in Figure 41.

This model has remarkable similarities with the observed units at Jebel Tays, in particular this model envisages faults filled with serpentinite mud material and exhibit low greenschist to sub-greenschist facies metamorphism rather than the typical amphibolite facies metamorphic soles associated with many obducted ophiolites. At Jebel Tays this is exactly what is observed, all thrust contacts involve serpentinite mélange, never do we observe gabbro blocks in thrust contact with the surrounding sediments and metamorphism of this contact is sub-greenschist, this last point can not be over-emphasised, clearly its emplacement onto the surrounding sediments was cold. At some time during these events but while in communication with the mantle carbon reservoir much of the serpentinite has been transformed to carbonate. Finally these serpentinite mélanges and gabbroic blocks have been remobilised as a part of the accretionary wedge that is now the Ad Dawadimi basin. As discussed earlier, structurally and stratigraphically it seems likely that the easterly thrust is the oldest, thrusting the ophiolitic rocks over the Abt sediments and this was latter followed by the westerly thrust of the Abt over the ophiolitic thrust sheet. However, I have no constraints on the absolute timing between these events.

Importantly this type of forearc serpentinite volcanism and horst block thrusting may not be limited to Jebel Tays, at least two other Ad Dawadimi basin ophiolitic bodies have been described as serpentinised mélanges, the

Ar Ridayniyah mélange (Al-Saleh and Boyle, 2001b) and Al Amar-Idsas mélange zone (Al-Shanti and Gass, 1983) and may well be ophiolitic bodies of a similar origin as proposed for Jebel Tays.

8.3 Regional Tectonic Interpretation

From a regional perspective Jebel Tays sits within a sedimentary basin (Ad Dawadimi basin) composed of metapelitic sediments whose protolith must have been immature silts and sands with minor conglomerates, this is entirely consistent with a marginal basin or forearc environment. The Ad Dawadimi basin separates the Afif Terrane to the west and the Ar Rayn Terrane to the east. Based on the ages of arc magmatism in these adjacent terranes and the widespread occurrence of ophiolites within the Ad Dawadimi basin, specifically mafic melts dated at ca 670-680 Ma (this study), must mean that two subduction zones existed at this time, one inboard of the Ar Rayn and one outboard of the Ar Rayn. The west dipping nature of the foliations and thrusts along with top to the east kinematics at Jebel Tays all suggest a west dipping subduction zone within this basin, this implies that the outboard subduction zone was also west dipping. Thus on the regional scale the Ad Dawadimi basin represents a back-arc basin or forearc basin between the Afif and Ar Rayn Terranes.

While stratigraphically Jebel Tays sits within the Ad Dawadimi basin the primary control on its original tectonic setting and obduction is the boninitic series magmatism recorded by the exposed mafic rocks and the forearc affinity of the preserved peridotites and chrome spinels. Kim and Jacobi (2002) list five major settings for boninitic magma genesis, three of which are restricted to forearcs, these include:

1. Subduction of an active spreading ridge.
2. Subduction initiation.
3. Forearc Spreading.

Furthermore, the need to accommodate the extensive magmatism of the Halaban ophiolite must also be compatible with any tectonic model. Geochemical work on the Halaban is limited but Al-Saleh & Boyle (2001a) published major and trace data on eight gabbro samples. On numerous discriminant diagrams these all plot within the field of island arc tholeiites (IAT) and exhibited prominent Nb anomalies. In contrast to the gabbros exposed at Jebel Tays, these Halaban gabbros are high Ti IAT (>1 weight % TiO_2) and showed negative gradients in their respective normalised REE plots. The single dated sample (this study) indicates that this magmatism is broadly coeval with magmatism at Jebel Tays. Below we propose two tectonic models which seem consistent with the above structural, geochemical and chronological constraints.

8.3.1 Model 1 – Back-arc Basin Magmatism

1. *700 Ma*
   Arc magmatism occurring within the Afif Terrane due to a west dipping subduction system.
2. *>680 Ma*
   Slab roll back places Afif margin into extension, resulting in arc splitting and the opening of a back-arc, this arc splitting shifts the volcanic front to the east resulting in Ar Rayn arc magmatism. Deposition of Abt sediments starts within the newly formed back-arc basin, sediments are sourced from both Afif and Ar Rayn Terranes.
3. *ca 680 Ma - 670 Ma*
   Subduction initiation within back-arc basin produces low Ti IAT magmatism of Jebel Tays, mafic IAT magmatism of the overriding back-arc plate produces the proto-ophiolite of the Halaban.
4. *ca 630 Ma*
   Jebel Tays intruded by adakitic magma. Sometime between 630 Ma and 600 Ma rocks of Jebel Tays obducted as a forearc thrust sheet.
5. *ca 600 Ma*
   Basin Closure.

Schematically this tectonic model is shown in Figure 42 and is broadly consistent with models put forward by Al-Saleh and Boyle (2001a) and Nawab (1979).

8.3.2 Model 2 - Forearc Magmatism and Ar Rayn Micro-continent

1. *>700 Ma*
   Subduction under the Afif producing arc magmatism, the Ar Rayn is an outboard micro-continent also undergoing arc magmatism.
2. *ca 680 Ma - 670 Ma*
   Afif forearc extension / slab roll back produces low Ti IAT magmatism along with IAT magmatism in the advancing volcanic front. Obduction of Halaban IAT rocks to form proto-ophiolite.
3. *ca 630 Ma – 600 Ma*
   Adakitic magmatism and obduction of Jebel Tays, continued Ar Rayn arc magmatism.
4. *ca 600 Ma*
   Collision of the Ar Rayn micro-continent with the Afif.

Schematically this tectonic model is shown in Figure 43, this model is an extension of the Ar Rayn micro-continent model proposed by Stoeser & Camp (1985).

8.3.3 Model Comparisons

In many respects both models produce very similar end results, both are consistent with the detrital zircon age spectrum for the Abt Formation suggesting sediments sourced from both terranes, both allow for magmatism with boninitic affinity and both are consistent with the obduction mechanism outlined for Jebel Tays. Model 1 requires the back-arc to be very marginal to explain why the Halaban ophiolite has IAT rather than BABB chemistry. Stoeser and Camp (1985) proposed this original micro-continent model based on the differences in Pb isotopes between the Afif and Ar Rayn, arguing that such differences make the idea of the Ar Rayn being a rifted segment of the

Afif unlikely. This isotopic argument is persuasive, but recent isotopic work (Stoeser and Frost, 2006) has shown the entire Afif to be a composite terrane, this could be interpreted as evidence for the multiple episodes of micro-continent amalgamation throughout the Proterozoic. However, I also see no geologic reason why such amalgamated terranes could not have been rifted apart along re-activated sutures in the past to form numerous back-arc basins. However, with three identified ophiolitic bodies within the Ad Dawadimi basin, the requirement for two subducting slabs within the back-arc of any proposed back arc model, the IAT chemistry of the Halaban rather than BABB chemistry or E-MORB and previous Pb isotope data, I believe the combination of this evidence is more simply explained with micro-continent terrane amalgamation. Thus we interpret the entire Ad Dawadimi basin as a forearc basin.

9 CONCLUSION

Jebel Tays represents an ophiolitic thrust sheet that has been transported along west dipping thrust structures accompanied by extensive serpentinite mud volcanism. Jebel Tays does not fit within the traditional interpretation of ophiolites being fragments of oceanic crust generated at mid ocean ridges, rather the mafic magmatism associated with Jebel Tays has clear forearc affinity precluding a mid ocean ridge tectonic setting. This forearc affinity also distinguishes it from the volumetrically abundant mafic magmatism associated with the nearby Halaban ophiolite. Therefore Jebel Tays is an example of a forearc ophiolite emplaced within the interface between the upper overriding plate and the subducting slab. The identification of Jebel Tays as a forearc ophiolite constrains the Ad Dawadimi basin to the forearc of the Afif and thus conclude that the Ad Dawadimi is best described as forearc basin. Detrital zircon ages constrain the Ad Dawadimi sediments to being Ediacaran in age and clearly point to basin closure and the docking of the Ar Rayn micro-continent with the Afif at ca 600Ma.

10 REFERENCES

Al-Saleh, A.M. and Boyle, A.P., 2001a. Neoproterozoic ensialic back-arc spreading in the eastern Arabian Shield: geochemical evidence from the Halaban Ophiolite Journal of Afrrcan Earth Sciences,, 33(1).

Al-Saleh, A.M. and Boyle, A.P., 2001b. Structural rejuvenation of the eastern Arbian Shield during continental collision: 40Ar/40Ar evidence from the Ar Ridayniyah ophiolitic melange. Journal of African Earth Sciences, 33(1): 135-141.

Al-Saleh, A.M., Boyle, A.P. and Mussett, A.E., 1998. Metamorphism and 40Ar/39Ar dating of the Halaban Ophiolite and associated units: evidence for two-stage orogenesis in the eastern Arabian Shield. Journal of the Geological Society, 155(1): 165-175.

Al-Shanti, A.M. and Gass, I.G., 1983. The Upper Proterozoic ophiolite melange zones of the easternmost Arabian shield. Journal of the Geological Society, 140(6): 867-876.

Al-Shanti, A.M.S., Abdel-Monem, A.A. and Marzouki, F.H., 1984. Geochemistry, petrology and Rb-Sr dating of trondhjemite and granophyre associated with Jabal Tays Ophiolite, Idsas area, Saudi Arabia. Precambrian Research, 24(3-4): 321-334.

Anonymous, 1972. Penrose Field Conference on Ophiolites, Penrose Field Conference on Ophiolites. Geological Society of America, pp. 24-25.

Azer, M.K. and Stern, R.J., 2007. Neoproterozoic (835-720 Ma) Serpentinites in the Eastern Desert, Egypt: Fragments of Forearc Mantle. Journal of Geology, 115(4): 457-472.

Barker, F. (Editor), 1979. Trondhjemites: definition, environment and hypotheses of origin. Trondhjemites, Dacites and Related Rocks. Elsevier, Amsterdam.

Barnes, S.J. and Roeder, P.L., 2001. The Range of Spinel Compositions in Terrestrial Mafic and Ultramafic Rocks. J. Petrology, 42(12): 2279-2302.

Barth, M.G., Foley, S.F. and Horn, I., 2002. Partial melting in Archean subduction zones: constraints from experimentally determined trace element partition coefficients between eclogitic minerals and tonalitic melts under upper mantle conditions. Precambrian Research, 113(3-4): 323-340.

Bedard, J.H., Lauziere, K., Tremblay, A. and Sangster, A., 1998. Evidence for forearc seafloor-spreading from the Betts Cove ophiolite, Newfoundland: oceanic crust of boninitic affinity. Tectonophysics, 284(3-4): 233-245.

Blundy, J.D. and Wood, B.J., 1991. Crystal-chemical controls on the partitioning of Sr and Ba between plagioclase feldspar, silicate melts, and hydrothermal solutions. Geochimica et Cosmochimica Acta, 55(1): 193-209.

Chew, D.M., 2003. An Excel spreadsheet for finite strain analysis using the Rf/[phi] technique. Computers & Geosciences, 29(6): 795-799.

Claesson, S., Pallister, J.S. and Tatsumoto, M., 1984. Samarium-neodymium data on two late Proterozoic ophiolites of Saudi Arabia and implications for crustal and mantle evolution. Contributions to Mineralogy and Petrology, 85(3): 244-252.
Coleman, R.G., Peterman, Z.E. , 1975. Oceanic Plagiogranite. Journal of Geophysical Research, 80(8): 1099-1108.
Collins, A.S. and Pisarevsky, S.A., 2005. Amalgamating eastern Gondwana: The evolution of the Circum-Indian Orogens. Earth-Science Reviews, 71(3-4): 229-270.
Dare, S.A.S., Pearce, J.A., McDonald, I. and Styles, M.T., 2009. Tectonic discrimination of peridotites using fO2-Cr# and Ga-Ti-FeIII systematics in chrome-spinel. Chemical Geology, 261(3-4): 199-216.
Defant, M.J. and Drummond, M.S., 1990. Derivation of some modern arc magmas by melting of young subducted lithosphere. Nature, 347(6294): 662-665.
Delfour, J., 1979. Explanatory notes to the geologic map of the Halaban quadrangle, Sheet 23G, Kingdom of Saudi Arabia, Bureau de Recherches Geologiques et Minieres, Orleans.
DePaolo, D.J., 1980. Crustal growth and mantle evolution: inferences from models of element transport and Nd and Sr isotopes. Geochimica et Cosmochimica Acta, 44(8): 1185-1196.
Dick, H.J.B. and Bullen, T., 1984. Chromian spinel as a petrogenetic indicator in abyssal and alpine-type peridotites and spatially associated lavas. Contributions to Mineralogy and Petrology, 86(1): 54-76.
Dunnet, D., 1969. A technique of finite strain analysis using elliptical particles. Tectonophysics, 7(2): 117-136.
Falloon, T.J. and Danyushevsky, L.V., 2000. Melting of Refractory Mantle at 1.5, 2 and 2.5 GPa under Anhydrous and H2O-undersaturated Conditions: Implications for the Petrogenesis of High-Ca Boninites and the Influence of Subduction Components on Mantle Melting. J. Petrology, 41(2): 257-283.
Fryer, P., 1992. A synthesis of Leg 125 drilling of serpentine seamounts on the Mariana and Izu-Bonin forearcs. Proceedings of the Ocean Drilling Program - Scientific Results Leg 125. Ocean Drilling Program, College Station, Texas, 593-614 pp.
Fryer, P., 2002. Recent studies of serpentinite occurences in the mantle-ocean interactions in the plate tectonic cycle. Chemie der Erde Geochemistry, 62(4): 257-302.
Fryer, P., Lockwood, J.P., Becker, N., Phipps, S. and Todd, C.S., 2000. Significance of serpentine mud volcanism in convergent margins. Geological Society of America Special Paper 349: 35-51.
Goldstein, S.L., O'Nions, R.K. and Hamilton, P.J., 1984. A Sm-Nd isotopic study of atmospheric dusts and particulates from major river systems. Earth and Planetary Science Letters, 70(2): 221-236.
Henderson, P. and Suddaby, P., 1971. The nature and origin of the chrome-spinel of the Rhum layered intrusion. Contributions to Mineralogy and Petrology, 33(1): 21-31.

Howard, K.E. et al., 2009. Detrital zircon ages: Improving interpretation via Nd and Hf isotopic data. Chemical Geology, 262(3-4): 277-292.
Ishikawa, T., Nagaishi, K. and Umino, S., 2002. Boninitic volcanism in the Oman ophiolite: Implications for thermal condition during transition from spreading ridge to arc. Geology, 30(10): 899-902.
Jackson, S.E., Pearson, N.J., Griffin, W.L. and Belousova, E.A., 2004. The application of laser ablation-inductively coupled plasma-mass spectrometry to in situ U-Pb zircon geochronology. Chemical Geology, 211(1-2): 47-69.
Jacobsen, S.B. and Wasserburg, G.J., 1979. The mean age of mantle and crustal reservoirs. Journal of Geophysical Research, 84: 7411-7427.
Javoy, M. and Pineau, F., 1991. The volatiles record of a "popping" rock from the Mid-Atlantic Ridge at 14∞N: chemical and isotopic composition of gas trapped in the vesicles. Earth and Planetary Science Letters, 107(3-4): 598-611.
Javoy, M., Pineau, F. and Delorme, H., 1986. Carbon and nitrogen isotopes in the mantle. Chemical Geology, 57(1-2): 41-62.
Johnson, P., 2006. Explanatory Notes to the Map of Proterozoic Geology of Western Saudi Arabia - Technical Report SGS-TR-2006-4, Saudi Geological Survey.
Johnson, P. and Kattan, F., 2008. Lithostratigraphic revision in the Arabian Shield: The impacts of geochronology and tectonic analysis. The Arabian Journal for Science and Engineering, 33(1C).
Johnson, P., Kattan, F. and Al-Saleh, A.M., 2004. Neoproterozoic ophiolites in the Arabian Shield: Field relations and structure. Precambrian Ophiolites and Related Rocks.
Johnson, P. and Woldehaimanot, B., 2003. Development of the Arabian-Nubian Shield: perspectives on accretion and deformation in the northern East African Orogen and the assembly of Gondwana. Proterozoic East Gondwana: Supercontinent Assembly and Breakup, Special Publication 206. Geological Society of London.
Kerrich, R., Wyman, D., Fan, J. and Bleeker, W., 1998. Boninite series: low Ti-tholeiite associations from the 2.7 Ga Abitibi greenstone belt. Earth and Planetary Science Letters, 164(1-2): 303-316.
Kim, J. and Jacobi, R., 2002. Boninites: characteristics and tectonic constraints, northeastern Appaachians. Physics and Chemistry of the Earth, 27: 109-127.
Klein, M., Seck, H, Stosch, H, Shimizu, N, 1994. Experimental REE partitioning between amphibole, clinopyroxene, garnet and basaltic to tonalitic melts: applications to the tonalite genesis. Goldschmidt Conference Edinburgh.
Klemme, S., Blundy, J.D. and Wood, B.J., 2002. Experimental constraints on major and trace element partitioning during partial melting of eclogite. Geochimica et Cosmochimica Acta, 66(17): 3109-3123.
Koepke, J., Berndt, J., Feig, S. and Holtz, F., 2007. The formation of SiO2-rich melts within the deep oceanic crust by hydrous partial melting of gabbros. Contributions to Mineralogy and Petrology, 153(1): 67-84.

Koepke, J., Feig, S., Snow, J. and Freise, M., 2004. Petrogenesis of oceanic plagiogranites by partial melting of gabbros: an experimental study. Contributions to Mineralogy and Petrology, 146(4): 414-432.
Le Maitre, R.W., 1989. A classification of igneous rocks and glossary of terms (IUGS): recommendations of the IUGS Subcommission on the Systematics of Igneous Rocks. Blackwell, Oxford.
Lehnert, K., Su, Y., Langmuir, C., Sarbas, B. and Nohl, U., 2000. A global geochemical database structure for rocks. Geochemistry, Geophysics, Geosytems.
Lisle, R.J., 1985. Geological Strain Analysis: A Manual for the Rf/phi Technique. Pergamon Press, Oxford, 99 pp.
Ludwig, K.R., 2009. Isoplot Ver:3.0.
Macpherson, C. and Hall, R., 2001. Tectonic setting of Eocene boninite magmatism in the Izu-Bonin-Mariana forearc. Earth and Planetary Science Letters, 186(2): 215-230.
Malpas, J. and Strong, D.F., 1974. A comparison of chrome-spinels in ophiolites and mantle diapirs of Newfoundland. Geochimica et Cosmochimica Acta, 39(6-7): 1045-1060.
Martin, H., 1999. Adakitic magmas: modern analogues of Archaean granitoids. Lithos, 46(3): 411-429.
Martin, H., Smithies, R.H., Rapp, R., Moyen, J.F. and Champion, D., 2005. An overview of adakite, tonalite-trondhjemite-granodiorite (TTG), and sanukitoid: relationships and some implications for crustal evolution. Lithos, 79(1-2): 1-24.
Max Planck Institute, 2009. Geochemistry of Rocks of the Oceans and Continents. Max Planck Institute.
Melcher, F. and Meisel, T., 2004. A Metamorphosed Early Cambrian Crust-Mantle Transition in the Eastern Alps, Austria. J. Petrology, 45(8): 1689-1723.
Nawab, Z.A., 1979. Geology of the Al-Amar-Idsas region of the Arabian Shield. Institute of Applied Geology (Jeddah) Bulletin, 3(2): 29-40.
Nettle, D., 2009. A Sequence Stratigraphic, Geochronological and Chemostratigraphic investigation of the Ediacaran Antaq Basin, Western Arabian Shield, Saudi Arabia , University of Adelaide, Adelaide.
O'Hanley, D.S., 1996. Serpentinites: Records of tectonic and petrological history. Oxford Monographs on Geology and Geophysics, 34: 277.
Payne, J.L., Hand, M., Barovich, K.M. and Wade, B.P., 2008. Temporal constraints on the timing of high-grade metamorphism in the northern Gawler Craton: implications for assembly of the Australian Proterozoic. Australian Journal of Earth Sciences: An International Geoscience Journal of the Geological Society of Australia, 55(5): 623 - 640.
Pearce, J.A., 2008. Geochemical fingerprinting of oceanic basalts with applications to ophiolite classification and the search for Archean oceanic crust. Lithos, 100(1-4): 14-48.
Pearce, J.A., Harris, N.B.W. and Tindle, A.G., 1984a. Trace Element Discrimination Diagrams for the Tectonic Interpretation of Granitic Rocks. J. Petrology, 25(4): 956-983.

Pearce, J.A., Lippard, S.J. and Roberts, S., 1984b. Characteristics and tectonic significance of suprasubduction zone ophiolites. Geological Society of London Special Publication, 16: 77-94.
Pearce, J.A. and Peate, D.W., 1995. Tectonic Implications of the Composition of Volcanic ARC Magmas. Annual Review of Earth and Planetary Sciences, 23(1): 251-285.
Plank, T., 2007. Arcs create or inherit the continents? Geochimica et Cosmochimica Acta, 70(18, Supplement 1): A496-A496.
Plank, T., Cooper, L.B. and Manning, C.E., 2009. Emerging geothermometers for estimating slab surface temperatures. Nature Geosci, 2(9): 611-615.
Power, M.R., Pirrie, D., Andersen, J.C.ò. and Wheeler, P.D., 2000. Testing the validity of chrome spinel chemistry as a provenance and petrogenetic indicator. Geology, 28(11): 1027-1030.
Rapp, R.P., Shimizu, N., Norman, M.D. and Applegate, G.S., 1999. Reaction between slab-derived melts and peridotite in the mantle wedge: experimental constraints at 3.8 GPa. Chemical Geology, 160(4): 335-356.
Sharp, Z.D., Papike, J.J. and Durakiewicz, T., 2003. The effect of thermal decarbonation on stable isotope compositions of carbonates. American Mineralogist, 88(1): 87-92.
Sorensen, S.S., 1987. Metasomatism and partial melting in a subduction complex; Catalina Schist, Southern California. Geolog, 15(2): 115.
Sorensen, S.S., 1988. Petrology of amphibolite-facies mafic and ultramafic rocks from the Catalina Schist, southern California: metasomatism and migmatization in a subduction zone metamorphic setting. Journal of Metamorphic Geology, 6(4): 405-435.
Spulber, S.D. and Rutherford, M., 1983. The Origin of Rhyolite and Plagiogranite in Oceanic Crust: An Experimental Study. J. Petrology, 24(1): 1-a-25.
Stacey, J.S., Stoeser, D.B., Greenwood, W.R. and Fischer, L.B., 1984. U-Pb zircon geochronology and geological evolution of the Halaban-Al Amar region of the Eastern Arabian Shield, Kingdom of Saudi Arabia. Journal of the Geological Society, 141(6): 1043-1055.
Stern, R.J., Johnson, P., Kroner, A. and Yibas, B., 2004. Neoproterozoic ophiolites of the Arabian-Nubian Shield. Precambrian Ophiolites and Related Rocks, 13: 95-128.
Stoeser, D.B. and Camp, V.E., 1985. Pan-African microplate accretion of the Arabian Shield. Geological Society of America Bulletin, 96(7): 817-826.
Stoeser, D.B. and Frost, C.D., 2006. Nd, Pb, Sr, and O isotopic characterization of Saudi Arabian Shield terranes. Chemical Geology, 226(3-4): 163-188.
Streckeisen, A., 1974. Classification and nomenclature of plutonic rocks recommendations of the IUGS subcommission on the systematics of Igneous Rocks. International Journal of Earth Sciences, 63(2): 773-786.

Sun, S.-s. and McDonough, W.F., 1989. Chemical and isotopic systematics of oceanic basalts: implications for mantle composition and processes. Geological Society, London, Special Publications, 42(1): 313-345.
Tanaka, T. et al., 2000. JNdi-1: a neodymium isotopic reference in consistency with LaJolla neodymium. Chemical Geology, 168(3-4): 279-281.
Taylor, R.N. et al., 1994. Mineralogy, Chemistry, and Genesis of the Boninite Series Volcanics, Chichijima, Bonin Islands, Japan. J. Petrology, 35(3): 577-617.
van Keken, P. and Kiefer, B., 2002. High-resolution models of subduction zones: Implications for mineral dehydration reactions and the transport of water into the deep mantle. Geochemistry, Geophysics, Geosytems(3).
Wade, B.P., Hand, M., Maidment, D.W., Close, D.F. and Scrimgeour, I.R., 2008. Origin of metasedimentary and igneous rocks from the Entia Dome, eastern Arunta region, central Australia: a U and Pb LA-ICPMS, SHRIMP and Sm and Nd isotope study. Australian Journal of Earth Sciences: An International Geoscience Journal of the Geological Society of Australia, 55(5): 703 - 719.
Wakabayashi, J. and Dilek, Y., 2000. Spatial and temporal relationships between ophiolites and their metamorphic soles: A test of models of forearc ophiolite genesis. Special Paper 349: Ophiolites and oceanic crust: new insights from field studies and the Ocean Drilling Program, 349(0): 53-64.
Worku, H., 1996. Geodynamic development of the Adola Belt (Southern Ethiopia) in the neoproterozoic and its control on gold mineralisation. Verlag Dr. Koster: 156.
Zhang, S.-B. et al., 2009. Origin of TTG-like rocks from anatexis of ancient thickened crust: Geochemical evidence from Neoproterozoic granitoids in South China. Lithos, In Press, Accepted Manuscript.
Zimmer, M., Kroner, A., Jochum, K.P., Reischmann, T. and Todt, W., 1995. The Gabal Gerf complex: A precambrian N-MORB ophiolite in the Nubian Shield, NE Africa. Chemical Geology, 123(1-4): 29-51.

11.2 S09-108 Zircon Age Data

Sample Name: **S09-108** **Jebel Tays Gabbro**
GPS Co-Ordinates: **Latitude (N)** **23.05286**
Longitude (E) **44.98439**

Spot	1 Sigma Age (My)				1 Sigma Uncertainty (My)			
	Pb207/Pb206	Pb206/U238	Pb207/U235	Pb208/Th232	Pb207/Pb206	Pb206/U238	Pb207/U235	Pb208/Th232
GJ01	617.1	597.9	601.9	551.2	32.31	8.26	7.94	28.94
GJ02	621.4	602.8	606.7	635	31.09	8.27	7.77	30.5
GJ03	585.3	600.2	597.1	670.4	31.88	8.26	7.79	31.23
BJWP01	731.9	733.8	733.2	744.4	35.03	10.23	9.78	15.3
spot11r	1720	682.2	978.3	986.4	37.81	10.44	13.64	20.67
spot12r	743.9	662.9	681.5	665.6	56.31	10.45	13.69	18.42
spot13r	730.5	650.6	668.7	655.4	59.3	10.4	14.09	20.61
spot14r	725.5	676.4	687.8	657.8	46.22	10.02	11.6	14.59
spot15u	739.9	675.6	690.5	647.4	30.16	9.35	8.51	9.89
spot16r	664.5	671.2	669.5	685.3	50.5	10.11	12.16	18.32
spot17u	660.6	671.4	668.8	634.4	56.66	10.51	13.42	19.53
spot17r	676.5	684	682	702.9	50.59	10.42	12.38	16.22
spot18r	1500.6	686.8	910.2	1042.3	41.6	10.73	13.87	25.08
spot19r	703.3	661.8	671.2	634.8	47.75	9.94	11.68	15.24
GJ04	630	597.1	603.8	602	35.81	8.29	8.5	36.39
GJ05	641.7	611.6	617.7	595.4	36.38	8.62	8.79	37.69
GJ06	570.1	605.8	597.9	647.8	51.55	8.99	11.14	63.31
spot20c	709.9	654.5	667	601.4	54.39	10.27	13.01	13.8
spot20r	800.3	654.4	688.1	640.1	67.96	11.28	16.43	23.01
spot21r	768.7	654	680.3	595.1	57.98	10.54	14.05	18.25
spot22r	673.1	671.1	671.4	606.5	46.58	10.03	11.41	14.8
spot23r	687.6	670.5	674.3	603.3	50.3	10.26	12.23	15.87
spot24u	683	687.6	686.4	593.1	29.02	9.48	8.2	8.73
spot25r	654.1	681.6	675.2	603.6	42.81	9.96	10.66	13.95
spot26u	722.6	679.5	689.5	622.6	50.07	10.36	12.4	17.58
spot27r	747.8	664.6	683.8	592.7	46.88	9.99	11.7	13.28
spot28r	791.8	662.3	692.4	604.4	51.28	10.2	12.78	14.91
GJ07	639.6	600.3	608.5	597.3	34.17	8.33	8.26	32.8
GJ08	538.6	615.2	599.4	660.9	56.02	9.29	11.89	65.07
GJ09	591	600.3	598.3	601	37.38	8.33	8.62	37.83
spot29r	812.5	634.2	674.7	562.6	71.89	11.22	17.09	20.47
spot30r	829.6	644.5	687.2	583.3	64.95	10.97	15.8	21.07
spot31r	699.7	683.6	687.4	572.9	46.94	10.23	11.71	15.24
spot32r	566.1	634.7	619.9	523.9	79.72	11.28	17.19	19.8
spot33u	710.7	653.5	666.5	562.3	50.28	9.99	12.16	16.03
spot34r	755.2	665.2	686.2	606.9	59.05	10.79	14.39	20.69
GJ10	558.2	599.3	590.7	635	48.96	9.09	10.69	58.01
GJ11	643.7	599.6	608.8	631.5	35.36	8.26	8.42	39.01

Table 5. S09-108 Jebel Tays gabbro age data

11.3 S09-008 Zircon Age

Sample Name: **S09-008** **Halaban Diorite**
GPS Co-Ordinates: **Latitude (N)** **23.477944**
Longitude (E) **44.364389**

Spot	1 Sigma Age (My)				1 Sigma Uncertainty (My)			
	Pb207/Pb206	Pb206/U238	Pb207/U235	Pb208/Th232	Pb207/Pb206	Pb206/U238	Pb207/U235	Pb208/Th232
GJ01	677.9	604	619.8	818.8	28.7	8.36	7.71	19.15
GJ02	608.2	600.2	601.9	634.2	29.12	8.29	7.55	15.85
GJ03	609	601.1	602.7	589.7	29.88	8.32	7.69	15.72
GJ04	614.9	590.9	595.8	651.7	30.51	8.21	7.73	17.42
BJWP1	707.6	732.6	726.4	700	31.88	10.1	9.25	9.34
spot1r	964.3	704.9	770.1	736.2	38.04	9.98	11.26	10.13
spot2r	755.5	683.7	700.6	626.3	42.23	9.74	11.19	9.55
spot3r	689.6	676.6	679.6	605.5	41.62	9.6	10.74	9.63
spot4u	643.4	678.5	670.4	609.8	33.78	9.43	9.03	7.82
spot5u	710.2	645.6	660.1	550	35.7	9.05	9.37	7.62
spot6r	631.9	666	658.3	563.8	45	9.53	11.1	8.33
spot7r	657.2	661	660.1	567.3	44.17	9.45	10.99	8.52
spot8r	779.7	675.7	700.1	614.7	35.9	9.5	9.88	8.5
spot9r	609.4	690.2	671.5	614.4	36.5	9.64	9.52	8.23
spot10u	714.3	679.5	687.6	595.8	32.29	9.43	8.97	7.25
GJ05	608.1	600.6	602.2	599.2	29.09	8.32	7.51	15.11
GJ06	523.2	606.3	589.1	585.4	30.11	8.43	7.46	15.02
GJ07	608.4	600.2	601.9	624.8	28.76	8.31	7.45	15.23
spot11r	694.1	674.8	679.2	594.5	39.54	9.57	10.32	8.77
spot12r	646.2	674.7	668.1	578.2	43.11	9.6	10.84	8.78
spot13r	695.9	647.4	658.2	543.4	49.65	9.47	12.16	9.89
spot14r	713.5	643.6	659.3	552.7	53.77	9.56	13.08	10.23
spot15u	746.3	707.5	716.9	666.6	33.14	9.87	9.48	8.67
spot16r	734.3	666.7	682.3	586.3	50.26	9.8	12.69	10.26
spot17u	741.4	664	681.9	535.9	56.7	9.96	14.09	10.95
spot18r	725	659.1	674.2	548.8	51.47	9.7	12.83	9.11
spot19r	702.2	647.7	659.9	566.7	42.57	9.3	10.77	8.69
spot20u	671.6	684.4	681.4	620.1	33.49	9.56	9.17	7.73
GJ08	608.6	605.7	606.2	614.6	32.85	8.34	8.2	18.69
GJ09	607.4	595.7	598.1	607.9	33.26	8.21	8.19	18.78
spot00821c	651.1	659.8	657.8	594	31.13	10.21	9.31	9.07
spot00821r	638.3	672.8	665	585.5	47.18	9.45	11.58	8.74
spot00822r	677.1	673.8	674.6	581.2	61.56	10.02	14.68	11.88
spot00823r	631.3	658	652.1	575.3	41.94	9.51	10.74	8.72
spot00824r	657.8	672.5	669.2	590.8	39.73	9.27	10.01	8.3
spot00825r	697.2	695.9	696.3	648.9	42.99	9.55	10.89	8.78
spot00826r	718.5	678.4	687.9	663.5	44.79	9.84	11.59	10.83
spot00826c	714.4	687.7	694.1	671.6	41.98	9.55	10.93	10.79
spot00827r	810.4	702.8	728.3	748.7	35.98	9.52	9.76	8.98
BJWP3	653.4	734.2	714.6	724.3	63.59	10.61	16.46	16.63
BJWP4	746.5	730.3	734.4	715.5	32.81	10.03	9.26	10.15
GJ10	576	600.3	595.2	651.1	31.25	9.93	9.2	9.97
GJ11	617.5	606.7	609	583.4	38.5	8.26	9	25.93

Table 6. S09-008 Halaban diorite age data

11.4 S09-046 Zircon Age Data

Sample Name: **S09-046** **Jebel Tays Trondhjemite**
GPS Co-Ordinates: **Latitude (N)** **23.11012**
Longitude (E) **44.96698**

Spot	1 Sigma Age (My)				1 Sigma Uncertainty (My)			
	Pb207/Pb206	Pb206/U238	Pb207/U235	Pb208/Th232	Pb207/Pb206	Pb206/U238	Pb207/U235	Pb208/Th232
GJ01	592.7	562.7	568.3	613.1	42.84	7.81	9.23	48.87
GJ02	635.1	579.1	590.4	810.4	43.63	8.07	9.59	58.92
GJ03	611.1	600.3	602.4	590.7	34.01	7.99	7.97	33.29
GJ04	588.8	602.8	599.7	618.6	36.59	8.13	8.38	36.53
BJWP01	650.5	750	725.4	746.6	34.57	9.91	9.23	15.02
BJWP02	728.4	741.1	737.8	702.1	34.48	9.92	9.45	14.3
GJ05	629.4	596.3	603.2	617.8	40.8	8.23	9.21	44.24
spot1r	790	680.5	706.5	714.3	53.41	10.23	13.27	17.46
spot2r	2454	2533	2489.6	2342.7	19.02	29.18	13.07	31.29
spot3rD	1307.3	658.8	826.1	911.6	33.21	9.22	10.53	17.68
spot4r	820.6	613.8	659.7	575	55.4	9.48	13.12	16.56
spot5r	1079.8	1134.6	1116.1	991.4	21.04	14.24	9.27	15.58
spot6u	1116.1	528.1	654.3	2355.7	26.76	7.17	7.66	50.98
spot7r	709.6	636.5	652.9	568.6	44.27	9.22	10.64	14.45
spot8r	611.8	667.1	654.9	677.2	31.24	8.93	8.07	12.64
spot8c	770.5	696	714.2	640.7	38.42	9.78	10.23	13.95
spot9u	641.4	630.3	633	520.6	39.51	8.95	9.45	9.55
spot10c	1901.6	1852	1875.9	1670	17.98	22.41	11.6	18.61
GJ06	634.2	614.2	618.9	638.2	41.81	8.8	9.73	48.32
GJ07	584	603	598.9	576	48.49	8.83	10.61	50.96
spot11c	2770.2	2839.5	2799.8	2242.6	16.56	32.33	13.02	32.81
spot12r	733	726.5	728.3	635.5	37.34	10.21	10.14	13.02
spot13r	1880.1	1809.7	1843.1	1405.1	19.49	22.37	12.15	22
spot14r	1039.8	674.2	764.6	737	47.36	10.34	13.1	27.26
spot15c	832	739.4	763	642	43.72	10.77	12	14.63
spot16c	730.2	675.1	688	601.8	43.79	9.77	11.06	14.66
spot17r	641.9	641.6	641.6	561.5	50.87	9.58	11.81	18
spot18c	954.4	812.6	851.1	771.3	29.58	10.93	9.73	16.98
spot19c	701	639.9	653.4	539.3	48.3	9.46	11.52	13.93
spot20c	662	664.6	663.9	549	37.89	9.36	9.6	10.65
GJ08	622.5	596.1	601.4	625.9	42.2	8.49	9.64	46.86
GJ09	585.6	606.4	601.6	603.8	41.94	8.58	9.56	44.66
spot21r	752.5	630.6	657.3	559.1	29.87	8.51	8.08	13.03
spot20r	832.5	654.2	695.6	723.1	54.31	10.07	13.47	48.53
spot22r	1028.7	635.6	728.9	585.2	53.12	10.21	14.05	18.44
spot23r	811.1	637.2	676.7	608.3	28.84	8.61	8.13	13.27
spot24r	667.3	631.9	639.6	548.7	29.3	8.56	7.79	10.8
spot25r	828	622.6	668.7	602	33.53	8.65	8.94	13.45
spot26u	806.9	686.8	715.4	625.2	45.65	10.1	11.87	17.25
spot27r	749.9	674.5	692	619	36.65	9.36	9.68	14.22
spot28r	669.5	624.6	634.3	589.2	51.59	9.36	11.89	18.89
spot29r	788.1	677.2	703.2	752.2	34.92	9.23	9.38	30.06
spot29c	637.2	659.3	654.2	596	37.02	9.19	9.24	12.85
spot30r	976.5	683.5	755.7	866.9	37.12	9.55	10.53	33.64
GJ10	594.9	598.1	597.6	624.9	44.97	8.53	9.92	50.84
GJ11	625.7	602.8	607.7	595.3	44.81	8.62	10.13	51.39
spot41r	863.4	646.9	696	738.7	103.17	13.77	24.73	68.09
spot42r	782.4	616.6	653.3	711.4	62.11	9.86	14.46	31.63
spot43r	724.3	620	643	692.5	45.14	8.99	10.76	24.95
spot45r	641	670.3	663.7	718.5	45.76	9.63	11	24.05
spot44r	913.8	606.5	675.8	703.9	62.36	10.25	15.21	38.58
spot46r	756.5	631.8	659.8	665.6	47.26	9.3	11.45	24.68
spot47r	714.6	624.7	644.7	660.4	53.8	9.55	12.54	24.87
spot48r	757.5	628.6	657.5	703.6	38.73	8.83	9.73	23.74
spot49r	1101.1	644.8	756	916.8	59.45	10.89	16	65.16
spot50r	676.9	617.9	630.8	719.5	33.9	8.44	8.45	24.98
GJ14	638.6	586.5	597.3	653.8	45.28	8.4	10.06	56.76
GJ15	717.1	574.1	603.5	431.7	55.2	8.57	12.11	55.92

Table 7. S09-046 Jebel Tays trondhjemite age data

11.5 S09-127 Detrital Zircon Age Data

Sample Name: **S09-127** **Abt Schist Pebbly Conglomerate**
GPS Co-Ordinates: **Latitude (N)** **23.097079**
Longitude (E) **44.976448**

Spot	1 Sigma Age (My)				1 Sigma Uncertainty (My)			
	Pb207/Pb206	Pb206/U238	Pb207/U235	Pb208/Th232	Pb207/Pb206	Pb206/U238	Pb207/U235	Pb208/Th232
GJ01	664.7	579.7	597.2	656.8	27.23	6.86	6.4	24.18
GJ02	579.9	600.1	595.8	616	40.33	7.21	8.53	44.08
GJ03	653.7	594.3	606.8	645	36.54	7.47	8.22	39.6
GJ04	636.5	598.3	605.5	619.3	58.82	8.72	12.54	70.31
GJ05	615.4	605	607.1	609.5	41.18	7.37	8.88	44.89
PLES01	342.4	346.8	346.2	353.6	31.3	4.19	4.45	9.07
GJ06	586.1	599.8	596.8	584.5	39.1	7.83	8.63	40.71
PLES02	307.9	342.4	337.9	355.5	32.6	4.2	4.5	9.69
S09127spot1r	941.9	641.9	712.4	692.2	52.2	8.85	13.13	15.49
S09127spot2r	1867.1	1824	1844	1860.7	20.81	20.05	11.33	24.6
S09127spot3r	5040.7	******	6552.9	******	16.84	107.58	19.57	1267.96
S09127spot4r	964.1	782.9	831.5	796.5	33.86	9.66	9.97	12.18
S09127spot5r	5043.1	******	6803.8	******	28.45	299.88	53.2	1619.54
S09127spot6r	5038.3	******	6322.3	******	24.16	141.71	26.41	1240.57
S09127spot7r	773.2	668.7	693	579.6	34.76	8.43	8.9	9.15
S09127spot8r	2147.6	1897.2	2019.6	2132.6	28.99	22.61	14.94	38.48
S09127spot9r	5121.4	******	6738.3	******	19.68	135.54	24.13	271.12
S09127spot10c	2050.7	1831.4	1936.1	1591.6	38.29	26.16	19.12	24.29
GJ07	627.3	597.4	603.5	597.5	31.36	7.26	7.21	31.13
GJ08	596.2	602.7	601.2	629.8	30.01	7.38	6.98	28.74
S09127spot11r	1802.3	1431.3	1588.2	1051.4	19.59	16.47	10.49	42.01
S09127spot12r	1088.5	670.9	776.4	785.8	125.83	14.58	34.39	54.65
S09127spot13r	1546.7	1147.7	1296.2	1082.3	24.62	13.03	10.42	35.65
S09127spot14r	1962.9	1905.3	1935	1792.1	46.32	26.62	22.37	61.02
S09127spot15r	2117.9	2102.9	2112	1930.9	23.29	23.15	12.87	84.67
S09127spot16r	812.6	713.6	740.2	565.5	182.81	14.84	47.99	43.03
S09127spot17c	679.2	853.3	809.2	736	84.3	12.4	22.2	30.07
S09127spot18r	851.4	739.8	770.3	736.5	57.82	10	15.03	36.45
S09127spot19c	671.5	675.4	678.2	698.1	46.01	8.05	10.69	33.69
S09127spot20r	713.6	735.4	733.8	687.1	44.56	8.53	10.96	28.34
GJ09	612.2	606.8	611.3	563.7	52.06	7.18	11.03	89.65
GJ10	629.9	599.5	609.3	489.2	51.51	7.01	10.89	86.24
S09127spot21r	656.1	632.1	637.4	610.4	93.49	9.4	20.73	60.56
S09127spot22c	651.7	602.2	612.7	633.2	67.13	7.83	14.35	49.97
S09127spot23r	1831.8	2021.4	1929.5	2245.2	43.91	25.65	20.4	258.02
S09127spot24r	917.2	646.3	710.2	531.5	25.75	6.81	6.6	41.58
S09127spot25r	2086	2114.1	2100.2	2158	19.46	20.1	10.39	166.7
S09127spot26r	1223.2	597.5	746	696.1	63.71	8.91	16.78	102.76
S09127spot27r	1795.4	1812.2	1804.5	1831.1	21.18	17.41	10.15	171.59
S09127spot28r	1747.1	837.9	1130.9	1198.6	88.4	14.73	32.69	101.78
S09127spot29c	1909.4	1855.7	1881.2	1929.2	30.55	20.17	14.48	148.54
S09127spot30r	1641.1	594.3	865	773	64.84	9.01	19.93	65.26
S09127spot31r	745.2	697.4	708.9	722.1	56.84	8.62	13.65	65.06
S09127spot32r	1028.4	753.8	826.6	763.8	44.87	9.39	12.43	105.67
GJ11	604.2	591.4	594	713.9	55.35	7.22	11.44	117.26
GJ12	612.3	615.8	615.1	514.2	64.23	7.9	13.59	117.39
GJ13	504.4	611.6	589.2	640.6	40.73	7.36	8.44	57.88
GJ14	656.9	598.5	610.7	621.2	41.13	7.39	9.04	60.63
GJ15	589.6	604.6	601.2	659.7	39.69	7.32	8.56	59.04
GJ16	606.6	599.4	600.9	506	46.57	7.73	9.98	63.16
BJWP01	597.3	703.8	678.6	695.5	78.8	10.08	18.17	29.01
BJWP02	761.9	714.9	726.1	756.7	75	10.34	18.57	31.98
GJ17	613.3	595.9	599.4	585.1	41.16	7.35	8.88	56.45
BJWP03	826.1	699.2	729.8	668.1	70.78	10.04	17.74	29.22
S09127spot33r	896.5	793.7	821.1	714.2	41.23	9.89	11.53	11.59
S09127spot34r	761.2	648.6	674.1	567	39.14	8	9.45	8.44
S09127spot35r	937.5	946.6	943.7	866.3	24.96	10.74	8.31	14.22
S09127spot36u	461.2	713.7	655.8	679.7	132.99	12.19	29.61	29.4
S09127spot37c	929.4	548.2	628.4	462	32.44	6.68	7.81	7.05
S09127spot38r	933.5	727.1	779.5	661.6	29.54	8.6	8.39	9.7
S09127spot39r	867.3	789.3	809.7	717.2	45.26	10.09	12.4	10.44

Table 8. S09-127 Abt schist detrital zircon data

Sample Name: **S09-127** **Abt Schist Pebbly Conglomerate**
GPS Co-Ordinates: **Latitude (N)** **23.097079**
Longitude (E) **44.976448**

Spot	1 Sigma Age (My)				1 Sigma Uncertainty (My)			
	Pb207/Pb206	Pb206/U238	Pb207/U235	Pb208/Th232	Pb207/Pb206	Pb206/U238	Pb207/U235	Pb208/Th232
S09127spot40r	962.3	795.3	840.4	773.8	67.6	11.48	19.03	15.23
S09127spot41r	3630.7	1129.5	2316.3	2956.1	29.23	16.91	16.35	48.93
S09127spot42r	1694.8	724.2	1009.2	856.5	63.63	11.88	21.64	21.19
GJ18	634.6	599.4	606.6	692	39.06	7.34	8.58	58.08
GJ19	566.9	600.9	593.6	507.6	40.01	7.36	8.55	54.2
S09127spot43r	1111	731.6	832.1	1425.7	83.05	11.9	23.67	101.17
S09127spot44r	2097.8	2103.7	2100.8	3346.2	18.78	21.93	10.92	202.16
S09127spot45r	964.9	645.2	720.7	1259	69.43	9.65	17.46	187.9
S09127spot46c	1600.5	678.3	934.5	1512.9	40.35	9.04	13.22	103.71
S09127spot47r	691.9	605.3	623.9	738.3	40.96	7.53	9.24	48.34
S09127spot48r	991.7	825.4	871.8	1313	87.87	13.2	25.48	83.28
S09127spot50r	708.6	685.8	691.1	1072.2	41.45	8.57	10.09	65.34
S09127spot51c	786.3	742.9	753.8	1047.2	65.48	10.56	16.7	64.47
S09127spot52r	1800.1	1861.4	1832.8	2678.5	31.3	22.68	15.09	210.43
GJ20	619.1	610.6	612.4	860.4	38.77	7.54	8.59	92.06
GJ22	591.9	607.1	603.9	759	39.27	7.49	8.57	85.63
S09127spot53c	588.9	632.8	623.4	521	63.24	9.28	13.72	12.32
S09127spot54r	830.8	638.9	682.4	644.1	101.63	10.66	24.47	23.95
S09127spot55r	796.3	696	720	682.7	48.82	9.09	12.22	13.16
S09127spot56r	1355.2	564.1	750.7	453.5	30.22	7.22	8.87	7.49
S09127spot57c	758.1	675.9	694.8	627.1	34.92	8.18	8.74	9.45
S09127spot58c	1004.8	705.6	780.9	784.1	28.64	8.07	8.11	12.86
S09127spot59c	759.4	690	706.1	696.9	58.46	9.38	14.21	17.48
S09127spot60r	2093.7	1007.7	1413.8	1454.6	48.58	16.23	20.56	38.46
S09127spot61c	929	786.9	824.4	767.2	53.86	10.54	14.97	16.61
S09127spot62c	662	695	687.4	563.7	52.35	9.61	12.47	13.16
GJ23	589.5	597.6	595.6	604.3	39.31	7.33	8.48	58.91
GJ24	625.9	595.1	601.1	566.1	38.99	7.32	8.52	57.39
S09127spot63c	1017.7	709.4	787.6	683.8	53.83	10.72	14.67	68.96
S09127spot64c	954.1	803.5	844.5	792.4	63.54	11.99	17.87	49.22
S09127spot65c	814	801.9	805	765.3	62.46	11.24	16.73	39.06
S09127spot66c	1395.8	808.3	982.6	857.9	58.35	12.57	19.05	54.19
S09127spot67c	679	682.2	681.4	652	48.75	8.84	11.54	32.26
S09127spot68c	1803.7	1827.9	1816.4	1637.2	21.78	19.87	11.33	74.13
S09127spot69c	1876	1841.6	1857.6	1706.2	28.87	21.46	14.26	79.4
S09127spot70c	1703.2	1676.1	1688	1494.1	29.85	20.14	14.03	89.63
S09127spot71c	697	760	744.1	660.6	83.86	11.68	20.94	35.17
GJ25	647.2	599.2	609.2	617.6	39.12	7.43	8.67	59.08
GJ26	577.7	601.8	596.7	610.8	39.37	7.43	8.51	55.05
S09127spot73r	935.9	790.4	828.8	714.7	32.07	9.52	9.37	24.03
S09127spot74r	927.4	788.9	825.3	659.6	79.37	12.08	21.96	25.97
S09127spot75c	595.2	652.2	639.2	563.6	107.13	10.61	23.72	26.67
S09127spot76r	870.3	650.1	700.8	561	106.92	11.08	26.52	32.89
S09127spot77c	1727.4	1516.2	1605.9	1439.5	24.13	17.11	11.54	47.34
S09127spot78c	1808.7	1733.1	1766.8	1599.8	21.04	19.71	11.3	73.42
S09127spot79c	867.2	739.1	771.3	705.2	82.78	11.97	21.69	38.5
S09127spot80c	1111.2	791	879.4	745.5	71.91	12.19	21.27	28.53
S09127spot81c	1856.5	1909.3	1883.3	1762.7	19.17	20.26	10.62	59.24
S09127spot82r	927	784.5	822.3	712.8	41.66	10.09	11.76	28
S09127spot83c	1849.9	1891.8	1871.7	1721	26.69	22.13	13.64	76.22
GJ27	616.2	608.5	610	690.6	38.12	7.55	8.49	59.7
GJ28	564.5	609.5	600	713.4	38.93	7.58	8.49	60.33
GJ29	610	613.4	612.5	646.4	29.93	7.33	6.96	39.01
GJ30	653	590.2	603.3	578.7	30.52	7.1	7.03	38.69
GJ31	610.8	588.3	592.8	579.9	30.79	7.08	6.96	38.97
BJWP04	704.4	707.6	706.8	695.1	33.75	8.66	8.64	28.88
S09127spot84r	838.1	606.2	657.7	545.7	27.52	7.33	7.1	13.73
S09127spot85c	2195.8	1890.4	2040.5	2132.4	17.5	20.05	10.62	48.04
S09127spot86r	726.7	734.4	732.5	693.1	28.17	8.81	7.71	15.95
S09127spot87r	653.4	629.8	635.1	565.7	32.35	7.74	7.7	16.39
S09127spot88c	768.7	719.7	731.7	664.6	34.95	9.01	9.23	16.69
S09127spot88r	811.7	639.7	679	605.9	31.22	8.03	8.09	14.85
S09127spot89c	951	876.8	898.2	837.8	39.24	11.34	11.93	24.44
S09127spot90c	725	730.4	729.1	696.5	30.69	8.91	8.24	19.09
S09127spot91r	1034.2	791.5	858	792.5	34	10.11	10.4	19.98
S09127spot91c	840.9	780.9	796.6	748.7	35.2	10.03	10.02	20.13
S09127spot92c	796.6	769.7	776.6	722.4	38.83	9.9	10.58	18.22
S09127spot93c	853.3	783.8	802.1	798.3	22.85	9.26	7.23	25.77
S09127spot93r	901.9	804.8	831	701.6	35.22	11.03	10.56	30.67
GJ32	609.2	602.2	603.6	619.7	33.62	7.49	7.64	41.1

Table 8 cont. S09-127 Abt schist detrital zircon data

11.6 S09-088 Monazite Age Data

Sample Name: **S09-088** **Jebel Tays Trondhjemite**
GPS Co-Ordinates: **Latitude (N)** **23.13745**
Longitude (E) **44.94999**

Spot	1 Sigma Age (My)			1 Sigma Uncertainty (My)		
	Pb207/Pb206	Pb206/U238	Pb207/U235	Pb207/Pb206	Pb206/U238	Pb207/U235
Madel01	507.7	593.4	578	22.94	8.44	6.59
Madel02	1502.9	619.1	849.4	19.12	8.78	8.48
Madel04	486.1	508.7	506.4	23.39	7.28	5.97
Madel05	490	507.7	506.1	23.38	7.26	5.96
Madel06	495.8	524.6	520.7	23.46	7.48	6.1
Madel07	495	515.4	513.2	23.52	7.36	6.04
IS222_01	447.2	446.1	447.4	23.62	6.41	5.49
S09088M1Spot1	2686.6	744.8	1434.8	25.58	11.39	13.85
S09088M1Spot2	835.3	593.9	647.5	47.5	9.2	11.72
S09088M1Spot3	822.7	594.9	645.9	30.6	8.64	8.54
S09088M1Spot4	1973.9	623.8	1008.7	33.9	9.81	13.21
S09088M1Spot5	819.7	616.2	662.6	26.16	8.83	7.93
S09088M1Spot6	893.9	560	631.6	30.74	8.12	8.36
S09088M1Spot7	787	596.6	638.7	30.33	8.57	8.27
S09088M1Spot8	732.2	605.5	633.7	41.58	9.07	10.21
S09088M1Spot9	1791	681.3	1003.4	23.26	9.82	10.41
S09088M1Spot10	724.8	597.2	625.3	48.05	9.15	11.35
Madel08	479.8	511.9	506.9	23.85	7.28	5.98
Madel09	501.8	513.6	512.2	24.43	7.34	6.14
Madel10	482.6	515.8	510.5	25.4	7.43	6.27
S09088M1Spot11	684.1	602.6	620.9	33.89	8.83	8.72
S09088M1Spot12	932.4	620.3	693	38.82	9.26	10.65
S09088M1Spot13	754.6	591.4	627.3	33.34	8.59	8.7
S09088M1Spot14	803	591.8	638.4	51.96	9.25	12.48
S09088M1Spot15	1099.4	597.5	714.7	104.76	12.58	27.14
S09088M1Spot16	0.1	-NaN	2433	7999.9	*******	*******
S09088M1Spot17	3055.5	735.1	1602.4	37.13	13.17	18.68
S09088M1Spot18	2884.5	815.9	1606.2	20.66	11.86	12.97
S09088M1Spot19	2458.2	643.6	1219.6	20.31	9.33	11.21
S09088M1Spot20	1184.1	602.6	741.5	24.55	8.68	8.54
Madel11	485.2	514.4	509.9	23.86	7.31	6.02
Madel12	496	513.6	511.3	23.95	7.31	6.05

Table 9. Jebel Tays trondhjemite monazite age data.

11.7 S08-021 Zircon Age Data

Sample Name: **S08-021** **Cobble Clast**
GPS Co-Ordinates: **Latitude (N)** **23.092965**
Longitude (E) **44.975723**

Spot	1 Sigma Age (My)				1 Sigma Uncertainty (My)			
	Pb207/Pb206	Pb206/U238	Pb207/U235	Pb208/Th232	Pb207/Pb206	Pb206/U238	Pb207/U235	Pb208/Th232
GJ01	611.3	600.5	602.5	607.1	27.59	7.33	6.65	25.88
GJ02	607.4	600.1	601.4	637	27.53	7.34	6.63	25.78
GJ03	560.7	603.7	594.5	585.2	28.05	7.4	6.64	25.88
GJ04	650.8	596.3	607.6	608.3	27.39	7.31	6.7	26.8
GJ05	617.4	603.2	606.1	625	27.88	7.42	6.76	27
PLES01	330	338	336.9	321	29.65	4.24	4.3	7.88
S08021spot1r	817.2	837.4	831.7	930	29.5	10.16	8.92	11.59
S08021spot2r	777.4	704.1	721.7	684.7	27.28	8.73	7.73	8.51
S08021spot3r	1200	678.6	812.5	751.7	47.56	9.26	13.88	15.26
S08021spot4r	745	659.1	678.8	633.2	26.11	8.1	7.13	7.56
S08021spot5r	885.1	611.8	673.2	644	21.47	7.44	6.35	7.1
S08021spot6r	813.7	426.6	492.7	526.8	25.21	5.27	5.49	6.48
S08021spot7r	677.9	661.7	665.3	621.9	32.17	8.32	8.16	8.1
S08021spot8r	681.7	665.3	669	633.3	34.09	8.43	8.58	8.63
S08021spot9r	1358.7	635.7	819.7	690.3	29.3	8.16	9.41	9.58
S08021spot10r	1293.5	686.3	846.4	765.9	26.6	8.66	8.9	9.88
GJ06	600.3	601.8	601.4	616.6	28.95	7.56	6.97	29.31
GJ07	615.1	599.1	602.4	609.1	28.64	7.52	6.94	28.51
S08021spot11r	661.5	669.9	667.9	624.7	40.36	8.75	9.86	10.47
S08021spot12r	794.7	651.3	684.3	631.8	44.61	8.66	11.14	10.93
S08021spot13r	820.3	675.6	709.9	740.3	41.41	8.89	10.74	12.63
S08021spot14r	672	665	666.6	607.5	30.91	8.4	7.96	8.23
S08021spot15r	648.6	642.1	643.5	592.9	29.33	8.08	7.44	7.97
S08021spot16r	6114.4	422.9	2168.5	******	1885.62	*******	*******	*******
S08021spot17r	697	639.1	651.9	608	29.41	8.06	7.57	8.72
S08021spot18r	658.4	623.1	630.8	585.1	21.31	7.66	5.98	7.11
S08021spot19r	1458.7	617	831.7	852.8	33.96	8.55	10.87	15.33
S08021spot20r	926	345	431.8	445.1	21.27	4.36	4.59	5.52
GJ08	605.9	597.1	598.9	616.5	28.96	7.55	6.98	30.17
GJ09	609.7	604	605.2	607.5	28.62	7.62	6.98	29.86

Table 10. Cobble clast zircon age data.

11.8 ICP-MS Data for USGS Cody Shale (SCo-1) Standard

USGS Cody Shale Standard (Sco-1)

All analysis were carried out on a Agilent 7500 series ICP-MS at Adelaide Mircoscopy

Raw Data (ppb)

	Li	Be	Sc	V	Cr	Co	Ni	Se	Ag	Cd	La	Eu	Tl	Pb	Th	U
Cody Shale	10.00	0.47	2.77	30.58	15.09	2.51	6.19	0.30	0.08	0.06	6.68	0.28	0.15	7.63	2.27	0.70
Cody Shale	10.10	0.41	2.76	30.66	14.62	2.43	5.91	0.28	0.06	0.05	6.98	0.26	0.13	7.60	2.07	0.65
Cody Shale	10.32	0.45	2.72	30.82	14.67	2.42	5.94	0.21	0.05	0.06	7.09	0.25	0.13	5.89	2.04	0.65
Cody Shale	10.24	0.46	2.76	31.26	14.65	2.42	5.93	0.28	0.05	0.05	7.12	0.25	0.12	7.51	1.99	0.62
Cody Shale	10.67	0.41	2.71	30.60	15.00	2.43	5.85	0.32	0.07	0.07	6.24	0.26	0.14	7.31	2.17	0.69
Cody Shale	10.89	0.47	2.94	32.82	16.08	2.56	6.35	0.29	0.06	0.06	6.11	0.24	0.14	7.38	1.99	0.67
Cody Shale	10.93	0.49	3.03	33.97	16.50	2.63	6.50	0.31	0.06	0.06	6.12	0.23	0.13	7.26	1.95	0.64
Cody Shale	10.67	0.41	2.71	30.60	15.00	2.43	5.85	0.32	0.07	0.07	6.24	0.26	0.14	7.31	2.17	0.69
Cody Shale	10.89	0.47	2.94	32.82	16.08	2.56	6.35	0.29	0.06	0.06	6.11	0.24	0.14	7.38	1.99	0.67
Cody Shale	10.93	0.49	3.03	33.97	16.50	2.63	6.50	0.31	0.06	0.06	6.12	0.23	0.13	7.26	1.95	0.64

Corrected Data (ppm)

Cody Shale	40.55	1.90	11.24	123.93	61.15	10.17	25.10	1.21	0.33	0.25	27.06	1.14	0.62	30.93	9.19	2.85
Cody Shale	40.93	1.68	11.17	124.28	59.25	9.83	23.95	1.14	0.24	0.22	28.29	1.06	0.53	30.79	8.40	2.63
Cody Shale	41.82	1.81	11.04	124.93	59.47	9.82	24.07	0.85	0.22	0.26	28.75	1.03	0.52	23.87	8.28	2.62
Cody Shale	41.52	1.88	11.18	126.71	59.39	9.83	24.02	1.15	0.21	0.20	28.87	1.02	0.51	30.44	8.07	2.52
Cody Shale	43.25	1.66	10.98	124.04	60.79	9.84	23.70	1.29	0.27	0.27	25.29	1.04	0.57	29.61	8.81	2.79
Cody Shale	44.15	1.89	11.93	133.03	65.18	10.37	25.74	1.19	0.25	0.26	24.77	0.97	0.55	29.92	8.06	2.70
Cody Shale	44.32	1.97	12.30	137.69	66.88	10.64	26.33	1.28	0.25	0.26	24.82	0.93	0.54	29.44	7.90	2.58
Cody Shale	43.25	1.66	10.98	124.04	60.79	9.84	23.70	1.29	0.27	0.27	25.29	1.04	0.57	29.61	8.81	2.79
Cody Shale	44.15	1.89	11.93	133.03	65.18	10.37	25.74	1.19	0.25	0.26	24.77	0.97	0.55	29.92	8.06	2.70
Cody Shale	44.32	1.97	12.30	137.69	66.88	10.64	26.33	1.28	0.25	0.26	24.82	0.93	0.54	29.44	7.90	2.58
Mean	42.82	1.83	11.50	128.94	62.50	10.14	24.87	1.19	0.25	0.25	26.27	1.01	0.55	29.40	8.35	2.68
St Dev	1.48	0.12	0.54	5.80	3.16	0.35	1.09	0.13	0.03	0.02	1.77	0.06	0.03	2.01	0.45	0.11
St Err	0.47	0.04	0.17	1.83	1.00	0.11	0.35	0.04	0.01	0.01	0.56	0.02	0.01	0.64	0.14	0.03

Certified Values (ppm)

Actual	45.00	1.80	11.00	N/A	68.00	11.00	27.00	N/A	N/A	N/A	30.00	N/A	N/A	31.00	9.70	N/A
Error +/-	3.00	0.20	1.00	N/A	5.00	0.80	4.00	N/A	N/A	N/A	1.00	N/A	N/A	3.00	0.50	N/A
% Error	6.67	11.11	9.09	N/A	7.35	7.27	14.81	N/A	N/A	N/A	3.33	N/A	N/A	9.68	5.15	N/A
Diff (ppm)	**-2.18**	**0.03**	**0.50**		**-5.50**	**-0.86**	**-2.13**				**-3.73**			**-1.60**	**-1.35**	
Within Error	Yes	Yes	Yes		Yes	Yes	Yes				No			Yes	No	

N/A = Not Available

Informational not certified

Table 11. Comparison of concentration results from ICP-MS to certified values.

11.9 ICP-MS Data for USGS Basalt Standard (BHVO-1)

USGS Basalt Standard (BHVO-1)

All analysis were carried out on a Agilent 7500 series ICP-MS at Adelaide Mircoscopy

Raw Data (ppb)

	Li	Y	Nb	Cs	La	Pr	Nd	Sm	Eu	Gd	Dy	Ho	Yb	Lu	Th	U
BHVO1-22-1	21.39	89.44	106.03	0.38	73.70	23.64	110.17	27.07	9.13	26.92	22.48	4.19	8.42	1.15	4.04	1.94
BHVO1-22-2	24.69	154.51	104.87	0.51	84.75	25.95	118.52	29.16	10.15	30.40	25.22	4.60	9.34	1.30	6.55	1.83
BHVO1-27-1	22.38	123.59	107.47	0.42	77.95	24.55	113.33	27.51	9.65	28.61	23.85	4.39	8.63	1.20	4.91	1.84
BHVO-27-2	22.43	131.83	103.65	0.44	78.00	23.95	109.94	26.76	9.16	27.83	22.99	4.17	8.35	1.16	5.20	1.74

Corrected Data (ppm)

BHVO1-22-1	4.36	18.21	21.59	0.08	15.00	4.81	22.43	5.51	1.86	5.48	4.58	0.85	1.72	0.24	0.82	0.39
BHVO1-22-2	5.03	31.46	21.35	0.10	17.25	5.28	24.13	5.94	2.07	6.19	5.14	0.94	1.90	0.26	1.33	0.37
BHVO1-27-1	4.63	25.55	22.21	0.09	16.11	5.08	23.43	5.69	1.99	5.91	4.93	0.91	1.78	0.25	1.01	0.38
BHVO-27-2	4.64	27.25	21.42	0.09	16.12	4.95	22.73	5.53	1.89	5.75	4.75	0.86	1.73	0.24	1.08	0.36
Mean	4.66	25.62	21.65	0.09	16.12	5.03	23.18	5.67	1.95	5.83	4.85	0.89	1.78	0.25	1.06	0.38
St Dev	0.28	5.53	0.39	0.01	0.92	0.20	0.76	0.20	0.09	0.30	0.24	0.04	0.09	0.01	0.21	0.01
St Err	0.14	2.76	0.20	0.01	0.46	0.10	0.38	0.10	0.05	0.15	0.12	0.02	0.04	0.01	0.11	0.01

Certified Values (ppm)

Actual	4.60	28.00	19.00	0.13	N/A	N/A	25.00	6.20	2.06	6.40	5.20	0.99	2.00	0.29	1.10	N/A
Error +/-	1.50	2.00	N/A	0.06	N/A	N/A	2.00	0.30	0.08	N/A	0.30	N/A	N/A	N/A	N/A	N/A
% Error	32.61	7.14	N/A	46.15	N/A	N/A	8.00	4.84	3.88	N/A	5.77	N/A	N/A	N/A	N/A	N/A
Diff (ppm)	**0.1**	**-2.4**		**0.0**			**-1.8**	**-0.5**	**-0.1**		**-0.4**					
Within Error	Yes	Yes		Yes			Yes	Yes	Yes		Yes					

N/A = Not Available

Informational not certified

Table 12. Comparison of concentration results from ICP-MS to certified values.

11.10 ICP-MS Data for TASBAS Standard

Tasbas House Standard

All analysis were carried out on a Agilent 7500 series ICP-MS at Adelaide Mircoscopy

Corrected Data (ppm)

	Li	Y	Nb	Cs	La	Nd	Sm	Eu	Dy	Ho	Yb	Lu	Ta	Th	U
Tasbas	11.91	18.75	56.89	0.89	39.95	38.55	6.85	2.19	3.91	0.65	1.08	0.15	3.06	3.49	1.43
Tasbas	10.70	19.29	59.41	0.88	40.18	39.22	6.74	2.15	3.77	0.63	1.05	0.14	3.04	3.25	1.32
Tasbas	10.36	22.84	63.37	0.88	43.62	41.79	7.40	2.36	4.17	0.69	1.17	0.16	3.29	3.79	1.41
Tasbas	11.75	18.14	56.56	0.89	39.33	38.12	6.70	2.14	3.80	0.64	1.05	0.14	3.00	3.34	1.39
Tasbas	11.32	16.42	58.94	0.87	41.20	35.02	7.07	2.28	4.11	0.68	1.14	0.16	3.42	4.12	1.79
Tasbas	10.77	15.87	56.36	0.86	39.64	33.57	6.81	2.18	3.87	0.64	1.09	0.15	3.34	3.97	1.67
Tasbas	11.46	16.56	59.58	0.88	41.59	35.38	7.13	2.31	4.17	0.69	1.16	0.16	3.44	4.15	1.82
Mean	11.18	18.27	58.73	0.88	40.79	37.38	6.96	2.23	3.97	0.66	1.10	0.15	3.23	3.73	1.55
St Dev	0.54	2.21	2.28	0.01	1.38	2.64	0.23	0.08	0.16	0.03	0.05	0.01	0.18	0.34	0.19
St Error	0.22	0.90	0.93	0.00	0.56	1.08	0.10	0.03	0.07	0.01	0.02	0.00	0.07	0.14	0.08

Accpeted Values (ppm) (NOT CERTIFIED)

Actual	12.5		1.07	44.48	40.2	8.25	2.64	4.77	0.8	1.27	0.17	3.76	4.87	1.89
Error +/-	N/A		N/A	N/A	N/A	N/A	N/A	N/A	N/A	N/A	N/A	N/A	N/A	N/A
% Error	N/A		N/A	N/A	N/A	N/A	N/A	N/A	N/A	N/A	N/A	N/A	N/A	N/A
Diff	-1.32		-0.19	-3.69	-2.82	-1.29	-0.41	-0.80	-0.14	-0.17	-0.02	-0.53	-1.14	-0.34

Table 13. Comparison of concentration results from ICP-MS to suggested values for the TASBAS house standard.

11.11 XRF Major Element Data

Major Elemet Data

Sample Name	Description	Latitude (N)	Longitude (E)	SiO_2 % XRF	Al_2O_3 % XRF	Fe_2O_3T % XRF	MnO % XRF	MgO % XRF	CaO % XRF	Na_2O % XRF	K_2O % XRF	TiO_2 % XRF	P_2O_5 % XRF	SO_3 % XRF	LOI %	Total %	Mg#
S09-061	Mafic Dike	23.108920	44.961550	53.183	15.13	11.97	0.23	3.89	7.44	2.89	0.19	0.92	0.71	0.02	2.84	99.40	0.56
S09-081	Mafic Dike	23.131080	44.988140	61.99	14.73	6.16	0.08	3.16	3.37	4.29	2.20	0.73	0.20	0.02	1.85	98.80	0.67
S09-111	Mafic Dike	23.070510	44.990140	51.433	13.57	8.23	0.15	7.12	12.62	2.79	0.06	0.56	0.12	0.02	3.49	100.17	0.77
S09-112	Mafic Dike	23.064600	44.993250	56.908	15.56	6.24	0.09	5.12	5.69	4.17	0.74	0.94	0.15	0.03	4.06	99.71	0.76
S09-125	Mafic Dike	23.118130	45.025320	48.072	14.94	9.34	0.16	9.79	12.82	2.48	0.04	0.59	0.07	0.01	1.68	99.98	0.81
S09-140	Mafic Dike	23.522370	44.226990	62.89	16.69	4.61	0.09	2.02	4.70	4.56	1.93	0.46	0.22	0.00	1.43	99.60	0.63
S09-067	Carbonate	23.105580	44.963170	37.76	12.90	10.62	0.13	13.41	6.52	0.44	1.09	0.57	0.13	0.04	15.15	98.76	0.83
S09-071	Carbonate			24.86	0.14	5.84	0.10	30.31	0.19	0.11	0.02	0.01	0.00	0.05	36.02	97.66	0.95
S09-062	Carbonate + Pyrite	23.107680	44.961750	49.209	17.10	14.20	0.24	1.06	4.00	0.26	5.53	1.06	0.87	0.10	6.01	99.63	0.23
S09-063	Carbonate + Pyrite	23.107050	44.962320	47.277	15.95	9.54	0.15	5.24	5.38	0.25	4.38	0.47	0.03	0.09	10.77	99.53	0.69
S09-023	Mafic Cumulate	23.102680	44.963620	38.70	17.83	7.08	0.15	5.60	21.78	0.18	0.02	0.40	0.06	0.06	8.57	100.44	0.76
S09-095	Mafic Cumulate	23.133230	45.004460	36.247	24.34	10.71	0.23	5.83	16.91	0.36	0.63	1.16	0.36	0.03	3.33	100.14	0.68
S09-083	Dacite	23.133230	45.004460	63.692	17.05	4.02	0.07	1.19	4.97	5.43	1.35	0.51	0.27	0.02	1.49	100.06	0.54
S09-021	Felsic Dike	23.101530	46.968333	74.85	15.31	1.00	0.01	0.61	0.16	0.17	4.68	0.12	0.01	0.02	2.42	99.35	0.71
S09-085	Felsic Dike	23.124190	44.977960	72.13	14.55	0.65	0.04	0.14	1.33	4.74	3.67	0.03	0.03	0.00	0.99	98.29	0.45
S09-124	Felsic Dike	23.027000	44.977680	74.184	12.52	1.30	0.04	0.49	3.75	4.91	0.45	0.15	0.05	0.01	1.38	99.25	0.60
S09-007	Mafic Intrusive	23.477944	44.364389	53.99	18.15	7.62	0.12	4.40	8.49	3.22	0.64	0.68	0.22	0.00	2.08	99.62	0.70
S09-008	Mafic Intrusive	23.477944	44.364389	53.80	18.14	7.64	0.13	4.40	8.48	3.25	0.66	0.69	0.23	0.00	2.09	99.51	0.70
S09-104	Mafic Intrusive			52.969	16.89	8.35	0.16	4.28	7.02	3.84	2.51	0.81	0.50	0.02	1.54	98.89	0.67
S09-108	Mafic Intrusive			48.331	14.13	6.88	0.13	10.28	14.03	2.16	0.03	0.30	0.04	0.01	2.90	99.22	0.86
S09-110	Mafic Intrusive	23.036210	44.934290	51.292	18.74	8.43	0.15	5.01	8.83	3.86	0.63	0.73	0.23	0.00	1.81	99.70	0.70
S09-115	Mafic Intrusive	23.052860	44.984390	49.027	19.21	9.05	0.16	5.27	11.84	3.30	0.39	0.75	0.06	0.01	1.06	100.12	0.70
S09-117B	Mafic Intrusive	23.052860	44.984390	50.064	15.95	7.36	0.14	8.85	13.30	2.02	0.03	0.39	0.04	0.01	2.15	100.30	0.83
S09-134	Mafic Intrusive	23.116090	45.025280	74.147	13.15	1.50	0.03	0.36	0.89	3.53	4.67	0.17	0.04	0.00	0.72	99.20	0.49
S09-135	Mafic Intrusive	23.539840	44.278100	73.51	13.12	1.50	0.03	0.36	0.88	3.50	4.65	0.16	0.04	0.00	0.79	98.55	0.49
S09-137	Mafic Intrusive	23.507320	44.185810	51.48	18.64	8.05	0.13	4.83	8.92	3.56	0.76	0.64	0.23	0.00	2.05	99.29	0.70
S09-121	Conglomerate Clast	23.095020	44.977880	73.59	12.49	1.35	0.05	0.49	3.72	4.91	0.45	0.15	0.05	0.01	1.44	98.71	0.59
S09-026	Serpentinised Peridotite	23.101290	44.978030	38.29	0.84	9.34	0.15	35.93	0.09	0.13	0.00	0.02	0.00	0.04	11.37	96.21	0.94
S09-038	Serpentinised Peridotite	23.103020	44.967670	31.58	0.16	8.83	0.10	36.82	0.35	0.13	0.00	0.01	0.00	0.15	18.96	97.06	0.94
S09-090	Serpentinised Ultramafic Cumulate	23.098020	44.973620	40.33	4.74	9.84	0.13	29.64	4.84	0.18	0.00	0.06	0.01	0.02	8.90	98.69	0.92
S09-036	Trondhjemite	23.105080	44.967630	56.09	15.43	4.67	0.07	2.56	6.77	4.03	1.94	0.95	0.24	0.02	6.73	99.49	0.68
S09-037	Trondhjemite	23.104070	44.966700	69.08	15.53	1.82	0.03	0.86	3.00	5.67	0.76	0.26	0.09	0.00	1.83	98.94	0.65
S09-039	Trondhjemite	23.103020	44.967670	69.37	15.55	1.28	0.03	0.64	2.90	5.56	1.24	0.19	0.07	0.00	0.97	97.79	0.67
S09-045	Trondhjemite	23.108970	44.966580	63.74	16.74	3.52	0.04	1.87	4.41	4.75	1.36	0.68	0.15	0.02	2.04	99.31	0.68
S09-046	Trondhjemite	23.110120	44.966980	67.55	15.73	2.04	0.03	0.99	2.84	4.37	2.44	0.33	0.11	0.04	2.68	99.15	0.66
S09-048	Trondhjemite	23.111140	44.969250	63.825	16.65	3.44	0.04	1.83	4.50	4.28	1.44	0.67	0.15	0.02	2.43	99.27	0.68
S09-068	Trondhjemite	23.105380	44.963540	64.85	16.33	2.39	0.04	1.30	2.45	4.86	2.41	0.37	0.12	0.03	3.94	99.08	0.68
S09-074	Trondhjemite	23.102000	44.947220	68.70	14.60	1.59	0.02	0.42	2.80	4.18	2.61	0.24	0.07	0.10	3.31	98.64	0.51
S09-084	Trondhjemite	23.123910	44.977600	68.01	15.52	1.74	0.03	0.91	3.31	5.50	1.21	0.26	0.09	0.01	1.90	98.48	0.67
S09-088	Trondhjemite	23.137450	44.949990	68.41	14.91	1.25	0.02	0.55	2.07	4.94	1.91	0.17	0.05	0.00	2.45	96.74	0.63
S09-099	Trondhjemite	23.112100	44.949730	68.929	14.91	1.83	0.03	0.49	2.69	4.27	2.58	0.26	0.08	0.10	3.16	99.31	0.52

Table 14. Major element XRF analysis

11.12 ICP-MS Trace Element Data

Trace Element Data (ppm)

Sample Name	Description	Latitude (N)	Longitude (E)	Cs	Tl	Rb	Ba	Th	U	K	Ta
				ICP-MS	ICP-MS	ICP-MS	XRF	ICP-MS	ICP-MS	XRF	ICP-MS
S09-061	Mafic Dike	23.108920	44.961550	0.19	0.02	5.76	48.00	0.77	0.19	1552.38	0.18
S09-081	Mafic Dike	23.131080	44.988140	3.22	0.24	62.24	598.00	3.66	0.99	18288.16	0.40
S09-111	Mafic Dike	23.070510	44.990140	1.03	0.08	18.94	338.00	0.62	0.27	506.39	0.26
S09-112	Mafic Dike	23.064600	44.993250	0.27	0.03	7.12	191.00	0.03	0.02	6143.09	0.21
S09-125	Mafic Dike	23.118130	45.025320	0.48	0.07	19.63	526.00	1.35	0.57	323.76	0.31
S09-140	Mafic Dike	23.522370	44.226990	1.25	0.18	45.36	2155.00	4.58	1.35	16005.25	0.31
S09-067	Carbonate	23.105580	44.963170	1.22	0.22	70.27	62.00	0.77	0.20	9015.40	0.13
S09-071	Carbonate			0.05	0.01	0.98	4.00	0.00	0.01	157.73	0.09
S09-062	Carbonate + Pyrite	23.107680	44.961750	3.37	0.73	248.78	276.00	0.94	0.70	45898.87	0.17
S09-063	Carbonate + Pyrite	23.107050	44.962320	1.41	0.38	168.49	125.00	0.13	0.13	36360.47	0.12
S09-023	Mafic Cumulate	23.102680	44.963620	0.07	0.00	0.60	19.00	0.01	0.02	182.63	0.09
S09-095	Mafic Cumulate	23.133230	45.004460	0.96	0.07	14.57	246.00	5.39	2.12	5196.73	0.61
S09-083	Dacite	23.133230	45.004460	2.14	0.10	33.24	375.00	1.93	0.64	11190.39	0.75
S09-021	Felsic Dike	23.101530	46.968333	1.95	0.47	141.86	1096.00	1.58	0.96	38884.12	0.09
S09-085	Felsic Dike	23.124190	44.977960	0.46	0.20	52.82	747.00	1.87	1.35	30474.72	1.18
S09-124	Felsic Dike	23.027000	44.977680	0.03	0.00	0.57	49.00	0.02	0.03	3768.87	0.17
S09-007	Mafic Intrusive	23.477944	44.364389	0.38	0.02	4.60	310.00	0.17	0.06	5346.15	0.18
S09-104	Mafic Intrusive			0.01	0.00	0.33	13.00	0.05	0.02	20795.20	0.11
S09-108	Mafic Intrusive			0.16	0.01	3.34	356.00	0.24	0.09	273.95	0.22
S09-110	Mafic Intrusive	23.036210	44.934290	0.01	0.00	0.76	28.00	0.05	0.07	5205.03	0.13
S09-115	Mafic Intrusive	23.052860	44.984390	0.02	0.00	0.28	11.00	0.01	0.04	3262.48	0.17
S09-117B	Mafic Intrusive	23.052860	44.984390	0.02	0.00	0.47	15.00	0.01	0.00	207.54	0.09
S09-134	Mafic Intrusive	23.116090	45.025280	0.30	0.03	6.78	430.00	0.16	0.06	38801.11	0.16
S09-135	Mafic Intrusive	23.539840	44.278100	0.81	0.15	35.22	992.00	1.54	0.58	38618.47	0.24
S09-137	Mafic Intrusive	23.507320	44.185810	0.50	0.14	35.36	893.00	3.35	1.05	6325.73	0.48
S09-121	Conglomerate Clast	23.095020	44.977880	0.41	0.03	10.80	165.00	7.47	1.52	3727.36	0.48
S09-026	Serpentinised Peridotite	23.101290	44.978030	0.00	0.00	0.03	0.00	0.00	0.00	8.30	0.03
S09-038	Serpentinised Peridotite	23.103020	44.967670	0.02	0.00	0.02	5.00	0.00	0.01	0.00	0.01
S09-090	Serpentinised Ultramafic Cumulate	23.098020	44.973620	0.07	0.01	0.06	64.00	0.00	0.03	16.60	0.08
S09-036	Granitoid	23.105080	44.967630	1.49	0.13	34.68	544.00	1.50	0.57	16079.96	0.65
S09-037	Granitoid	23.104070	44.966700	0.73	0.07	14.17	554.00	0.50	0.43	6292.52	0.43
S09-039	Granitoid	23.103020	44.967670	0.83	0.09	17.02	572.00	0.48	0.51	10285.53	0.17
S09-045	Granitoid	23.108970	44.966580	0.92	0.12	25.00	490.00	1.16	0.52	11306.61	0.22
S09-046	Granitoid	23.110120	44.966980	1.22	0.14	47.85	830.00	0.72	0.35	20272.21	0.23
S09-048	Granitoid	23.111140	44.969250	0.93	0.10	23.47	582.00	0.65	0.30	11987.33	0.27
S09-068	Granitoid	23.105380	44.963540	1.66	0.29	79.79	485.00	1.62	0.80	20039.77	0.16
S09-074	Granitoid	23.102000	44.947220	0.88	0.21	88.22	774.00	4.37	1.56	21650.25	0.26
S09-084	Granitoid	23.123910	44.977600	0.66	0.09	19.21	634.00	0.63	0.64	10061.39	0.31
S09-088	Granitoid	23.137450	44.949990	1.20	0.25	81.98	910.00	1.80	1.01	15872.43	0.24
S09-099	Granitoid	23.112100	44.949730	0.79	0.21	64.26	689.00	4.12	1.62	21384.61	0.42

Table 15. Solution ICP-MS trace element analysis

Sample Name	Description	Latitude (N)	Longitude (E)	Nb	La	Ce	Pb	Pr	Mo	Sr	Nd
				ICP-MS	ICP-MS	ICP-MS	ICP-MS	ICP-MS	ICP-MS	XRF	ICP-MS
S09-061	Mafic Dike	23.108920	44.961550	1.78	7.99	20.20	2.14	2.55	0.74	552.00	12.19
S09-081	Mafic Dike	23.131080	44.988140	5.23	16.09	34.64	8.15	4.08	0.73	416.40	16.64
S09-111	Mafic Dike	23.070510	44.990140	3.31	6.63	15.68	5.12	1.92	0.19	479.60	8.45
S09-112	Mafic Dike	23.064600	44.993250	0.62	0.65	2.10	0.94	0.43	0.26	97.40	2.81
S09-125	Mafic Dike	23.118130	45.025320	2.96	8.35	18.48	8.62	2.26	0.25	820.80	10.03
S09-140	Mafic Dike	23.522370	44.226990	3.90	33.26	68.13	6.77	8.88	0.33	1165.80	31.74
S09-067	Carbonate	23.105580	44.963170	1.42	4.73	12.28	1.16	1.50	0.23	101.80	6.95
S09-071	Carbonate			0.04	0.06	0.13	2.98	0.01	0.76	15.20	0.05
S09-062	Carbonate + Pyrite	23.107680	44.961750	4.98	10.02	24.77	8.05	3.30	230.09	95.40	16.02
S09-063	Carbonate + Pyrite	23.107050	44.962320	0.65	0.99	2.51	3.45	0.36	0.40	42.70	1.81
S09-023	Mafic Cumulate	23.102680	44.963620	0.27	0.43	1.17	0.58	0.22	0.13	228.70	1.19
S09-095	Mafic Cumulate	23.133230	45.004460	8.27	28.33	60.07	13.00	7.87	0.90	363.40	29.16
S09-083	Dacite	23.133230	45.004460	10.36	17.37	32.98	13.97	3.89	0.30	748.30	15.26
S09-021	Felsic Dike	23.101530	46.968333	0.61	5.77	13.24	8.85	1.41	0.04	45.30	5.21
S09-085	Felsic Dike	23.124190	44.977960	7.96	4.51	11.39	14.59	1.19	0.30	231.80	4.80
S09-124	Felsic Dike	23.027000	44.977680	0.27	0.61	2.14	0.29	0.42	0.18	65.80	2.53
S09-007	Mafic Intrusive	23.477944	44.364389	1.27	6.78	16.15	4.56	1.96	0.20	1231.10	8.49
S09-104	Mafic Intrusive			0.54	0.82	2.02	0.67	0.31	0.13	232.30	1.61
S09-108	Mafic Intrusive			1.18	5.89	14.78	3.21	1.85	0.22	1055.50	8.35
S09-110	Mafic Intrusive	23.036210	44.934290	0.41	0.80	2.80	0.48	0.49	0.09	29.30	2.80
S09-115	Mafic Intrusive	23.052860	44.984390	0.20	0.29	1.15	0.19	0.23	0.09	60.50	1.57
S09-117B	Mafic Intrusive	23.052860	44.984390	0.17	0.27	0.98	0.12	0.20	0.09	66.80	1.26
S09-134	Mafic Intrusive	23.116090	45.025280	1.69	5.91	13.76	3.20	1.68	0.27	976.20	7.50
S09-135	Mafic Intrusive	23.539840	44.278100	2.64	15.83	33.08	6.29	4.01	0.07	1178.80	16.95
S09-137	Mafic Intrusive	23.507320	44.185810	3.66	16.40	31.71	6.72	3.54	0.37	1090.00	13.49
S09-121	Conglomerate Clast	23.095020	44.977880	3.57	14.82	31.67	8.20	3.14	0.46	146.10	10.92
S09-026	Serpentinised Peridotite	23.101290	44.978030	0.01	0.05	0.08	0.32	0.01	0.17	5.40	0.05
S09-038	Serpentinised Peridotite	23.103020	44.967670	0.03	0.00	0.01	1.15	0.00	0.09	33.20	0.00
S09-090	Serpentinised Ultramafic Cumulate	23.098020	44.973620	0.05	0.03	0.09	0.12	0.02	0.09	22.80	0.14
S09-036	Granitoid	23.105080	44.967630	7.86	11.46	24.66	6.11	2.83	0.41	642.00	11.53
S09-037	Granitoid	23.104070	44.966700	1.81	3.41	8.50	7.58	1.00	0.39	826.10	4.30
S09-039	Granitoid	23.103020	44.967670	1.18	2.13	4.80	8.64	0.65	0.02	813.20	2.74
S09-045	Granitoid	23.108970	44.966580	2.57	7.95	20.43	7.15	2.51	0.06	944.10	10.71
S09-046	Granitoid	23.110120	44.966980	2.91	6.24	14.46	6.92	1.62	0.23	503.70	6.61
S09-048	Granitoid	23.111140	44.969250	2.35	6.41	15.84	5.08	1.93	0.18	781.80	8.23
S09-068	Granitoid	23.105380	44.963540	1.19	6.25	15.34	4.89	1.82	0.05	361.60	7.60
S09-074	Granitoid	23.102000	44.947220	3.06	13.47	24.84	11.35	2.58	0.12	187.40	9.11
S09-084	Granitoid	23.123910	44.977600	2.00	3.41	8.66	9.11	1.00	0.12	784.60	4.24
S09-088	Granitoid	23.137450	44.949990	1.43	4.67	11.26	13.74	1.15	0.04	481.20	4.42
S09-099	Granitoid	23.112100	44.949730	2.12	9.80	18.71	10.44	1.89	0.36	189.00	6.77

Table 15 cont. Solution ICP-MS trace element analysis

Sample Name	Description	Latitude (N)	Longitude (E)	P	Sm	Zr	Eu	Ti	Gd	Tb	Dy
				XRF	ICP-MS	XRF	ICP-MS	ICP-MS	ICP-MS	ICP-MS	ICP-MS
S09-061	Mafic Dike	23.108920	44.961550	3983.50	3.02	50.50	0.91	5489.84	3.14	0.43	2.53
S09-081	Mafic Dike	23.131080	44.988140	1132.51	3.76	134.90	1.00	4375.09	3.85	0.59	3.57
S09-111	Mafic Dike	23.070510	44.990140	659.22	2.11	80.60	0.77	3380.21	2.30	0.35	2.17
S09-112	Mafic Dike	23.064600	44.993250	862.06	1.36	26.50	0.65	5657.66	2.18	0.40	2.74
S09-125	Mafic Dike	23.118130	45.025320	371.87	2.52	83.70	0.88	3530.04	2.59	0.36	2.10
S09-140	Mafic Dike	23.522370	44.226990	1262.10	6.22	90.30	2.02	2774.89	5.24	0.64	3.20
S09-067	Carbonate	23.105580	44.963170	726.83	1.91	44.60	0.55	3434.15	2.24	0.37	2.32
S09-071	Carbonate			16.90	0.01	6.40	0.00	41.95	0.01	0.00	0.01
S09-062	Carbonate + Pyrite	23.107680	44.961750	4879.37	4.05	57.30	1.20	6376.85	4.26	0.58	3.43
S09-063	Carbonate + Pyrite	23.107050	44.962320	174.67	0.64	23.30	0.20	2834.82	0.93	0.17	1.21
S09-023	Mafic Cumulate	23.102680	44.963620	326.79	0.48	9.20	0.25	2397.31	0.72	0.14	0.96
S09-095	Mafic Cumulate	23.133230	45.004460	2034.01	6.48	239.80	1.69	6958.20	6.38	0.95	5.70
S09-083	Dacite	23.133230	45.004460	1543.82	3.06	155.90	0.97	3050.58	2.84	0.39	2.12
S09-021	Felsic Dike	23.101530	46.968333	50.71	0.96	72.40	0.35	695.22	0.72	0.08	0.38
S09-085	Felsic Dike	23.124190	44.977960	163.40	1.51	41.40	0.52	161.82	1.62	0.25	1.35
S09-124	Felsic Dike	23.027000	44.977680	287.35	1.11	29.30	0.45	922.96	1.72	0.33	2.29
S09-007	Mafic Intrusive	23.477944	44.364389	1262.10	1.97	35.60	0.73	4075.43	1.97	0.28	1.66
S09-104	Mafic Intrusive			2789.02	0.59	16.40	0.32	4848.56	0.89	0.17	1.17
S09-108	Mafic Intrusive			236.64	1.96	22.60	0.76	1780.00	1.99	0.29	1.73
S09-110	Mafic Intrusive	23.036210	44.934290	1301.54	1.11	26.60	0.44	4387.08	1.71	0.31	2.15
S09-115	Mafic Intrusive	23.052860	44.984390	326.79	0.72	15.10	0.39	4494.96	1.22	0.23	1.63
S09-117B	Mafic Intrusive	23.052860	44.984390	225.37	0.60	13.40	0.29	2331.39	0.96	0.18	1.34
S09-134	Mafic Intrusive	23.116090	45.025280	236.64	7.50	17.90	0.74	988.89	1.83	0.26	1.55
S09-135	Mafic Intrusive	23.539840	44.278100	231.01	3.53	53.30	1.23	940.94	2.99	0.37	1.95
S09-137	Mafic Intrusive	23.507320	44.185810	1279.00	13.49	95.10	0.82	3841.69	2.18	0.29	1.62
S09-121	Conglomerate Clast	23.095020	44.977880	287.35	2.14	75.80	0.38	881.01	1.88	0.27	1.57
S09-026	Serpentinised Peridotite	23.101290	44.978030	0.00	0.02	5.00	0.01	143.84	0.04	0.01	0.06
S09-038	Serpentinised Peridotite	23.103020	44.967670	-5.63	0.00	3.50	0.00	41.95	0.00	0.00	0.00
S09-090	Serpentinised Ultramafic Cumulate	23.098020	44.973620	56.34	0.14	2.90	0.05	341.62	0.17	0.03	0.24
S09-036	Granitoid	23.105080	44.967630	1357.88	2.55	123.00	0.89	5663.65	2.53	0.35	2.08
S09-037	Granitoid	23.104070	44.966700	495.82	1.03	74.20	0.39	1558.25	1.03	0.15	0.82
S09-039	Granitoid	23.103020	44.967670	411.31	0.68	60.90	0.28	1120.74	0.69	0.10	0.50
S09-045	Granitoid	23.108970	44.966580	816.98	2.32	86.80	0.83	4069.44	2.05	0.26	1.34
S09-046	Granitoid	23.110120	44.966980	642.32	1.43	92.90	0.54	1995.76	1.31	0.16	0.79
S09-048	Granitoid	23.111140	44.969250	822.62	1.78	81.40	0.63	3985.53	1.51	0.18	0.93
S09-068	Granitoid	23.105380	44.963540	664.86	1.57	73.00	0.54	2187.55	1.36	0.17	0.94
S09-074	Granitoid	23.102000	44.947220	405.67	1.57	119.20	0.46	1432.39	1.29	0.15	0.73
S09-084	Granitoid	23.123910	44.977600	478.92	1.04	69.30	0.40	1552.26	1.06	0.15	0.82
S09-088	Granitoid	23.137450	44.949990	287.35	0.91	96.70	0.44	1036.84	0.81	0.11	0.55
S09-099	Granitoid	23.112100	44.949730	422.58	1.21	114.30	0.36	1546.27	1.02	0.13	0.63

Table 15 cont. Solution ICP-MS trace element analysis

Sample Name	Description	Latitude (N)	Longitude (E)	Ho	Er	Y	Yb	Lu	Cr	Ni	Co
				ICP-MS	ICP-MS	ICP-MS	ICP-MS	ICP-MS	XRF	XRF	XRF
S09-061	Mafic Dike	23.108920	44.961550	0.52	1.45	14.09	1.29	0.19	21	33	47
S09-081	Mafic Dike	23.131080	44.988140	0.74	2.18	21.59	2.10	0.32	165	58	41
S09-111	Mafic Dike	23.070510	44.990140	0.44	1.25	12.70	1.02	0.15	150	85	38
S09-112	Mafic Dike	23.064600	44.993250	0.59	1.72	15.75	1.58	0.22	590	222	56
S09-125	Mafic Dike	23.118130	45.025320	0.40	1.10	10.86	0.92	0.13	23	17	30
S09-140	Mafic Dike	23.522370	44.226990	0.60	1.65	15.51	1.51	0.23	24	11	36
S09-067	Carbonate	23.105580	44.963170	0.49	1.48	12.81	1.43	0.22	227	59	35
S09-071	Carbonate			0.00	0.01	0.07	0.01	0.00	2031	1775	103
S09-062	Carbonate + Pyrite	23.107680	44.961750	0.69	1.93	20.20	1.66	0.24	20	33	42
S09-063	Carbonate + Pyrite	23.107050	44.962320	0.28	0.84	7.73	0.81	0.12	42	26	38
S09-023	Mafic Cumulate	23.102680	44.963620	0.21	0.66	6.18	0.63	0.09	139	51	34
S09-095	Mafic Cumulate	23.133230	45.004460	1.18	3.46	38.70	3.31	0.48	177	76	40
S09-083	Dacite	23.133230	45.004460	0.41	1.14	12.91	1.01	0.15	2	3	29
S09-021	Felsic Dike	23.101530	46.968333	0.07	0.20	1.99	0.19	0.03	2	1	11
S09-085	Felsic Dike	23.124190	44.977960	0.23	0.61	6.60	0.52	0.07	1	0	68
S09-124	Felsic Dike	23.027000	44.977680	0.52	1.56	14.82	1.51	0.22	591	191	63
S09-007	Mafic Intrusive	23.477944	44.364389	0.34	0.98	8.73	0.91	0.14	47	26	43
S09-104	Mafic Intrusive			0.25	0.75	7.40	0.70	0.10	624	141	55
S09-108	Mafic Intrusive			0.35	1.01	9.56	0.94	0.14	40	25	48
S09-110	Mafic Intrusive	23.036210	44.934290	0.48	1.44	14.65	1.40	0.20	358	94	44
S09-115	Mafic Intrusive	23.052860	44.984390	0.37	1.11	10.16	1.08	0.16	496	129	45
S09-117B	Mafic Intrusive	23.052860	44.984390	0.30	0.89	8.60	0.87	0.12	413	137	50
S09-134	Mafic Intrusive	23.116090	45.025280	0.32	0.92	8.36	0.85	0.12	45	28	32
S09-135	Mafic Intrusive	23.539840	44.278100	0.37	1.01	9.53	0.91	0.13	35	22	40
S09-137	Mafic Intrusive	23.507320	44.185810	0.32	0.93	8.78	0.93	0.14	15	7	30
S09-121	Conglomerate Clast	23.095020	44.977880	0.32	0.99	10.68	1.06	0.16	23	8	61
S09-026	Serpentinised Peridotite	23.101290	44.978030	0.01	0.04	0.35	0.05	0.01	4832	3381	108
S09-038	Serpentinised Peridotite	23.103020	44.967670	0.00	0.00	0.03	0.01	0.00	2717	2435	105
S09-090	Serpentinised Ultramafic Cumulate	23.098020	44.973620	0.05	0.17	1.30	0.15	0.02	1536	616	126
S09-036	Granitoid	23.105080	44.967630	0.41	1.14	11.72	0.99	0.14	29	16	36
S09-037	Granitoid	23.104070	44.966700	0.16	0.44	4.36	0.40	0.06	19	8	41
S09-039	Granitoid	23.103020	44.967670	0.09	0.23	2.41	0.22	0.03	13	3	57
S09-045	Granitoid	23.108970	44.966580	0.23	0.58	5.85	0.46	0.07	12	13	31
S09-046	Granitoid	23.110120	44.966980	0.14	0.36	4.17	0.29	0.04	10	5	18
S09-048	Granitoid	23.111140	44.969250	0.16	0.42	4.77	0.31	0.04	15	13	28
S09-068	Granitoid	23.105380	44.963540	0.17	0.47	4.53	0.42	0.06	7	4	29
S09-074	Granitoid	23.102000	44.947220	0.13	0.36	4.04	0.31	0.04	6	2	20
S09-084	Granitoid	23.123910	44.977600	0.15	0.44	4.09	0.41	0.06	14	7	41
S09-088	Granitoid	23.137450	44.949990	0.10	0.27	2.65	0.23	0.04	3	2	68
S09-099	Granitoid	23.112100	44.949730	0.11	0.30	2.90	0.25	0.04	9	4	46

Table 15 cont. Solution ICP-MS trace element analysis

11.13 CIPW Normative Compositions

Sample Name	Description	Latitude (N)	Longitude (E)	Quartz	Orthoclase	Albite	Anorthite	Nepheline	Corundum	Diopside	Hypersthene	Wollastonite	Olivine	Magnetite	Ilmenite	Apatite	Total
S09-124	Felsic Dike	23.027000	44.977680	36.89	2.72	42.47	11.03	0.00	0.00	6.08	0.00	0.17	0.00	0.25	0.29	0.12	100.01
S09-036	Trondhjemite	23.105080	44.967630	8.65	12.36	36.76	19.71	0.00	0.00	12.19	6.83	0.00	0.00	0.95	1.95	0.60	100.01
S09-037	Trondhjemite	23.104070	44.966700	25.40	4.63	49.41	14.72	0.00	0.14	0.00	4.62	0.00	0.00	0.36	0.51	0.21	100.01
S09-039	Trondhjemite	23.103020	44.967670	25.40	7.57	48.59	14.26	0.00	0.00	0.10	3.29	0.00	0.00	0.25	0.37	0.17	100.01
S09-045	Trondhjemite	23.108970	44.966580	17.79	8.26	41.33	20.91	0.00	0.00	0.47	8.86	0.00	0.00	0.69	1.33	0.36	100.01
S09-046	Trondhjemite	23.110120	44.966980	25.28	14.95	38.34	13.86	0.00	1.04	0.00	5.21	0.00	0.00	0.41	0.65	0.26	100.01
S09-048	Trondhjemite	23.111140	44.969250	20.26	8.79	37.41	22.05	0.00	0.24	0.00	8.93	0.00	0.00	0.67	1.31	0.36	100.01
S09-068	Trondhjemite	23.105380	44.963540	20.11	14.97	43.24	11.95	0.00	1.64	0.00	6.59	0.00	0.00	0.47	0.74	0.29	100.01
S09-074	Trondhjemite	23.102000	44.947220	28.42	16.20	37.14	14.03	0.00	0.00	0.06	3.19	0.00	0.00	0.32	0.48	0.17	100.01
S09-084	Trondhjemite	23.123910	44.977600	23.36	7.40	48.19	14.59	0.00	0.00	1.50	3.89	0.00	0.00	0.35	0.51	0.22	100.01
S09-088	Trondhjemite	23.137450	44.949990	28.12	11.97	44.34	10.55	0.00	1.14	0.00	3.18	0.00	0.00	0.25	0.34	0.12	100.01
S09-099	Trondhjemite	23.112100	44.949730	27.98	15.87	37.61	13.35	0.00	0.41	0.00	3.71	0.00	0.00	0.36	0.51	0.19	100.01
S09-061	Mafic Dike	23.108920	44.961550	9.61	1.14	25.29	28.78	0.00	0.00	3.95	25.40	0.00	0.00	2.34	1.80	1.70	100.01
S09-081	Mafic Dike	23.131080	44.988140	14.18	13.43	37.46	14.88	0.00	0.00	0.85	16.10	0.00	0.00	1.20	1.43	0.48	100.01
S09-111	Mafic Dike	23.070510	44.990140	0.45	0.37	24.46	25.15	0.00	0.00	31.69	14.89	0.00	0.00	1.61	1.11	0.28	100.01
S09-112	Mafic Dike	23.064600	44.993250	8.44	4.57	36.87	22.55	0.00	0.00	4.83	19.25	0.00	0.00	1.23	1.88	0.37	100.01
S09-125	Mafic Dike	23.118130	45.025320	0.00	0.23	20.31	30.03	0.57	0.00	27.79	0.00	0.00	17.99	1.79	1.14	0.16	100.01
S09-104	Mafic Intrusive			0.00	15.21	33.37	22.06	0.00	0.00	8.65	10.62	0.00	5.73	1.62	1.58	1.18	100.01
S09-108	Mafic Intrusive			0.00	0.20	18.94	29.88	0.00	0.00	33.86	0.59	0.00	14.49	1.35	0.59	0.10	100.01
S09-110	Mafic Intrusive	23.036210	44.934290	0.00	3.79	33.33	32.66	0.00	0.00	8.70	11.34	0.00	6.60	1.62	1.42	0.55	100.01
S09-115	Mafic Intrusive	23.052860	44.984390	0.00	2.34	25.34	36.81	1.53	0.00	18.28	0.00	0.00	12.41	1.72	1.44	0.14	100.01
S09-117B	Mafic Intrusive	23.052860	44.984390	0.00	0.15	17.38	35.07	0.00	0.00	25.81	15.62	0.00	3.71	1.41	0.75	0.09	100.01

Table 16. Normative CIPW values

11.14 Nd-Sm TIMS Data

Sample Name		Latitude (N)	Longitude (E)	[Nd] ppm	[Sm] ppm	*143/144*	*150/144*	Ep(0)	Ep(T)	T_{DM} (Ma)
S09-007	Halaban Diorite	23.477944	44.364389	9.53	2.15	0.5125582	0.1363792	-1.6	3.6	1154
S09-008	Halaban Diorite	23.477944	44.364389	9.15	2.16	0.5126069	0.1430011	-0.6	4.0	1157
S09-045	Trondhjemite	23.108970	44.966580	9.76	2.06	0.5126042	0.1275677	-0.7	4.9	957
S09-088	Trondhjemite	23.137450	44.949990	4.22	0.79	0.5125502	0.1129574	-1.7	5.1	900
S09-125	Gabbro	23.107450	45.016140	2.93	1.24	0.5132741	0.2553657	12.4	7.5	464
S09-115	Gabbro	23.052860	44.984390	1.70	0.79	0.5133880	0.2803620	14.6	7.7	551
S09-108	Gabbro	23.037720	44.928690	11.00	2.62	0.5122149	0.1441538	-8.3	-3.9	2019
S09-085	Felsic Dike	23.123460	44.977300	5.23	0.94	0.5128180	0.1085343	3.5	10.6	478

Table 17. Nd-Sm TIMS data

11.15 $\delta^{13}C$ Analysis of Carbonates

Seq. #	Standard	Measured d13C	Accepted d13C	Seq. #	Sample Name	Measured d13C	Corrected d13C (PDB)	Atom (%) 13C	Beam (Amps)	Rock Type
1	UA Sucrose	-29.13	-25.79	5	S09-040	-12.18	-12.02	1.09785	1.02E-08	Carbonate Vein
2	L-SVEC LiCO3	-48.17	-46.60	6	S09-058	-10.72	-10.70	1.09945	6.82E-09	Carbonate Vein
3	ANUP3	-0.59	-2.40	7	S09-059	-12.48	-12.29	1.09752	7.02E-09	Carbonate Vein
4	ANUP3	-0.77	-2.40	12	S09-018	-11.57	-11.47	1.09851	8.19E-09	Carbonate Vein
10	L-SVEC LiCO3	-50.00	-46.60	13	S09-017	-10.93	-10.89	1.09922	7.87E-09	Carbonate Vein
22	L-SVEC LiCO3	-50.27	-46.60	17	S09-056	-11.95	-11.81	1.0981	6.12E-09	Carbonate Vein
23	ANUP3	-0.71	-2.40	18	S09-055	-12.15	-11.99	1.09787	4.79E-09	Carbonate Vein
24	UA Glycine	-34.58	-31.20	8	S09-091	-6.35	-6.76	1.10425	7.08E-09	Cauliflower Carbonate
25	UA Glutamic	-19.40	-17.10	9	S09-027	-7.39	-7.69	1.10311	6.85E-09	Cauliflower Carbonate
26	UA Sucrose	-28.67	-25.79	11	S09-030	-6.06	-6.50	1.10457	6.86E-09	Cauliflower Carbonate
				14	S09-025	-5.82	-6.28	1.10484	8.91E-09	Massive Carbonate
				15	S09-042	-5.08	-5.61	1.10565	5.70E-09	Massive Carbonate
				16	S09-032	-5.34	-5.85	1.10537	1.11E-08	Massive Carbonate
				19	S09-062	-4.61	-5.19	1.10619	3.89E-09	Massive Carbonate + Pyrite
				20	S09-063	-4.61	-5.19	1.11622	3.89E-09	Massive Carbonate + Pyrite
				21	S09-0102	-4.35	-4.95	1.10645	5.87E-09	Massive Carbonate + Pyrite

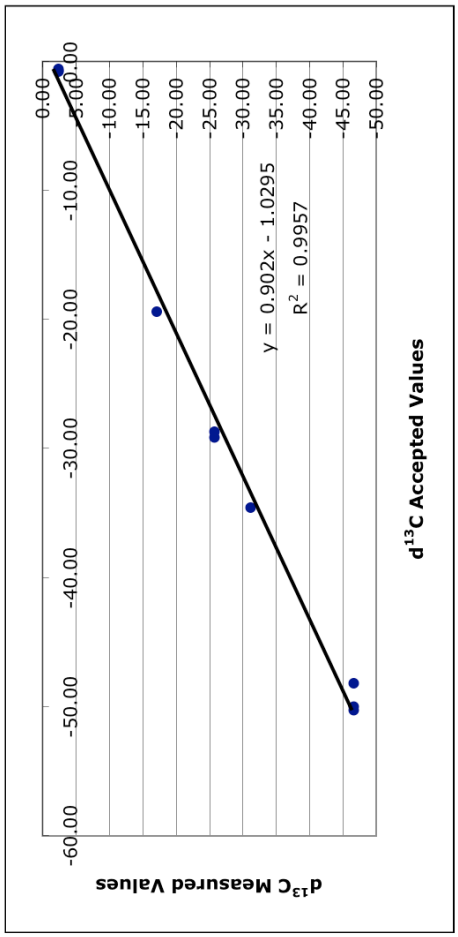

Table 18. Stable isotope data

11.16 Rf/ϕ Analysis of Abt Schist Conglomerate Clasts

Clast #	Reference Line		Clast Long Axis		Clast Length				
	Plunge	Plunge Direction	Plunge	Plunge Direction	Long Axis	Short Axis	Phi	Rf	ln Rf
5	50	124	35	185	360	40	0	9.0	2.2
48	54	120	52	188	155	22	-3	7.0	2.0
12	52	118	40	202	335	48	-17	7.0	1.9
16	58	130	40	160	240	35	25	6.9	1.9
59	62	142	30	180	170	25	5	6.8	1.9
25	52	105	36	165	135	20	20	6.8	1.9
2	40	130	40	180	290	45	5	6.4	1.9
72	68	120	40	188	180	30	-3	6.0	1.8
73	68	120	40	188	180	30	-3	6.0	1.8
39	52	120	58	172	135	23	13	5.9	1.8
34	60	128	58	205	125	22	-20	5.7	1.7
29	65	138	38	190	80	15	-5	5.3	1.7
75	60	125	42	188	160	30	-3	5.3	1.7
63	58	130	48	164	260	50	21	5.2	1.6
71	68	120	54	180	155	30	5	5.2	1.6
68	40	120	20	168	180	35	17	5.1	1.6
22	40	100	49	164	205	40	21	5.1	1.6
32	60	128	51	200	175	35	-15	5.0	1.6
76	60	130	23	176	150	30	9	5.0	1.6
36	60	128	54	205	130	27	-20	4.8	1.6
45	40	125	34	200	140	30	-15	4.7	1.5
49	52	170	52	192	70	15	-7	4.7	1.5
79	49	125	48	174	280	60	11	4.7	1.5
23	60	130	42	205	225	50	-20	4.5	1.5
33	60	128	42	208	110	25	-23	4.4	1.5
66	60	120	49	172	170	40	13	4.3	1.4
4	40	120	40	175	230	55	10	4.2	1.4
51	56	126	52	200	145	35	-15	4.1	1.4
35	60	128	59	208	150	37	-23	4.1	1.4
69	68	140	46	162	240	60	23	4.0	1.4
43	62	115	52	185	90	23	0	3.9	1.4
54	55	126	55	184	115	30	1	3.8	1.3
3	40	120	46	170	190	50	15	3.8	1.3
83	60	130	34	210	170	45	-25	3.8	1.3
89	50	130	56	174	320	85	11	3.8	1.3
93	69	130	30	180	110	30	5	3.7	1.3
17	62	132	40	174	200	55	11	3.6	1.3
28	65	138	40	192	125	35	-7	3.6	1.3
82	60	128	52	180	50	14	5	3.6	1.3
38	60	130	40	170	70	20	15	3.5	1.3
84	60	110	40	175	70	20	10	3.5	1.3
91	54	130	46	182	190	55	3	3.5	1.2
26	52	105	29	178	120	35	7	3.4	1.2
60	62	142	44	182	135	40	3	3.4	1.2
81	60	128	36	184	150	45	1	3.3	1.2
100	45	130	32	186	150	45	-1	3.3	1.2
24	60	130	50	196	65	20	-11	3.3	1.2
52	56	126	52	190	65	20	-5	3.3	1.2
95	58	120	30	194	80	25	-9	3.2	1.2
18	60	132	52	185	110	35	0	3.1	1.1
15	49	130	44	190	310	100	-5	3.1	1.1
27	70	120	44	192	60	20	-7	3.0	1.1
31	60	128	50	140	60	20	45	3.0	1.1
94	58	120	20	180	190	65	5	2.9	1.1
74	70	130	46	190	130	45	-5	2.9	1.1
92	69	130	40	172	130	45	13	2.9	1.1
61	62	142	42	192	100	35	-7	2.9	1.0
55	60	120	60	158	170	60	27	2.8	1.0
87	52	128	28	150	70	25	35	2.8	1.0
58	46	129	42	160	40	15	25	2.7	1.0
67	60	140	46	190	120	45	-5	2.7	1.0

Rf(max)	9.0
Rf(min)	1.2
Rs	3.2
Ri(max)	2.8
n_a	30
n_b	23
n_c	16
n_d	30
I_{syn}	0.79

Table 19. Data table for Abt Schist conglomerate clasts

Clast #	Reference Line		Clast Long Axis		Clast Length				
	Plunge	Plunge Direction	Plunge	lunge Directio	Long Axis	Short Axis	Phi	Rf	ln Rf
11	52	118	50	200	170	65	-15	2.6	1.0
21	60	140	36	160	90	35	25	2.6	0.9
40	52	120	51	170	115	45	15	2.6	0.9
47	54	120	40	194	75	30	-9	2.5	0.9
50	52	120	42	192	125	50	-7	2.5	0.9
53	56	126	42	180	50	20	5	2.5	0.9
90	54	130	42	162	170	70	23	2.4	0.9
7	40	125	65	185	120	50	0	2.4	0.9
8	55	140	50	178	130	55	7	2.4	0.9
80	48	110	32	190	140	60	-5	2.3	0.8
85	52	128	46	150	70	30	35	2.3	0.8
86	52	128	46	150	70	30	35	2.3	0.8
9	50	125	25	145	115	50	40	2.3	0.8
10	50	124	55	156	50	22	29	2.3	0.8
96	62	118	56	162	210	95	23	2.2	0.8
20	60	130	50	180	55	25	5	2.2	0.8
30	65	138	38	192	55	25	-7	2.2	0.8
77	66	120	42	168	110	50	17	2.2	0.8
57	46	129	46	162	120	55	23	2.2	0.8
19	58	130	45	145	130	60	40	2.2	0.8
64	58	130	40	150	65	30	35	2.2	0.8
88	50	130	40	178	130	60	7	2.2	0.8
98	62	118	40	200	65	30	-15	2.2	0.8
42	62	115	48	180	85	40	5	2.1	0.8
13	50	130	48	194	90	45	-9	2.0	0.7
56	50	125	40	174	110	55	11	2.0	0.7
78	49	125	48	174	80	40	11	2.0	0.7
99	60	120	36	190	50	25	-5	2.0	0.7
97	62	118	56	162	85	45	23	1.9	0.6
14	50	130	66	205	60	32	-20	1.9	0.6
46	40	125	42	195	70	38	-10	1.8	0.6
41	62	115	28	164	135	75	21	1.8	0.6
44	40	125	56	194	90	50	-9	1.8	0.6
70	52	118	32	160	80	45	25	1.8	0.6
6	40	125	44	175	85	50	10	1.7	0.5
37	60	130	46	200	50	30	-15	1.7	0.5
65	50	122	34	180	75	45	5	1.7	0.5
1	65	120	55	180	130	80	5	1.6	0.5
62	62	142	40	182	35	30	3	1.2	0.2
Mean	55.9	126.2	43.7	179.9	132.6	40.1	5.1	3.5	1.2
S.D.	7.9	9.1	9.3	15.9	69.0	17.3	15.9	1.5	0.4
RSD%	14.1	7.2	21.3	8.9	52.1	43.1	310.4	44.3	36.3

Table 19 cont. Data table for Abt Schist conglomerate clasts

11.17 Probe data of Plagioclase in Gabbro

Sample Name: **S09-122 Gabbro**
Latitude (N) 23.03000
Longitude (E) 44.98146

Analysis No.	Plag1	Plag2	Plag3	Plag4	Plag5	Plag6	Plag7	Plag8	Plag9	Plag10	Plag11	Plag12	Plag13	Plag14
Raw Weight % Oxide														
SiO2	44.29	38.09	54.51	48.13	51.74	44.40	56.95	49.73	55.08	44.58	60.32	49.36	47.72	51.85
TiO2	0.02	0.28	0.00	0.02	0.00	0.00	0.01	0.00	0.00	0.00	0.00	0.00	0.02	0.01
Al2O3	29.57	27.83	24.39	27.11	26.52	29.91	24.72	28.56	25.87	29.96	25.30	29.10	30.46	26.98
Cr2O3	0.04	0.33	0.00	0.00	0.00	0.01	0.04	0.03	0.01	0.03	0.01	0.00	0.00	0.01
FeO	2.42	5.95	0.69	0.82	1.14	0.83	0.49	1.10	1.30	0.77	0.71	1.19	0.52	1.36
MnO	0.01	0.12	0.04	0.04	0.03	0.04	0.04	0.04	0.05	0.07	0.00	0.02	0.00	0.03
MgO	0.00	0.12	0.01	0.01	0.00	0.05	0.01	0.00	0.01	0.03	0.00	0.03	0.01	0.00
ZnO	0.00	0.00	0.00	0.00	0.00	0.00	0.00	0.00	0.00	0.00	0.00	0.00	0.00	0.00
CaO	21.58	23.86	9.69	15.94	14.80	20.94	9.74	17.14	12.86	20.95	9.98	18.22	19.23	15.82
Na2O	1.57	0.01	7.04	3.83	4.88	2.15	6.81	3.53	4.73	1.58	6.66	2.66	2.57	3.61
K2O	0.00	0.01	0.02	0.04	0.03	0.02	0.03	0.00	0.03	0.01	0.03	0.00	0.01	0.03
Total	99.50	96.60	96.39	95.94	99.16	98.36	98.84	100.13	99.93	97.98	103.02	100.58	100.54	99.70
Cation Calculation														
Si	2.11	1.94	2.57	2.32	2.41	2.13	2.60	2.30	2.51	2.14	2.63	2.28	2.21	2.40
Ti	0.00	0.01	0.00	0.00	0.00	0.00	0.00	0.00	0.00	0.00	0.00	0.00	0.00	0.00
Al	1.66	1.67	1.35	1.54	1.45	1.69	1.33	1.56	1.39	1.69	1.30	1.58	1.66	1.47
Cr	0.00	0.01	0.00	0.00	0.00	0.00	0.00	0.00	0.00	0.00	0.00	0.00	0.00	0.00
Fe2+	0.10	0.25	0.03	0.03	0.04	0.03	0.02	0.04	0.05	0.03	0.03	0.05	0.02	0.05
Mn2+	0.00	0.00	0.00	0.00	0.00	0.00	0.00	0.00	0.00	0.00	0.00	0.00	0.00	0.00
Mg	0.00	0.01	0.00	0.00	0.00	0.00	0.00	0.00	0.00	0.00	0.00	0.00	0.00	0.00
Zn	0.00	0.00	0.00	0.00	0.00	0.00	0.00	0.00	0.00	0.00	0.00	0.00	0.00	0.00
Ca	1.10	1.30	0.49	0.82	0.74	1.07	0.48	0.85	0.63	1.08	0.47	0.90	0.95	0.78
Na	0.14	0.00	0.64	0.36	0.44	0.20	0.60	0.32	0.42	0.15	0.56	0.24	0.23	0.32
K	0.00	0.00	0.00	0.00	0.00	0.00	0.00	0.00	0.00	0.00	0.00	0.00	0.00	0.00
Ni	0.00	0.00	0.00	0.00	0.00	0.00	0.00	0.00	0.00	0.00	0.00	0.00	0.00	0.00
Cl	0.00	0.00	0.00	0.00	0.00	0.00	0.00	0.00	0.00	0.00	0.00	0.00	0.00	0.00
F	0.00	0.00	0.00	0.00	0.00	0.00	0.00	0.00	0.00	0.00	0.00	0.00	0.00	0.00
Total	5.13	5.21	5.08	5.09	5.09	5.13	5.04	5.08	5.00	5.09	5.00	5.05	5.08	5.03
Cation Calculation Incorporating Fe^{3+}														
Si	2.06	1.86	2.53	2.28	2.37	2.07	2.58	2.27	2.51	2.10	2.64	2.26	2.18	2.38
Ti	0.00	0.01	0.00	0.00	0.00	0.00	0.00	0.00	0.00	0.00	0.00	0.00	0.00	0.00
Al	1.62	1.60	1.33	1.52	1.43	1.65	1.32	1.54	1.39	1.66	1.30	1.57	1.64	1.46
Cr	0.00	0.01	0.00	0.00	0.00	0.00	0.00	0.00	0.00	0.00	0.00	0.00	0.00	0.00
Fe3+	0.39	0.64	0.25	0.27	0.27	0.40	0.11	0.24	0.01	0.28	0.00	0.16	0.24	0.10
Fe2+	-0.30	-0.39	-0.22	-0.24	-0.23	-0.37	-0.09	-0.19	0.04	-0.25	0.03	-0.11	-0.22	-0.04
Mn2+	0.00	0.00	0.00	0.00	0.00	0.00	0.00	0.00	0.00	0.00	0.00	0.00	0.00	0.00
Mg	0.00	0.01	0.00	0.00	0.00	0.00	0.00	0.00	0.00	0.00	0.00	0.00	0.00	0.00
Zn	0.00	0.00	0.00	0.00	0.00	0.00	0.00	0.00	0.00	0.00	0.00	0.00	0.00	0.00
Ca	1.08	1.25	0.48	0.81	0.73	1.05	0.47	0.84	0.63	1.06	0.47	0.89	0.94	0.78
Na	0.14	0.00	0.63	0.35	0.43	0.19	0.60	0.31	0.42	0.14	0.56	0.24	0.23	0.32
K	0.00	0.00	0.00	0.00	0.00	0.00	0.00	0.00	0.00	0.00	0.00	0.00	0.00	0.00
Ni	0.00	0.00	0.00	0.00	0.00	0.00	0.00	0.00	0.00	0.00	0.00	0.00	0.00	0.00
Cl	0.00	0.00	0.00	0.00	0.00	0.00	0.00	0.00	0.00	0.00	0.00	0.00	0.00	0.00
F	0.00	0.00	0.00	0.00	0.00	0.00	0.00	0.00	0.00	0.00	0.00	0.00	0.00	0.00
Total	5.00	5.00	5.00	5.00	5.00	5.00	5.00	5.00	5.00	5.00	5.00	5.00	5.00	5.00
%An	88.49	89.93	77.44	85.27	83.82	88.21	77.16	85.68	81.77	88.30	76.95	86.44	87.03	84.76
Recalculated Weight % Oxide Incorporating Fe_2O_3														
SiO2	44.02	38.73	56.13	49.78	51.77	44.62	57.43	49.32	55.10	45.13	58.56	48.85	47.13	51.87
TiO2	0.02	0.29	0.00	0.02	0.00	0.00	0.01	0.00	0.00	0.00	0.00	0.00	0.02	0.01
Al2O3	29.39	28.30	25.12	28.04	26.54	30.06	24.93	28.33	25.88	30.33	24.56	28.80	30.09	26.99
Cr2O3	0.04	0.33	0.00	0.00	0.00	0.01	0.04	0.03	0.01	0.03	0.01	0.00	0.00	0.01
Fe2O3	11.09	17.62	7.42	7.81	7.93	11.58	3.30	6.84	0.25	8.06	0.00	4.49	6.89	2.77
FeO	-7.57	-9.80	-5.97	-6.18	-6.00	-9.58	-2.47	-5.06	1.08	-6.48	0.69	-2.86	-5.68	-1.13
MnO	0.01	0.12	0.04	0.04	0.03	0.04	0.04	0.04	0.05	0.07	0.00	0.02	0.00	0.03
MgO	0.00	0.13	0.02	0.01	0.00	0.05	0.01	0.00	0.01	0.03	0.00	0.03	0.01	0.00
ZnO	0.00	0.00	0.00	0.00	0.00	0.00	0.00	0.00	0.00	0.00	0.00	0.00	0.00	0.00
CaO	21.44	24.27	9.97	16.49	14.81	21.04	9.82	17.00	12.86	21.21	9.69	18.03	18.99	15.82
Na2O	1.56	0.01	7.25	3.96	4.88	2.16	6.87	3.50	4.73	1.60	6.46	2.63	2.54	3.61
K2O	0.00	0.01	0.02	0.04	0.03	0.02	0.03	0.00	0.03	0.01	0.03	0.00	0.01	0.03
NiO	0.00	0.00	0.00	0.00	0.00	0.00	0.00	0.00	0.00	0.00	0.00	0.00	0.00	0.00
Total	100.00	100.00	100.00	100.00	100.00	100.00	100.00	100.00	100.00	100.00	100.00	100.00	100.00	100.00

Table 20. Probe data obtained from a gabbro sample for the mineral plagioclase

11.18 Probe data of Chrome Spinels in Cumulate

Sample #	S09-090	Ultramafic Cumulate																					
	Latitude (N)	23.09802																					
	Longitude (E)	44.97362																					
Major oxides																							
	crspin-1	crspin-2	crspin-3	crspin-4	crspin-5	crspin-6	crspin-7	crspin-8	crspin-10	crspin-11	crspin-12	crspin-13	crspin-14	crspin-15	crspin-16	crspin-17	crspin-18	crspin-19	crspin-20	crspin-21	crspin-22		
SiO_2	0.023	0.0373	0.0489	0.0003	0.0672	0.0699	0.0003	0.0173	0.0968	0.0986	0.0798	0.0425	0.0441	0.0221	0.0395	0.1435	0.0609	0.1591	0.0623	0.0003	0.8212		
TiO_2	0.4444	0.4905	0.459	0.4666	0.4321	0.4989	0.4511	0.3987	0.5114	0.5253	0.3615	0.4942	0.663	0.6431	0.7659	0.6653	0.6337	0.6855	0.6556	0.4957	0.0718		
Al_2O_3	21.8687	22.0602	22.4309	21.4652	22.8915	22.0552	22.2593	22.9749	22.0481	21.7369	23.5955	4.5011	1.3317	2.082	1.3448	0.9553	0.6427	0.8223	1.7811	2.9446	0.0058		
Cr_2O_3	35.7803	36.0309	36.1548	37.2936	35.7231	35.8708	36.108	35.4098	35.456	35.6917	35.6427	30.4548	27.1378	28.1442	26.7328	24.0377	21.4844	24.5762	27.8562	25.468	0.8566		
FeO	32.5807	32.5959	32.1214	31.4023	31.3405	32.5374	31.9229	31.4419	32.9833	31.2845	29.8495	56.3284	62.2508	58.7602	60.8164	63.1546	67.1464	63.3461	58.171	61.9952	85.3699		
MnO	0.4115	0.4709	0.4465	0.4445	0.5244	0.5278	0.5032	0.403	0.465	0.525	0.5221	0.7275	1.2591	0.938	1.4731	1.5523	1.1949	1.5767	1.9342	1.6722	0.0722		
MgO	6.8525	6.6709	6.8832	6.9683	7.5745	6.7914	7.1485	7.271	6.8967	6.6699	7.3449	1.3488	0.6629	0.984	0.6026	0.4547	0.3866	0.5623	0.337	0.4849	0.2081		
CaO	0.0087	0.0035	0.0104	0.0001	0.0001	0.0001	0.0001	0.0001	0.0226	0.007	0.0001	0.0293	0.0333	0.0501	0.0042	0.0017	0.0001	0.0433	0.0466	0.0685	0.0948		
Na_2O	0.0262	0.0139	0.0706	0.0739	0.015	0.0079	0.0349	0.0297	0.0418	0.0004	0.0347	0.0227	0.0067	0.0029	0.0115	0.0248	0.0118	0.0512	0.0435	0.0531	0.0005		
K_2O	0.0001	0.0101	0.0001	0.0189	0.0057	0.0016	0.0048	0.0085	0.0001	0.0133	0.0001	0.0039	0.0001	0.0027	0.0001	0.0046	0.0093	0.0015	0.0097	0.0066	0.0364		
Cation calculations																							
Si	0.0007	0.0012	0.0016	0.0000	0.0022	0.0023	0.0000	0.0006	0.0031	0.0033	0.0026	0.0016	0.0017	0.0009	0.0016	0.0057	0.0024	0.0063	0.0021	0.0000	0.0335		
Ti	0.0109	0.0120	0.0111	0.0114	0.0104	0.0122	0.0109	0.0097	0.0124	0.0130	0.0088	0.0140	0.0192	0.0189	0.0226	0.0198	0.0188	0.0203	0.0196	0.0143	0.0022		
Al	0.8378	0.8429	0.8522	0.8220	0.8648	0.8421	0.8465	0.8741	0.8395	0.8454	0.8994	0.1999	0.0606	0.0960	0.0623	0.0447	0.0299	0.0381	0.0833	0.1332	0.0003		
Cr	0.9196	0.9235	0.9214	0.9581	0.9053	0.9188	0.9212	0.9037	0.9056	0.9312	0.9114	0.9074	0.8281	0.8706	0.8303	0.7538	0.6700	0.7633	0.8740	0.7730	0.0277		
Fe^{3+}	0.2211	0.2086	0.2054	0.2025	0.2060	0.2107	0.2128	0.2039	0.2264	0.1913	0.1687	0.8633	1.0699	0.9941	1.0599	1.1526	1.2591	1.1496	1.0033	1.0694	1.9025		
Fe^{2+}	0.6646	0.6751	0.6605	0.6507	0.6340	0.6708	0.6485	0.6449	0.6646	0.6720	0.6386	0.9117	0.9393	0.9285	0.9379	0.9422	0.9558	0.9313	0.9270	0.9208	1.0126		
Mn^{2+}	0.0113	0.0129	0.0122	0.0122	0.0142	0.0145	0.0138	0.0110	0.0127	0.0147	0.0143	0.0232	0.0412	0.0311	0.0490	0.0521	0.0399	0.0525	0.0650	0.0544	0.0025		
Mg	0.3321	0.3224	0.3308	0.3376	0.3620	0.3280	0.3439	0.3499	0.3322	0.3282	0.3541	0.0758	0.0381	0.0574	0.0353	0.0269	0.0227	0.0329	0.0199	0.0278	0.0127		
Ca	0.0003	0.0001	0.0004	0.0000	0.0000	0.0000	0.0000	0.0000	0.0008	0.0002	0.0000	0.0012	0.0014	0.0021	0.0002	0.0001	0.0000	0.0018	0.0020	0.0028	0.0041		
Na	0.0017	0.0009	0.0044	0.0047	0.0009	0.0005	0.0022	0.0019	0.0026	0.0000	0.0022	0.0017	0.0005	0.0002	0.0009	0.0019	0.0009	0.0039	0.0033	0.0040	0.0000		
K	0.0000	0.0004	0.0000	0.0008	0.0002	0.0001	0.0002	0.0004	0.0000	0.0006	0.0000	0.0002	0.0000	0.0001	0.0000	0.0002	0.0005	0.0001	0.0005	0.0003	0.0019		
Major oxides recalculated incorporating Fe2O3																							
wt% SiO2	0.023	0.038	0.049	0.000	0.068	0.070	0.000	0.018	0.097	0.101	0.081	0.044	0.045	0.023	0.041	0.151	0.064	0.166	0.055	0.000	0.876		
wt% TiO2	0.449	0.494	0.461	0.471	0.435	0.503	0.454	0.404	0.514	0.540	0.368	0.509	0.683	0.677	0.803	0.701	0.661	0.716	0.696	0.512	0.077		
wt% Al2O3	22.112	22.229	22.549	21.690	23.023	22.227	22.414	23.255	22.169	22.334	24.046	4.640	1.372	2.191	1.410	1.007	0.671	0.859	1.890	3.039	0.006		
wt% Cr2O3	36.178	36.307	36.346	37.684	35.928	36.150	36.358	35.841	35.650	36.673	36.324	31.396	27.954	29.622	28.027	25.339	22.421	25.675	29.555	26.283	0.914		
wt% Fe2O3	9.138	8.615	8.511	8.370	8.590	8.712	8.826	8.497	9.366	7.916	7.065	31.387	37.948	35.538	37.593	40.710	44.270	40.630	35.649	38.206	66.055		
wt% FeO	24.720	25.093	24.633	24.199	23.791	24.951	24.202	24.180	24.737	25.021	24.063	29.826	29.976	29.867	29.933	29.943	30.240	29.619	29.640	29.602	31.633		
wt% MnO	0.416	0.475	0.449	0.449	0.527	0.532	0.507	0.408	0.468	0.539	0.532	0.750	1.297	0.987	1.544	1.636	1.247	1.647	2.052	1.726	0.077		
wt% MgO	6.929	6.722	6.920	7.041	7.618	6.844	7.198	7.360	6.934	6.853	7.485	1.390	0.683	1.036	0.632	0.479	0.403	0.587	0.358	0.500	0.222		
wt% CaO	0.009	0.004	0.010	0.000	0.000	0.000	0.000	0.000	0.023	0.007	0.000	0.030	0.034	0.053	0.004	0.002	0.000	0.045	0.049	0.071	0.101		
wt% Na2O	0.026	0.014	0.071	0.075	0.015	0.008	0.035	0.030	0.042	0.000	0.035	0.023	0.007	0.003	0.012	0.026	0.012	0.053	0.046	0.055	0.001		
wt% K2O	0.000	0.010	0.000	0.019	0.006	0.002	0.005	0.009	0.000	0.014	0.000	0.004	0.000	0.003	0.000	0.005	0.010	0.002	0.010	0.007	0.039		
Molar Cr	0.238	0.239	0.239	0.248	0.236	0.238	0.239	0.236	0.235	0.241	0.239	0.207	0.184	0.195	0.184	0.167	0.148	0.169	0.194	0.173	0.006		
Molar Al	0.217	0.218	0.221	0.213	0.226	0.218	0.220	0.228	0.217	0.219	0.236	0.046	0.013	0.021	0.014	0.010	0.007	0.008	0.019	0.030	0.000		
Molar Mg	0.172	0.167	0.172	0.175	0.189	0.170	0.179	0.183	0.172	0.170	0.186	0.034	0.017	0.026	0.016	0.012	0.010	0.015	0.009	0.012	0.006		
Molar Fe^{3+}	0.344	0.349	0.343	0.337	0.331	0.347	0.337	0.337	0.344	0.348	0.335	0.415	0.417	0.416	0.417	0.417	0.421	0.412	0.413	0.412	0.440		
Cr#	0.523	0.523	0.520	0.538	0.511	0.522	0.521	0.508	0.519	0.524	0.503	0.819	0.932	0.901	0.930	0.944	0.957	0.952	0.913	0.853	0.990		
Mg#	0.333	0.323	0.334	0.342	0.363	0.328	0.346	0.352	0.333	0.328	0.357	0.077	0.039	0.058	0.036	0.028	0.023	0.034	0.021	0.029	0.012		

Table 21. Probe data of chrome spinels from ultramafic cumulate

11 APPENDIX

11.1 Figures

11.1.1 Regional geology map of the Arabian Nubian Shield

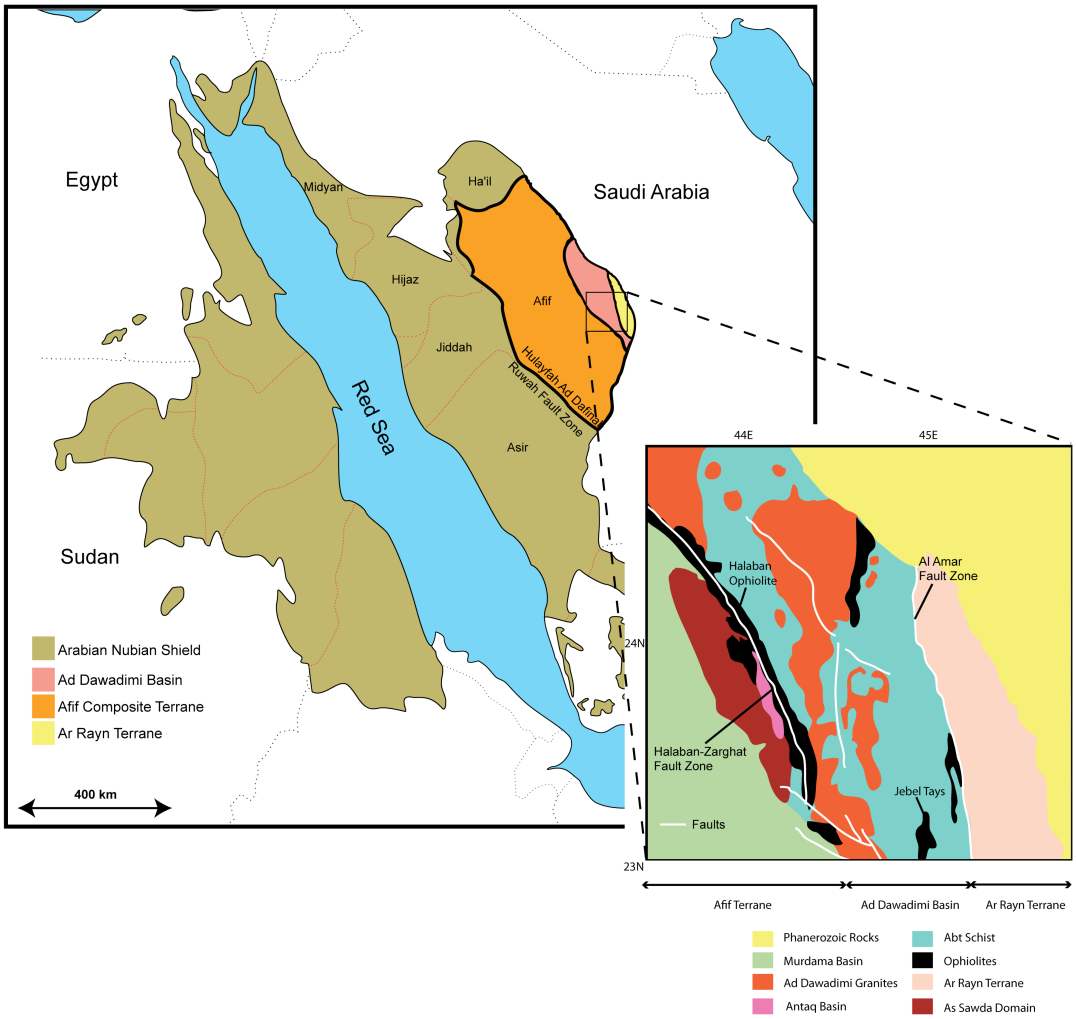

Figure 1. Map showing the current configuration of the exposed portion of the Arabian Nubian Shield. Inset map shows the geology of the eastern portion of the ANS.

11.1.2 Images of serpentinite and trondhjemite lithologies

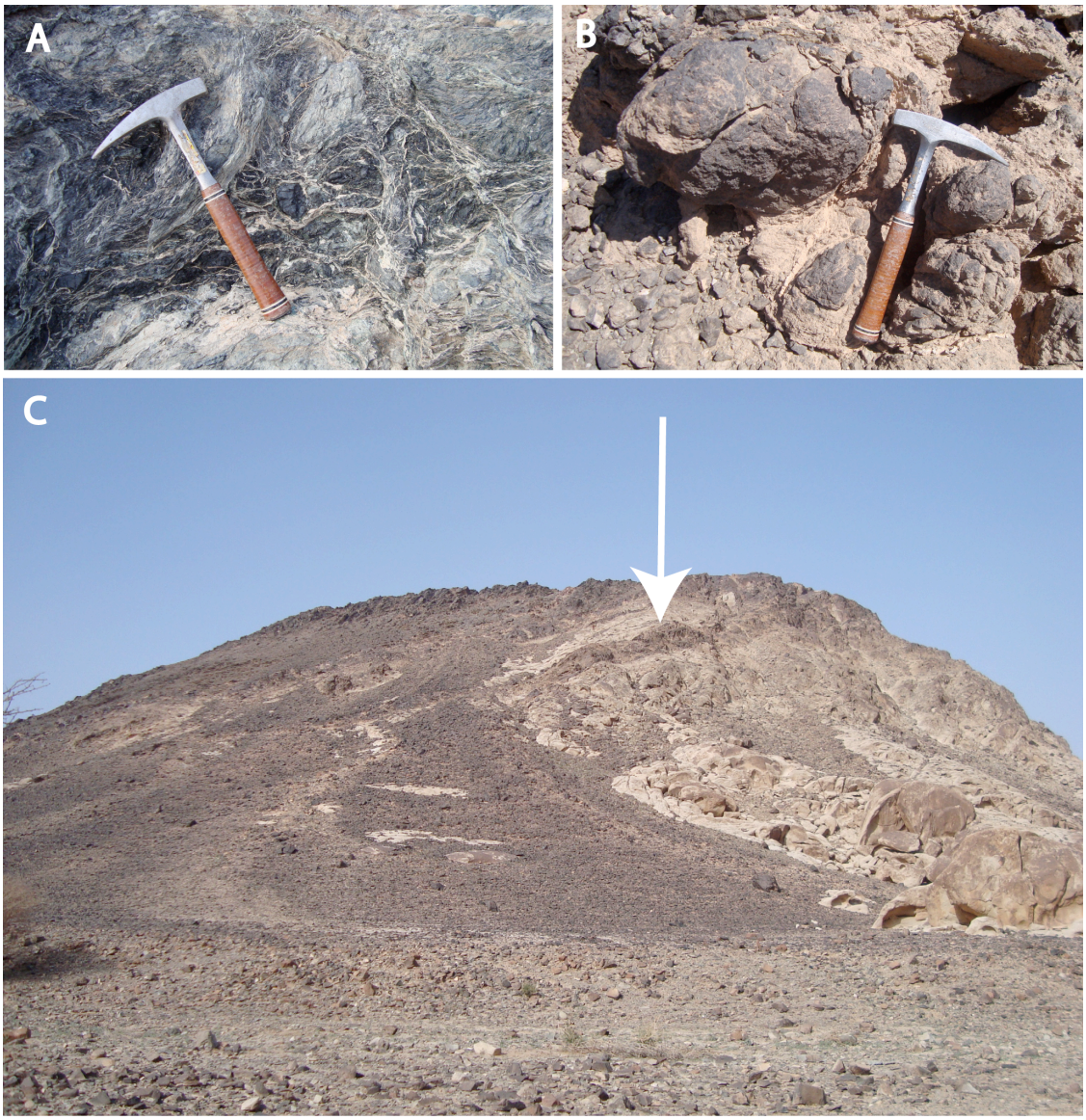

Figure 2. (A) Pebbles in a highly deformed serpentinite matrix. (B) Large boulders and cobbles protruding out of a fine-grained carbonated serpentinite matrix. (C) The main trondhjemite outcrop, arrow marks the position of the sunken roof pendent, photo taken looking north-west Lat: 23º 06.28" N, Lon: 44º 58.16"E.

11.1.3 Images of Abt, trondhjemite and carbonate lithologies

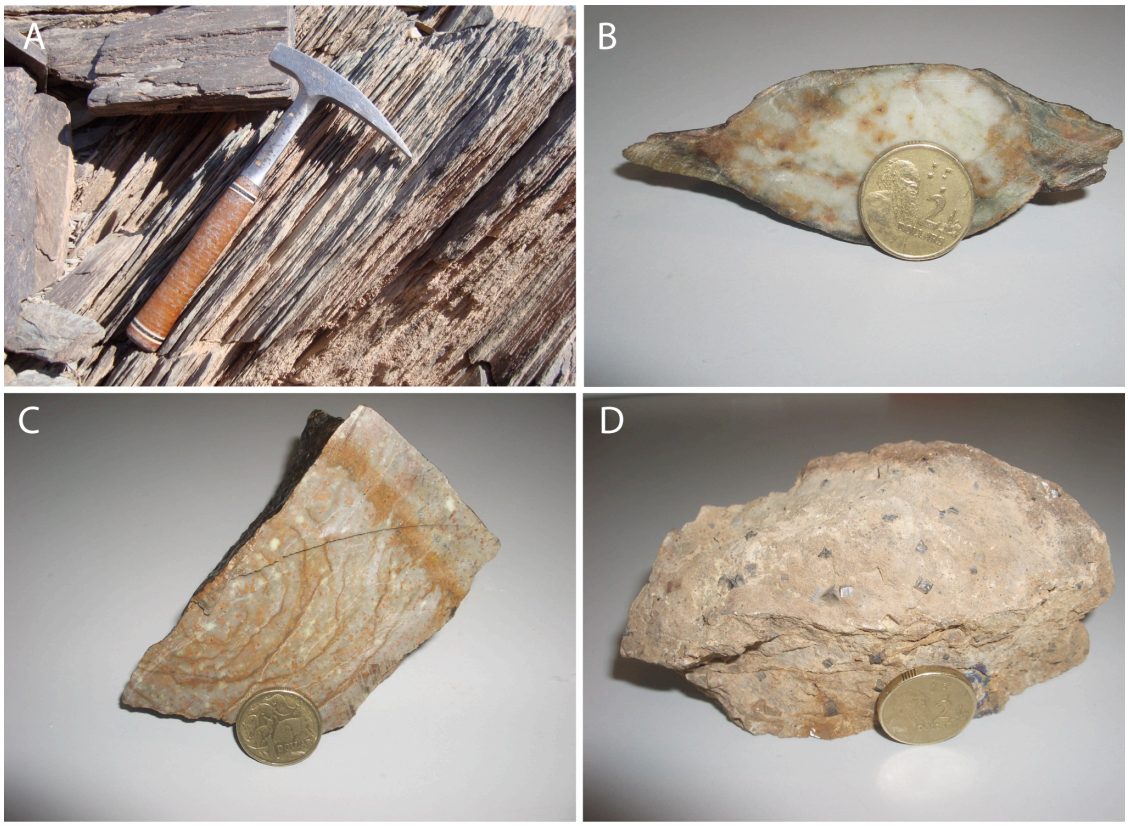

Figure 3. (A) Fine grained highly foliated calcareous silt of the Abt west of Jebel Tays. (B) Elongated sub-volcanic pebble clast from the Abt conglomerate unit east of Jebel Tays, note the metamorphic pressure shadow of muscovite, chlorite and biotite. (C) Coarse grained trondhjemite showing redox flow boundaries caused by post-crystallisation fluid flow. (D) Massive carbonate containing large euhedral pseudomorphed pyrite.

11.1.4 East-west cross section of Jebel Tays

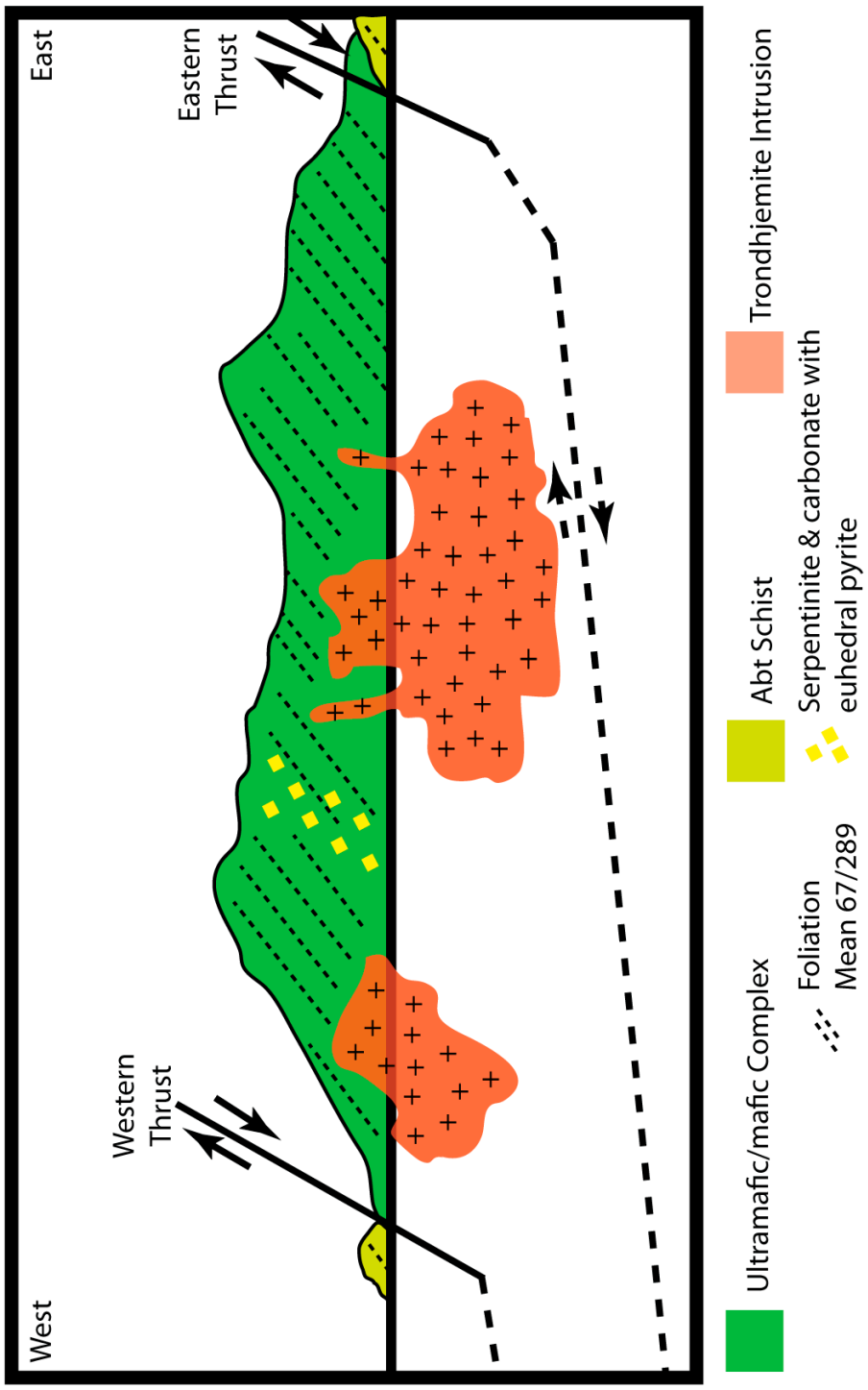

Figure 4. Schematic east-west cross section through Jebel Tays, horizontal distance is ca 4km.

11.1.5 Images of thrust contact and kinematics

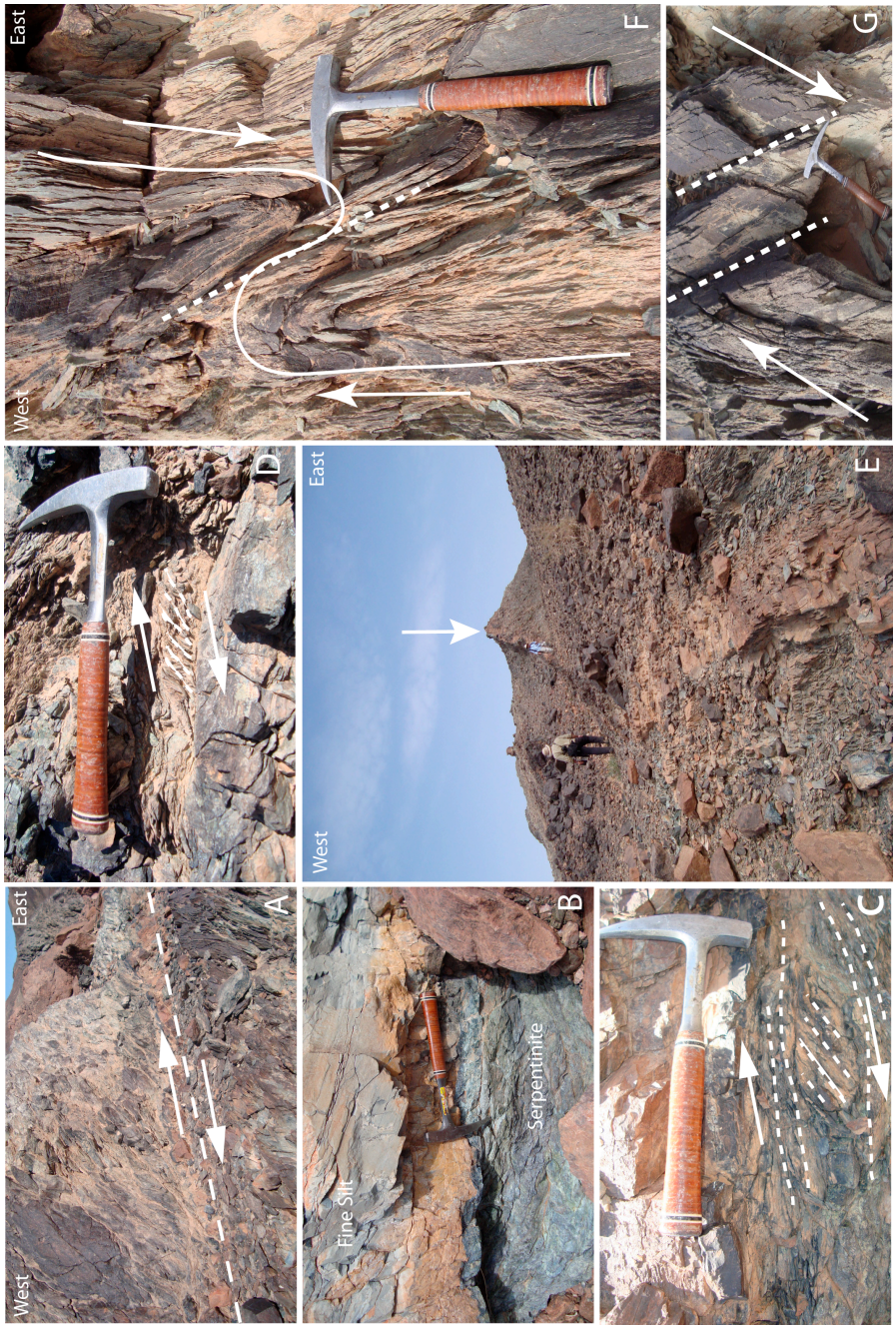

Figure 5. (A) Eastern sub-horizontal contact between serpentinite (top) and Abt (bottom). (B) Sharp contact between serpentinite and Abt siltstone showing that the silt has been moderately baked. (C & D) Dextral kinematic on sub-vertical section of the eastern contact. (E) Eastern contact trending towards the north showing the sub-vertical nature of the contact and the weathering resistant nature of the baked siltstone. (F & G) Asymmetrical folding and thrusting of the Abt near the western thrust contact indicating top to the east movement.

11.1.6 Solid geology map of Jebel Tays

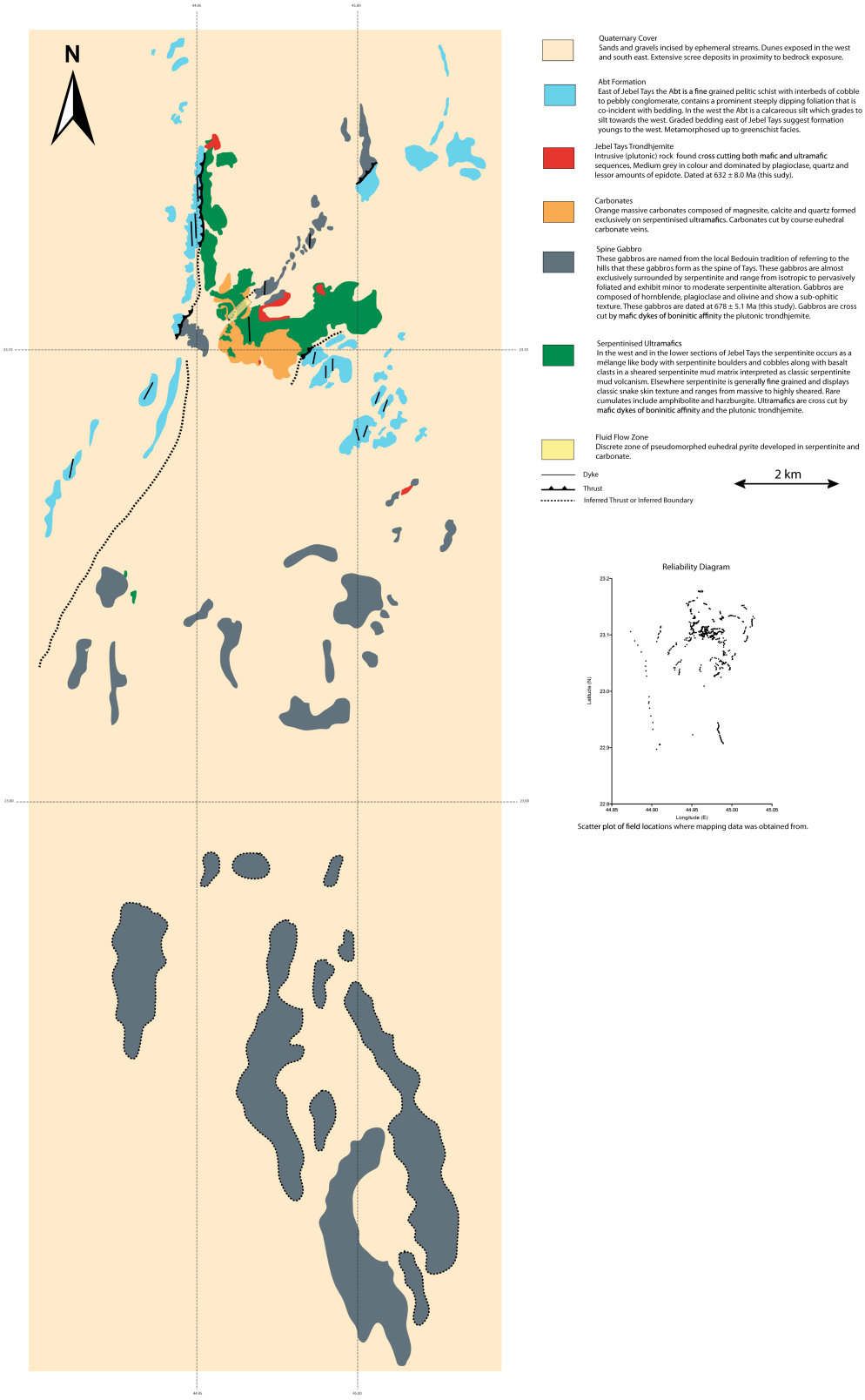

Figure 6. Solid geology map of Jebel Tays and the surrounding mafic / ultramafic rocks and the adjacent Abt Formation.

11.1.7 R_f/ϕ plot of cobble clast data

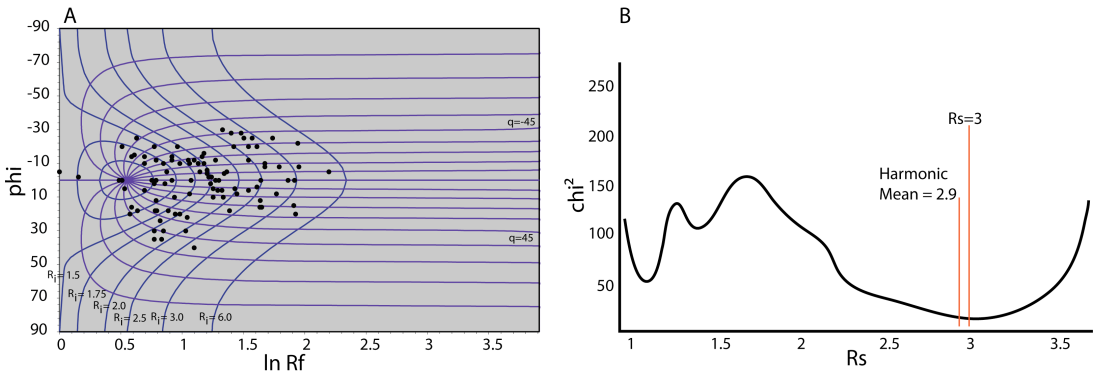

Figure 7. (A) Rf / ln ϕ plot based on 100 conglomerate clasts showing a tight symmetrical grouping indicating that strain is non-random and equates to 10% elongation along a mean north-south direction. (B) Calculation of R_s through the iterative minimisation of χ^2 that acts as a proxy for a random initial distribution. Plots produced by the excel program of Chew (2003)

11.1.8 Stereonet and rose diagram of foliation data

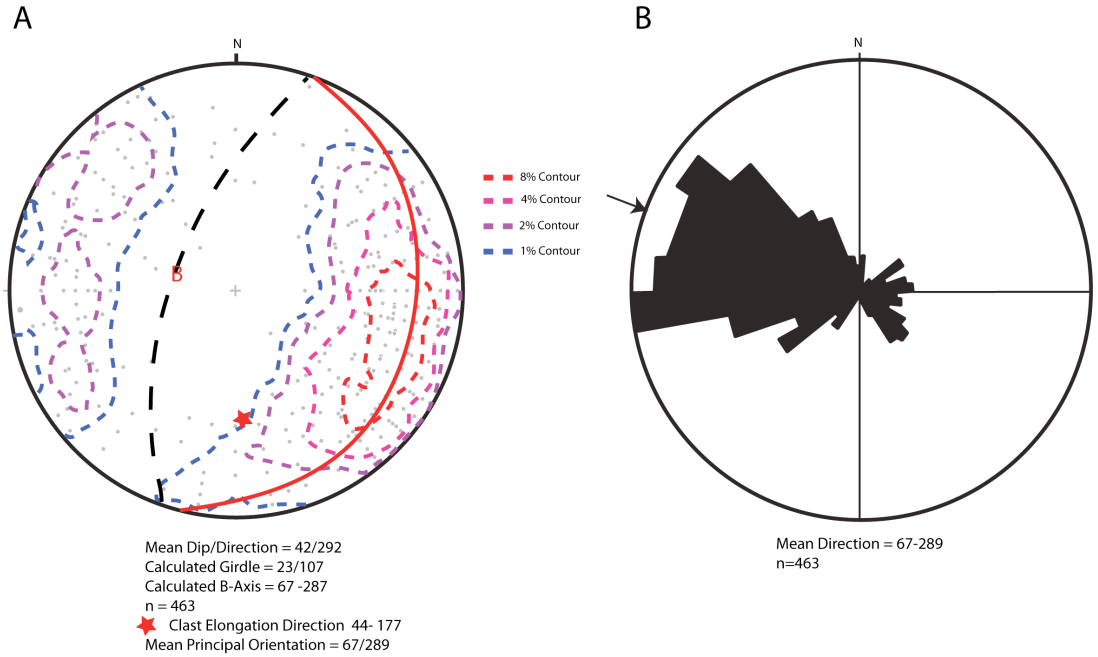

Figure 8. (A) Contoured poles to foliation planes, while there is considerable spread in the data the dominant foliation is orientated north-south, this is consistent with the orientation of both the eastern and western thrusts. (B) Rose diagram showing the dominant dip direction of foliation planes.

11.1.9 Foliation and form surface map of Jebel Tays

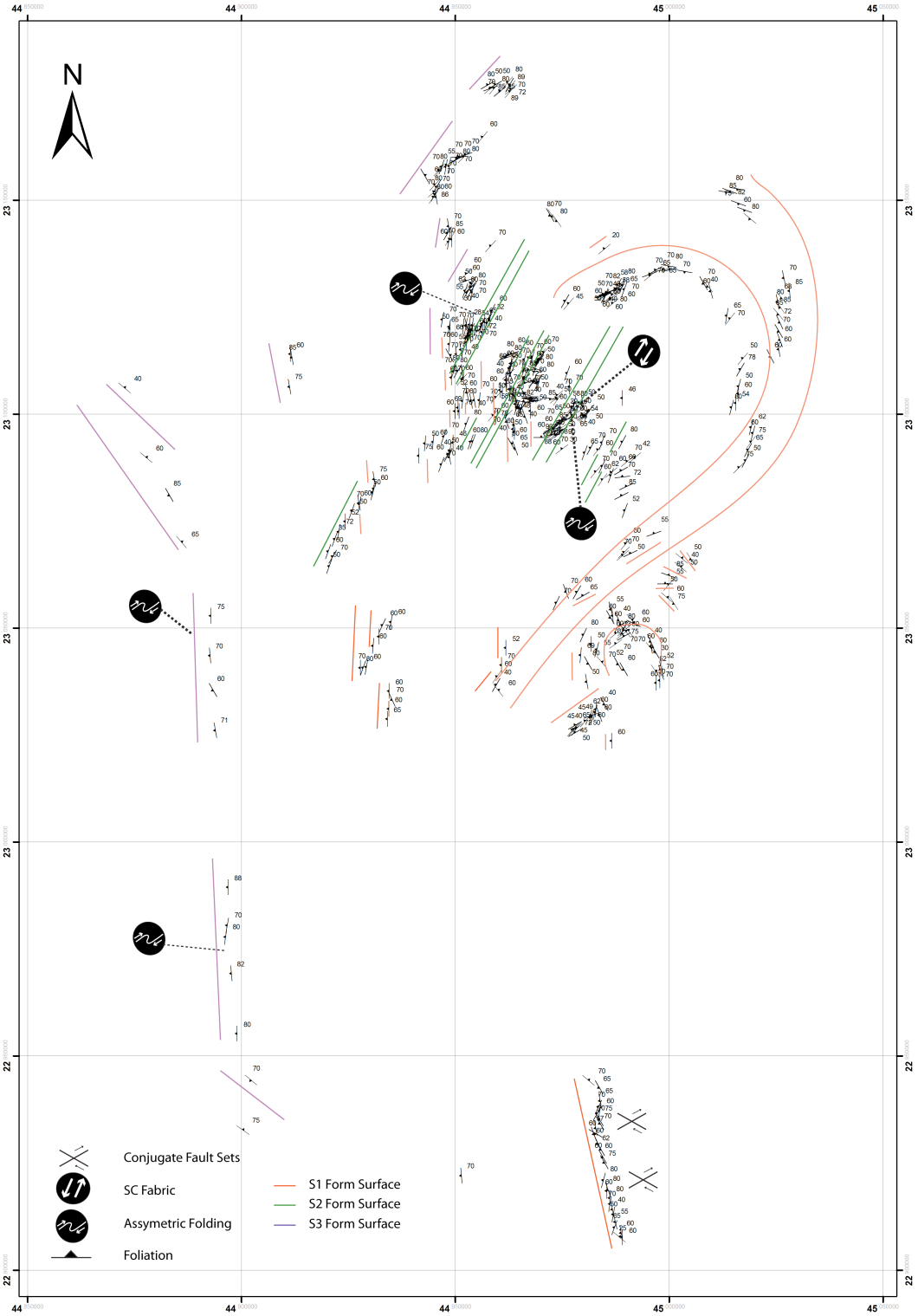

Figure 9. Foliation and form surface map of Jebel Tays reveals 3 deformation fabrics all of which a commensurate with a east-west orientated σ_1 but structural kinematics require differing σ_2 and σ_3 orientations for the D1, D2 and D3 deformation events.

11.1.10 Petrographic images of gabbros and cumulates

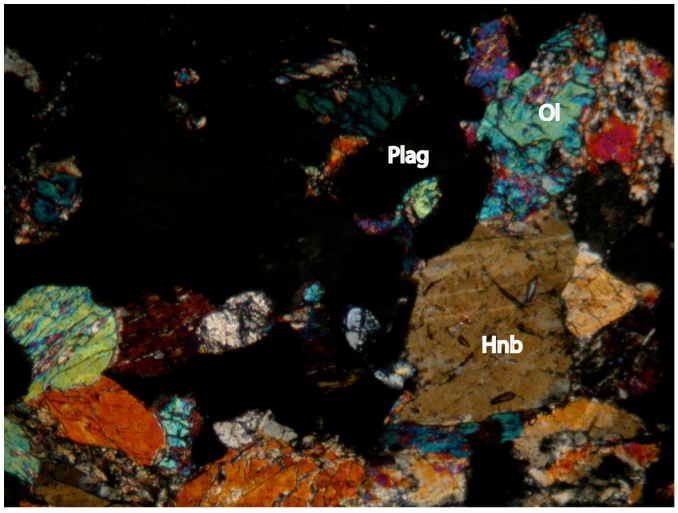

(A) Hornblende gabbro showing fractured olivine, amphibole and highly altered plagioclase.

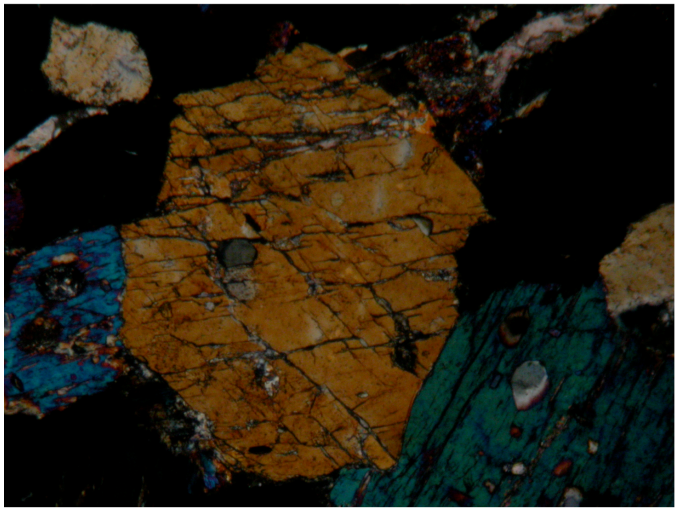

(B) Euhedral hornblende, note the clear 120 cleavage relationship.

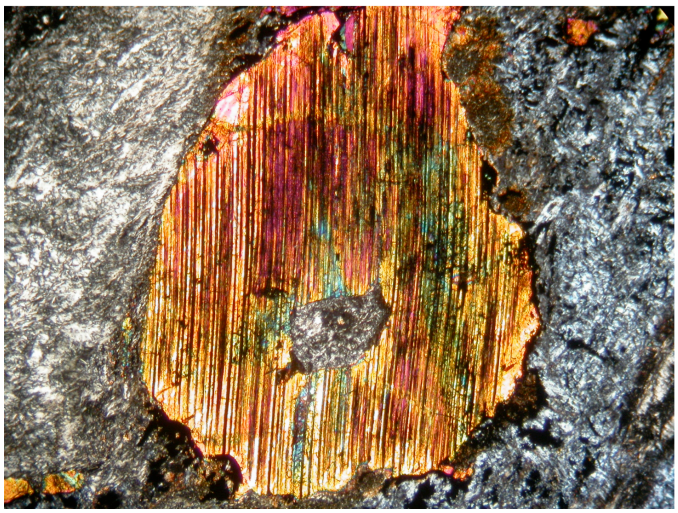

(C) Large CPX grained showing exsolution of OPX and surrounded by serpentinite.

Figure 10. (A) Gabbro showing composition of hornblende, olivine and altered plagioclase. (B) Euhedral hornblende suggesting that amphibole was a primary phase. (C) Ultramafic cumulate composed of CPX and serpentinite.

11.1.11 Harker diagrams for exposed mafic rocks

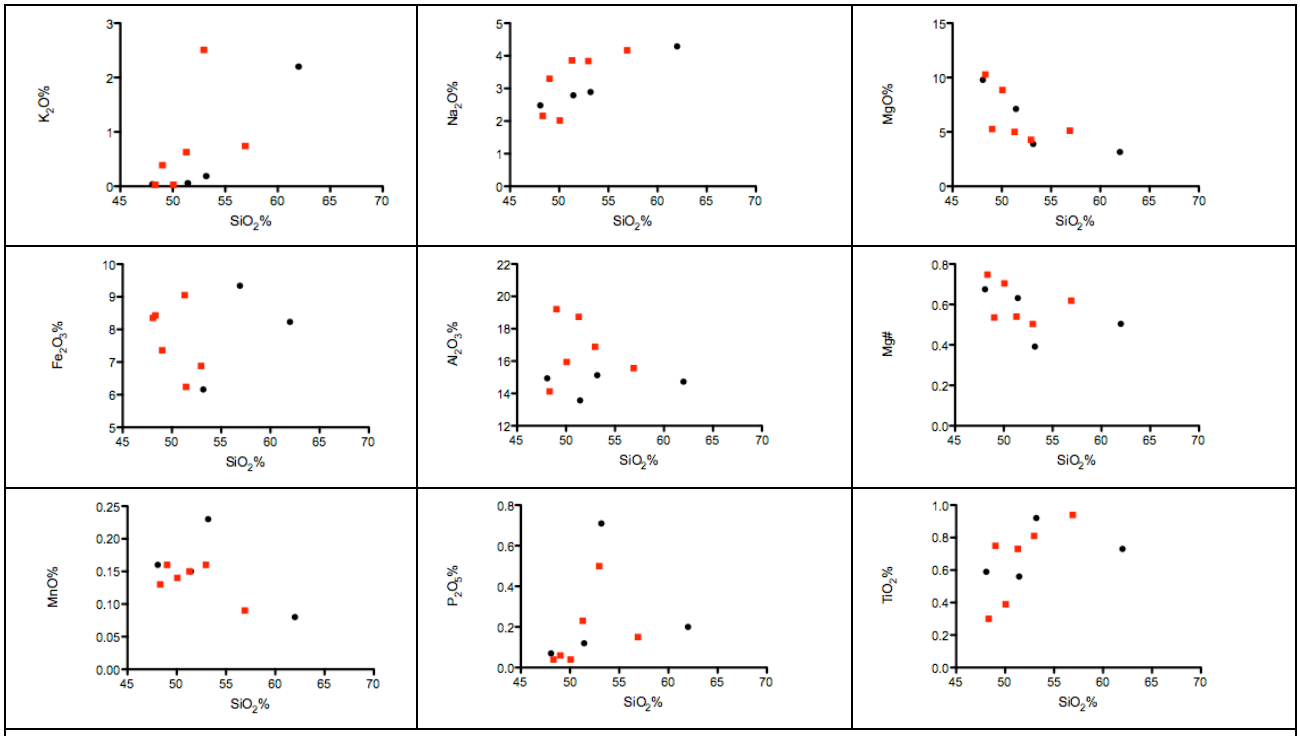

Figure 11A. Harker diagrams of major oxides vs. silica. Red squares are intrusive rocks (gabbros) while black circles are extrusives (basalt and andesite dykes).

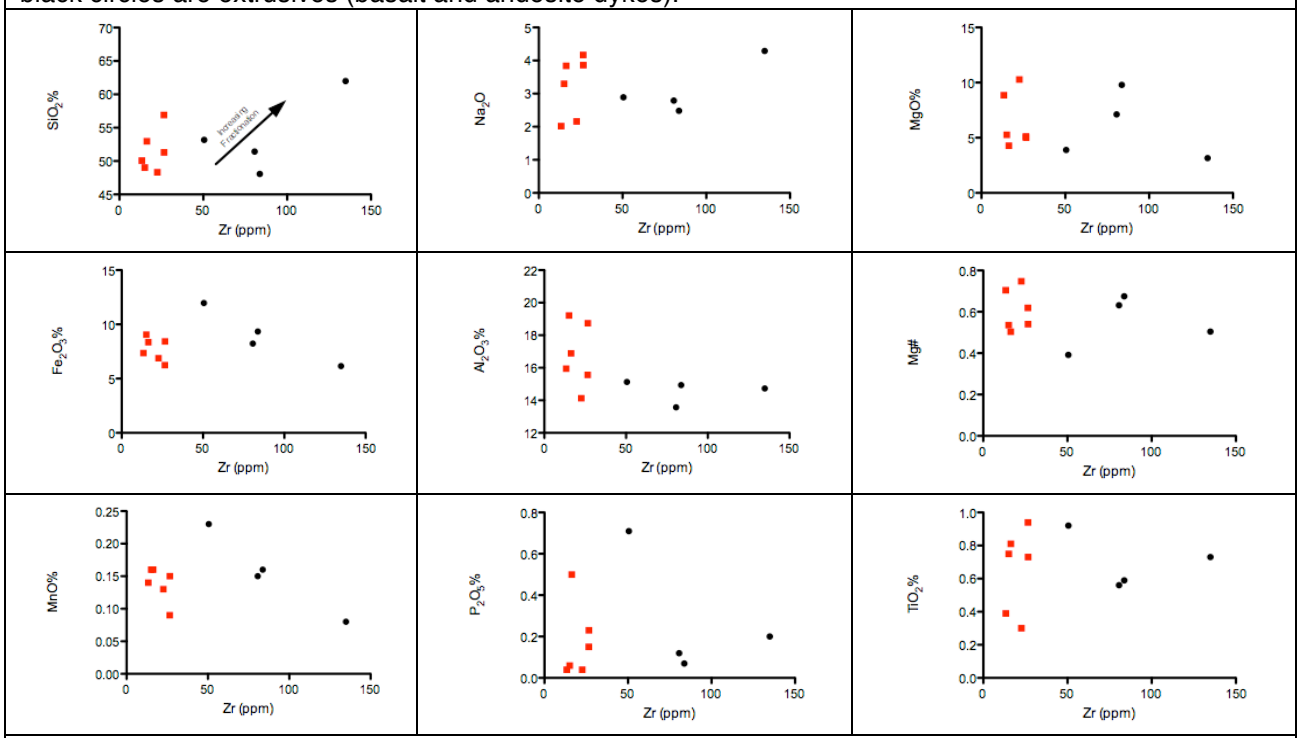

Figure 11B. Harker diagrams of major oxides vs. the relatively immobile Zr. Red squares are gabbros while black circles are mafic and intermediate dykes. Major variation in Zr content occurs only in extrusive rocks suggestive of fractional crystallisation processes.

11.1.12 IUSG classification of gabbroic rocks

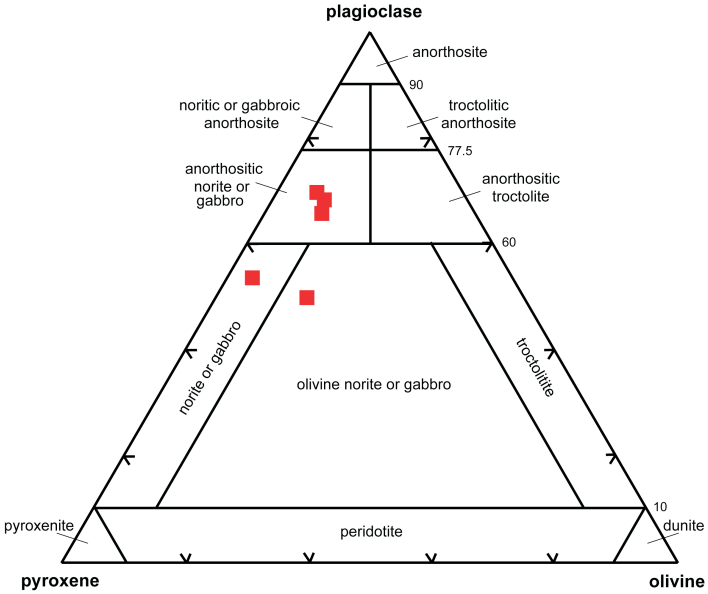

Figure 12. IUGS classification of gabbroic rocks after Streckeisen (1974) based on normative content of olivine, pyroxene, and plagioclase.

11.1.13 Mafic suite trace element spider plots

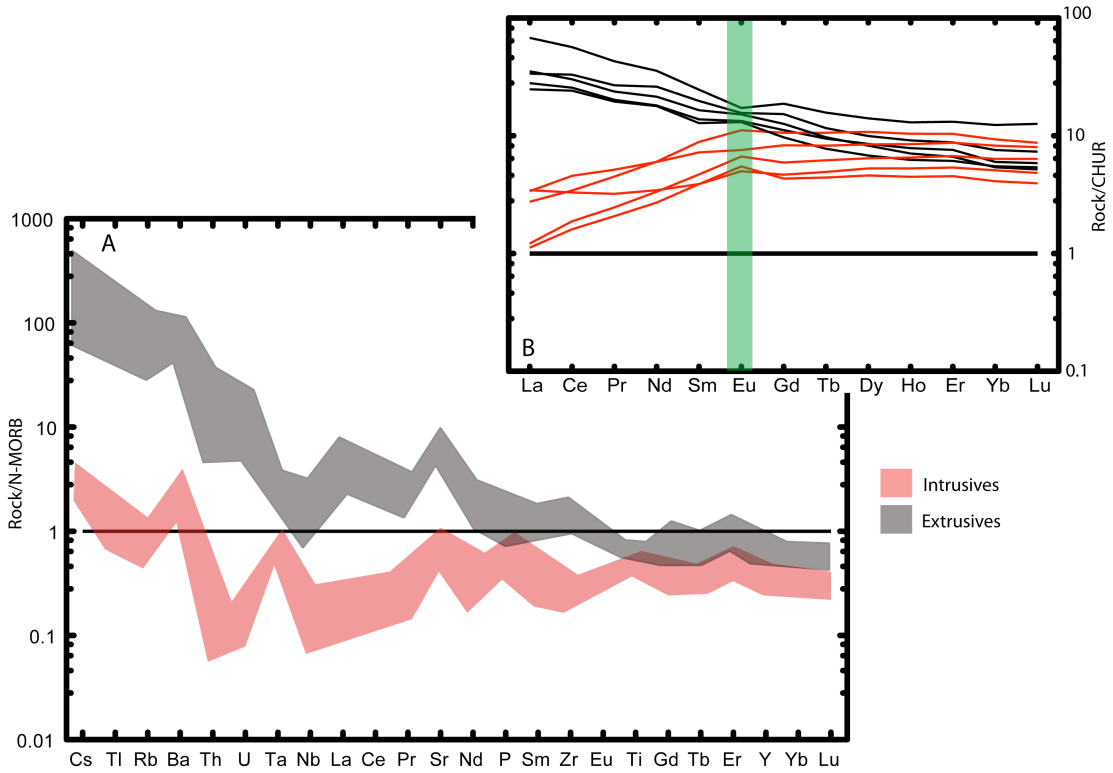

Figure 13. (A) Trace element plot for mafic intrusives (gabbros) (n=5) and extrusives (mafic dykes) (n=5), all rocks show similar HREE abundances and fan towards LILE typical of rocks related by fractional crystallisation. Also notable is the overall depletion shown by the gabbroic intrusives across the entire trace element spectrum. Particularly apparent is the overall positive gradient across the REE spectrum, this is suggestive of a significantly depleted source (B) REE plot for both gabbros and basalts, it is clear that the analysed gabbros do not exhibit any significant Eu anomaly and the associated basalts do not show a significant reciprocal Eu anomaly leading to the interpretation that these gabbros have not been subject to cumulate processes. Also evident is the strong positive gradient from Lu to La in the gabbros, this highly fractionated REE pattern is not the pattern which would be expected for MORB like gabbros or even typical IAT which show negative gradients from Lu to La as expected from their relative incompatibilities. Normalisation values are from Sun & McDonough (1989).

11.1.14 Cr vs. Y plot of chrome spinels

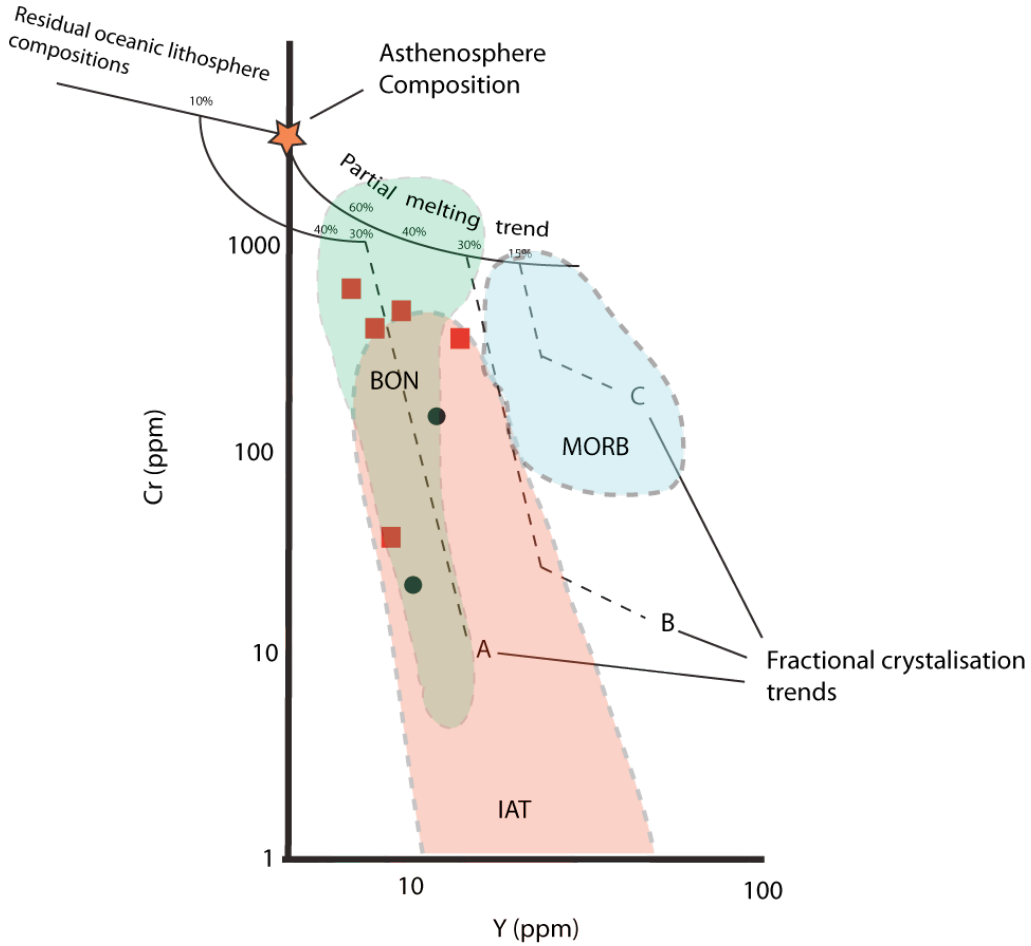

Figure 14. Cr vs. Y showing the fields of IAT, boninites and MORB. Composition field for MORB and IAT from Pearce *et al.* (1984b) while the field of Boninites is from the Petrological Database of the Ocean Floor, http://www.petdb.org (Lehnert et al., 2000). Red squares are mafic intrusives (gabbros) while black circles are basaltic dykes. All rocks bar one plot within the field of IAT/boninites and follow a boninitic fractionation trend.

11.1.15 MORB array plots of mafic rocks

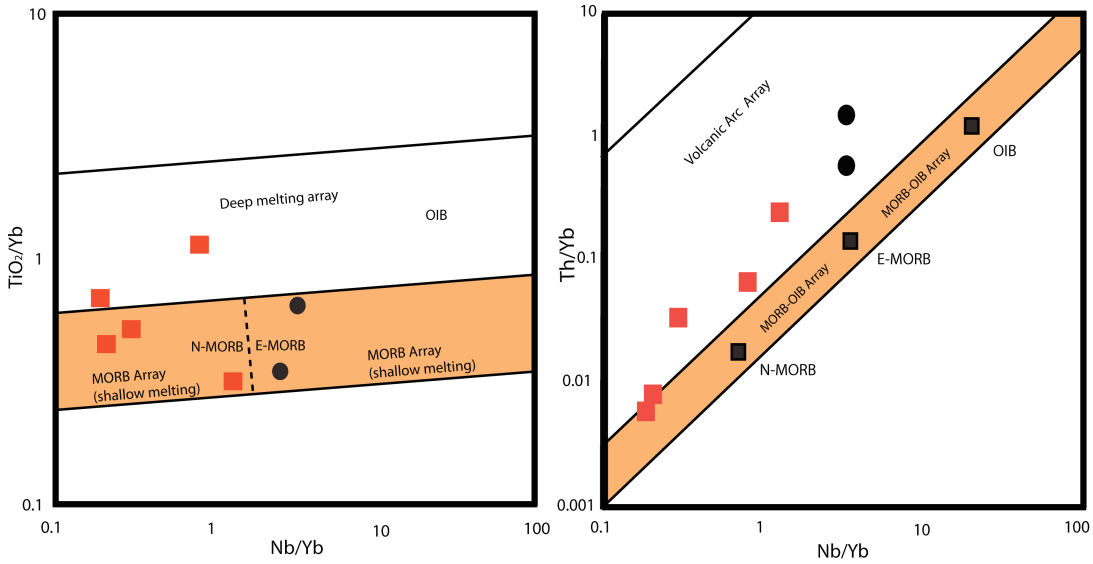

Figure 15. TiO_2/Yb vs. Nb/Yb melting depth proxy indicates that most samples are derived from depths similar to that of mid ocean ridge settings. Th/Yb vs. Nb/Yb reveals that most samples plot within the volcanic arc array indicative of continental input to the magma. Plots are from Pearce (2008)

11.1.16 Element maps of chrome spinels

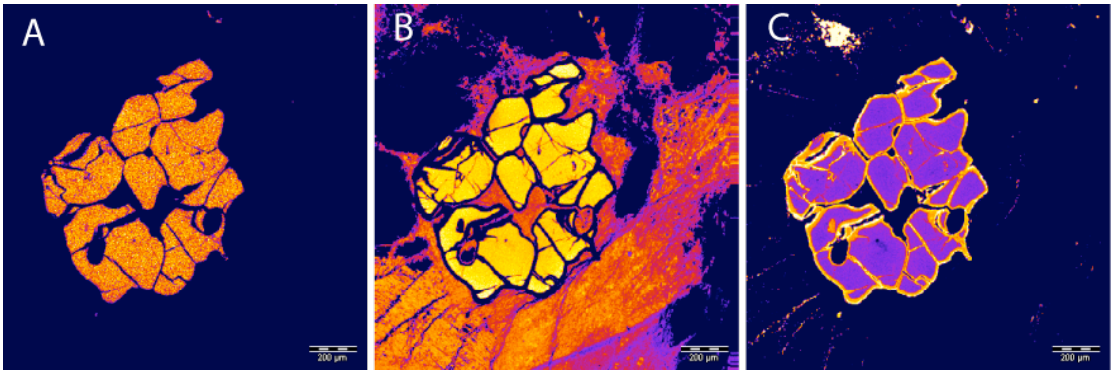

Figure 16. (A) Mg map of spinel showing that Mg has a relatively uniform distribution throughout the grain. (B) Al map showing marked decrease in Al content at the grain boundary. (C) Shows a commensurate increase in Fe content at grain boundaries.

11.1.17 Cr# vs. Mg# of chrome spinels

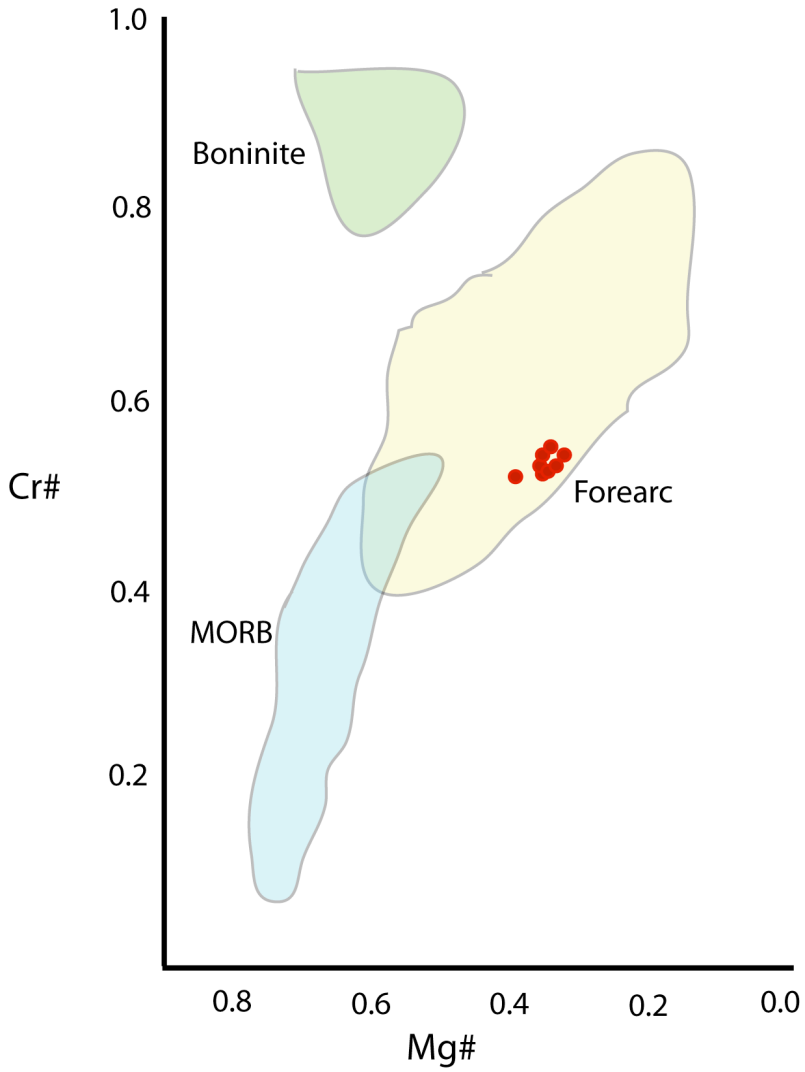

Figure 17. Cr# vs. Mg# discrimination plot (Azer and Stern, 2007) showing that unaltered spinel cores plot within the field of forearc peridotites.

11.1.18 Al vs. Ca of serpentinised peridotite

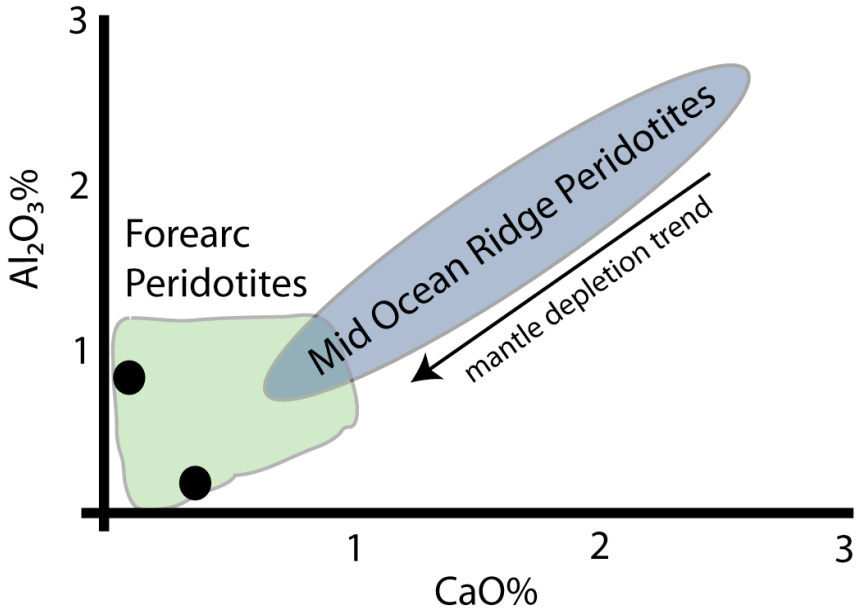

Figure 18. Tectonic discrimination of serpentinised peridotite after Azer & Stern (2007). These mantle sequence rocks map into the field of forearc peridotites indicative of a refractory mantle sequence. The basis for this discrimination is the same as that for chrome spinels, such low Al_2O_3 and CaO requires partial melting to the exhaustion of diopside (Dick and Bullen, 1984).

11.1.19 Epsilon Nd vs. Age plot of gabbros

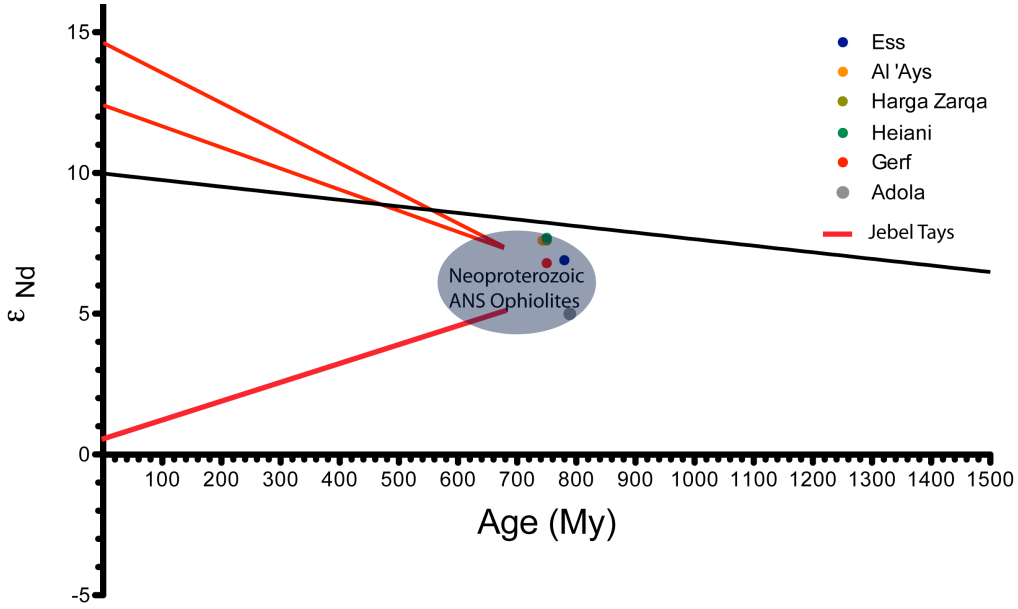

Figure 19. ε_{Nd} values and model ages for two gabbro samples from Jebel Tays as well as isotopic data from other ANS ophiolites which also plot within the same $\varepsilon_{Nd(T)}$ range, indicating that the mantle underlying much of the ANS was very depleted at this time. Data for other ANS ophiolites is sourced from Zimmer *et al.* (1995), Claesson *et al.* (1984) and Worku (1996). Depleted mantle model curve from Goldstein *et al.* (1984)

11.1.20 Comparison of Jebel Tays gabbros with those of Betts Cove

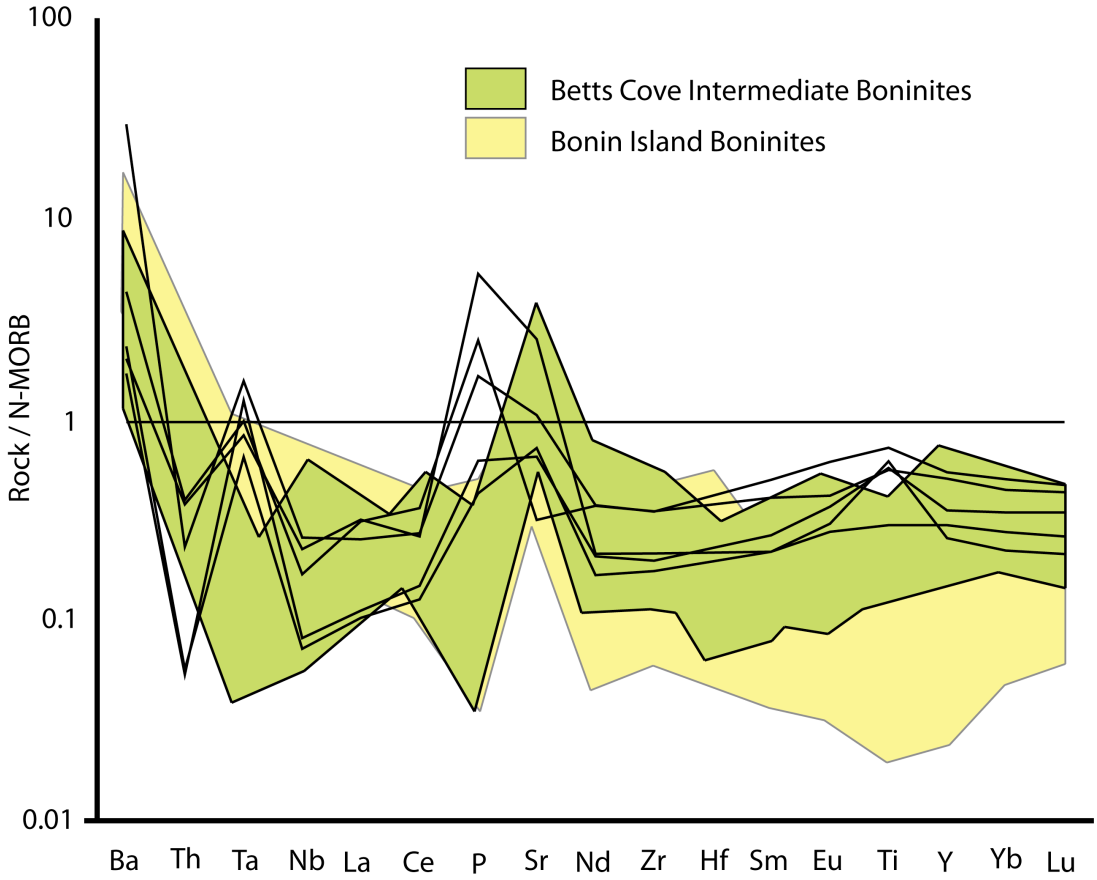

Figure 20. Trace element spider plot showing the close similarity between Jebel Tays gabbros and the intermediate Ti boninites of the Betts Cove ophiolite (Bedard et al., 1998). The U-shaped trace element pattern that is generally prominent in boninites is still evident in these intermediate Ti boninites. LILE/LREE enrichment is a function of the nature of the fluxing fluid and thus not a definitive characteristic of boninites, this is unlike REE fractionation which is a pre-requisite as it is a function of the refractory nature of the source rocks. Normalisation values are from Sun & McDonough (1989).

11.1.21 Petrographic images of the exposed trondhjemite

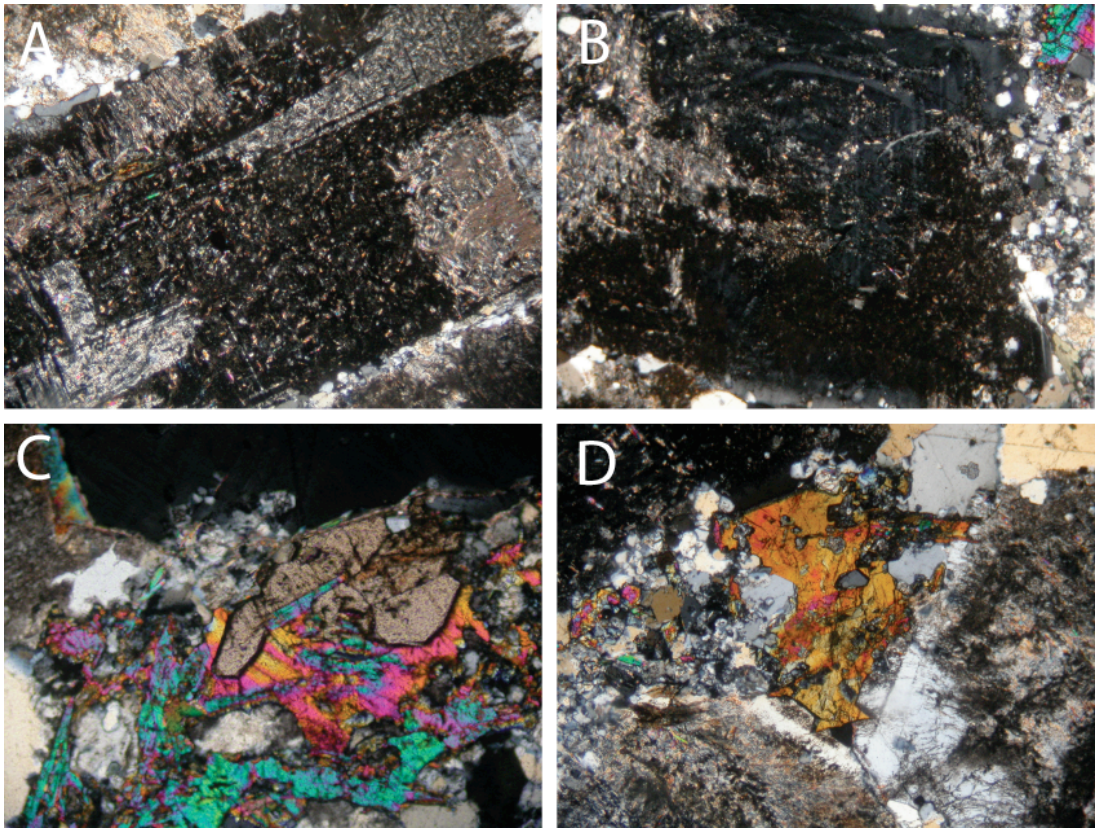

Figure 21. (A) & (B): Relic oscillatory zoning and multiple twinning in saussuritized plagioclase, speckles within plagioclase are muscovite and maybe epidote or zoisite. (C) Euhedral titanite as inclusions within epidote. (D) Sub-euhedral epidote.

11.1.22 Trondhjemite major element geochemical plots

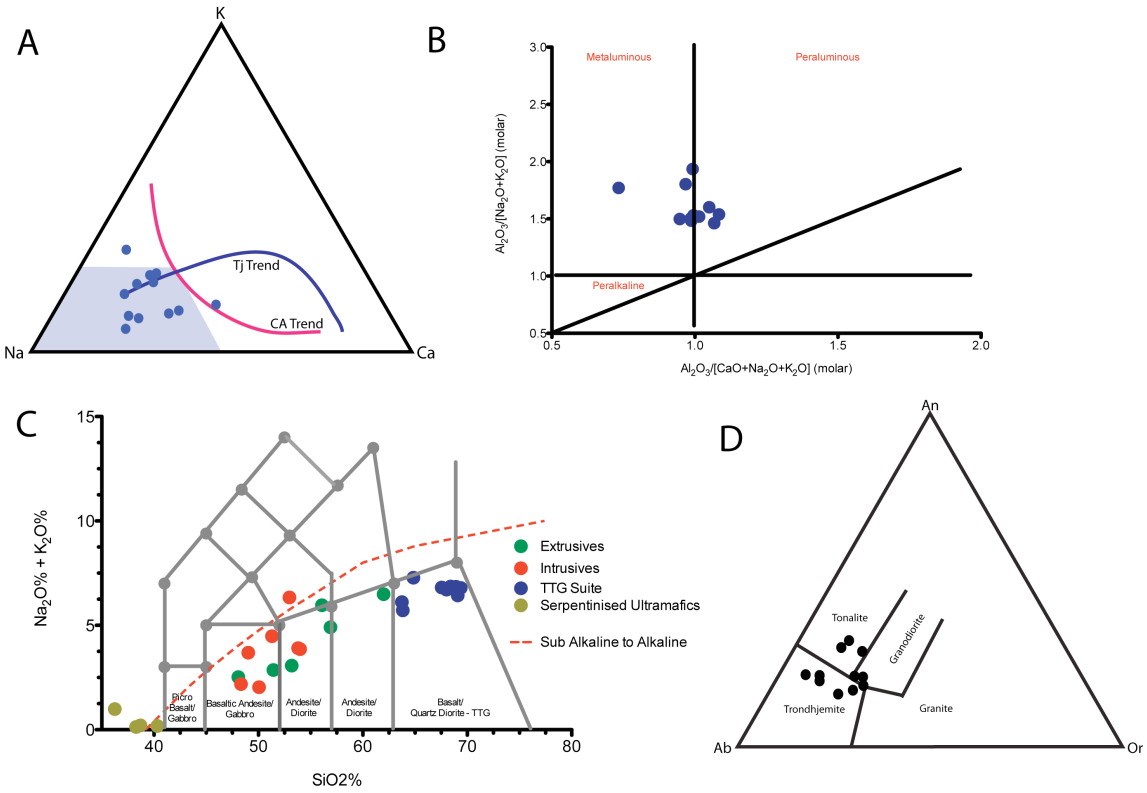

Figure 22. (A) K-NA-Ca ternary diagram revealing that these trondhjemitic rocks do not follow the typical calc-alkaline trend of increasing K content with increasing Na. (B) Shands index for TTG rocks indicating that while they are slightly peraluminous these rocks plot within the field of fractionated I-type melts. (C) TTG rocks display sub alkaline to alkaline characteristics and plot as quartz diorites of Le Maitre (1989). (D) Normative compositions of Barker (1979) revealing the overall trondhjemitic character of these rocks.

11.1.23 Trondhjemite trace element spider plot

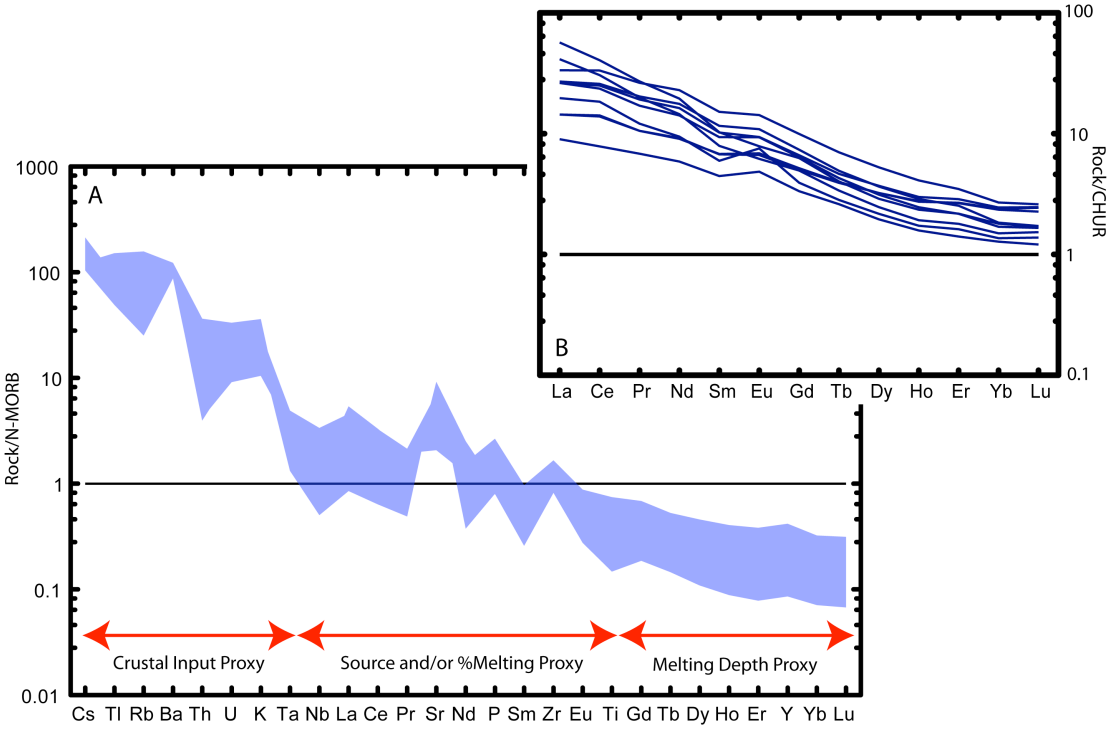

Figure 23. Trace element spider plot for TTG rocks (n=8), Nb anomaly suggests volcanic arc affinity while the generally flat pattern from La to Eu is a MORB like signature indicative of either significant melting of MORB or small percentage melting of a source more depleted than MORB. Ti through to Lu shows marked depletion and the relatively steep gradient indicates significant fractionation of HREE suggestive of melting at depths where amphibole or garnet are stable residual phases. Normalisation values are from Sun & McDonough (1989).

11.1.24 Trondhjemite discriminant diagrams

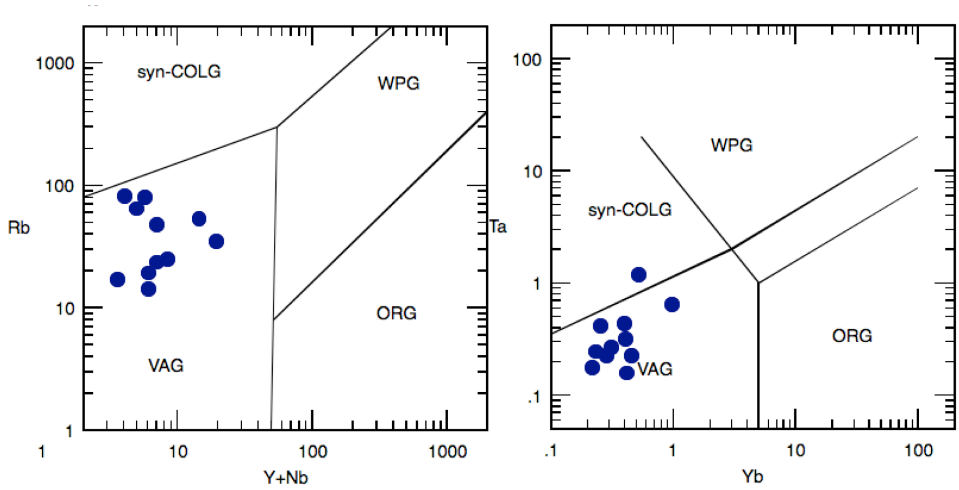

Figure 24. WPG: Within plate granites, syn-COLG: Syn-collisional granites, VAG: Volcanic arc granites, ORG: Ocean ridge granites “plagiogranites”. As is evident from both discriminant plots these trondhjemites plot within the field of volcanic arc granites and strongly negates a plagiogranite genesis. Plots from Pearce *et al*. (1984a)

11.1.25 Adakite discriminant diagrams

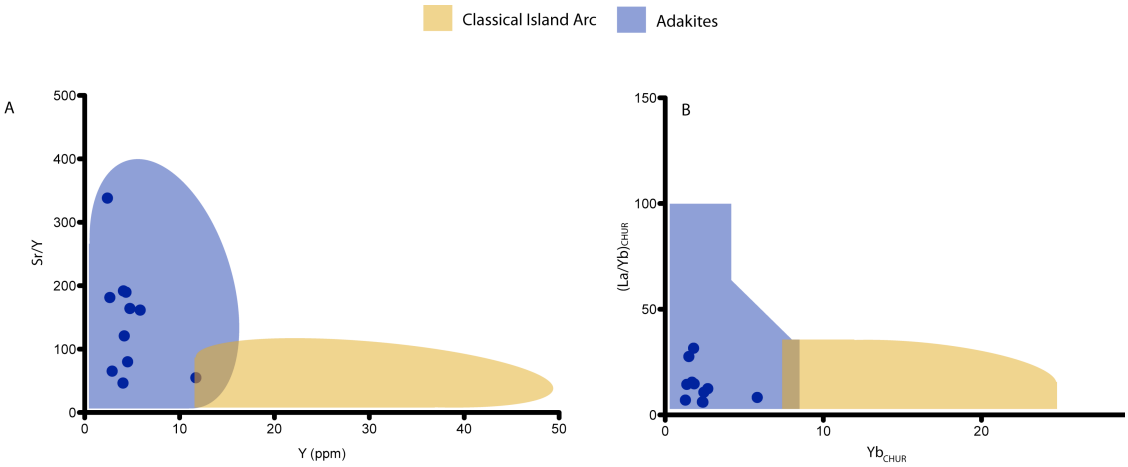

Figure 25. The key geochemical discriminant for adakites are Sr/Y vs. Y (Martin 1999) and La/Yb vs. Yb (Defant and Drummond 1990), these separate adakites from other volcanic arc magmas. The basis of these trace element discriminant diagrams are high Sr/Y ratios which reflect low Y concentration suggestive of melting at depth and a lack of plagioclase fractionation which separates them from volcanic arc dacites. La/Yb ratios are again melting depth proxies.

11.1.26 Qualitative temperature vs. Mg# plot for a cooling adakite melt

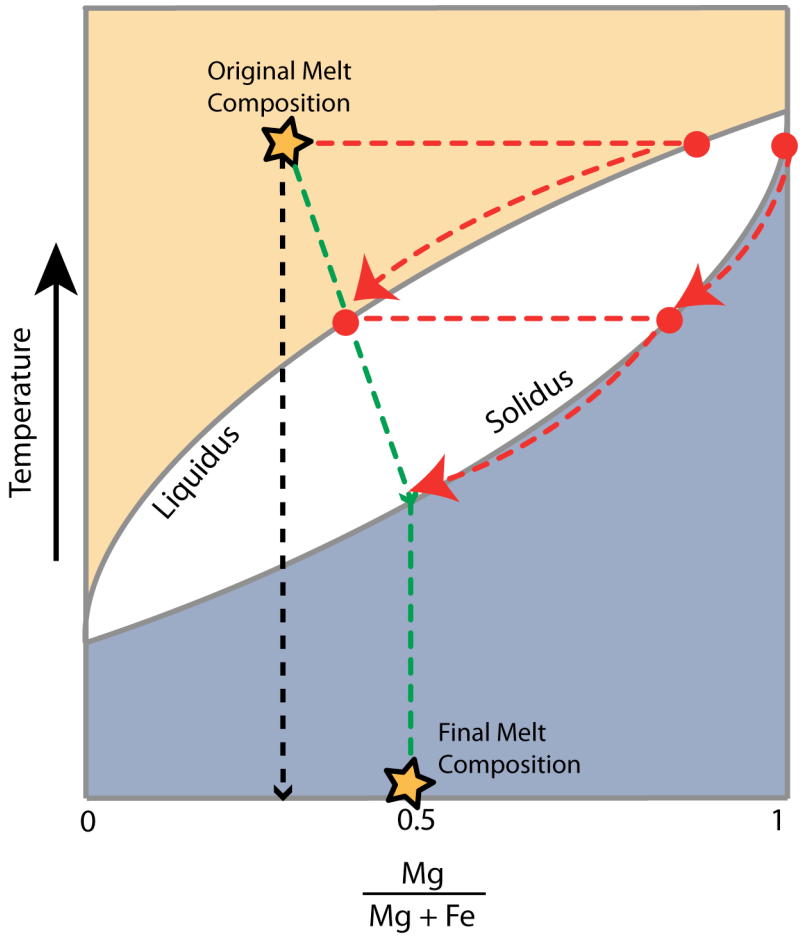

Figure 26. Qualitative temperature vs. Mg# diagram for olivine showing how a cooling felsic melt interacts with peridotite, the resulting mantle liquid derived is of high Mg#, such liquid is incorporated into the buoyant felsic melt resulting in the melt following the green cooling path, such interaction ceases once the felsic melt has cooled below the solidus for peridotite phases such as olivine (Foden *pers comm.,* 2009).

11.1.27 Serpentinite/carbonate mesh texture

Figure 27. (A) Mesh texture of serpentinised cumulate rock from Jebel Tays. (B) & (C) carbonate rocks displaying relic mesh texture from serpentinite protolith.

11.1.28 Images of carbonate morphologies

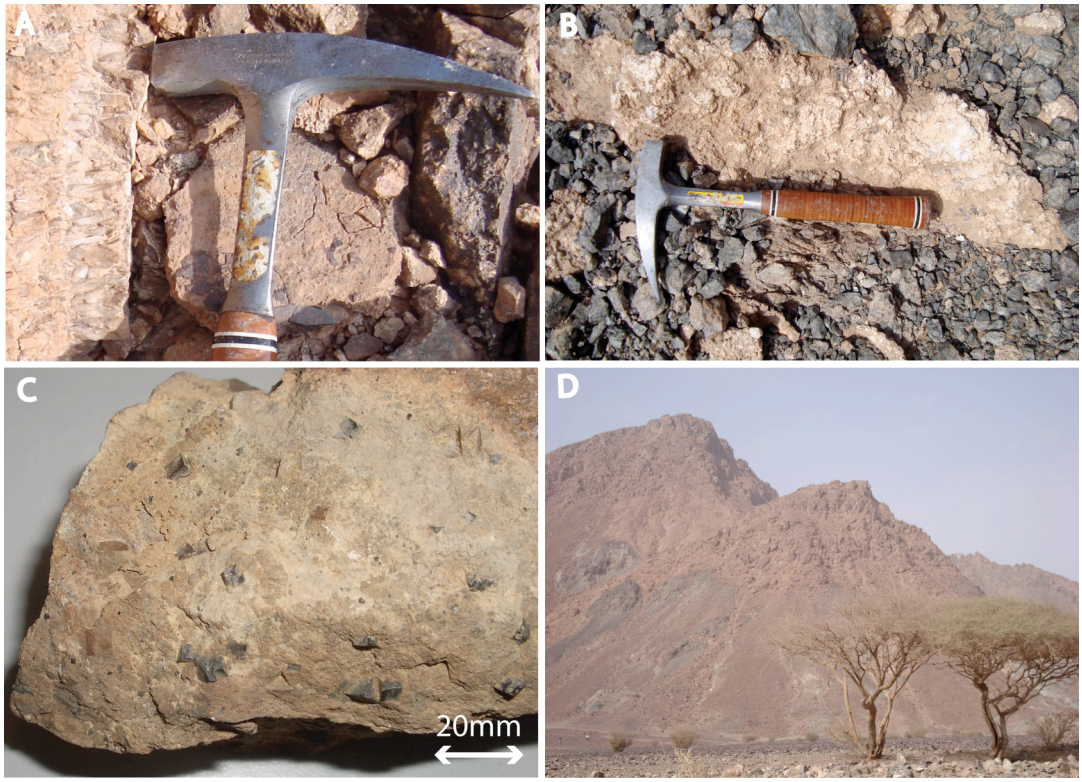

Figure 28. (A) Coarse crystalline carbonate vein cross cutting massive carbonates, these veins display sub-euhedral to euhedral carbonate crystals and have $\delta^{13}C > 12$ per mil. (B) Cauliflower carbonate that forms exclusively within serpentinite mélange. (C) Massive carbonate containing euhedral pseudomorphed pyrite. (D) Massive resistant carbonate ridges exposed on the eastern side of Jebel Tays, the dark patches are the underlying serpentinite.

11.1.29 CL images of Abt detrital zircons

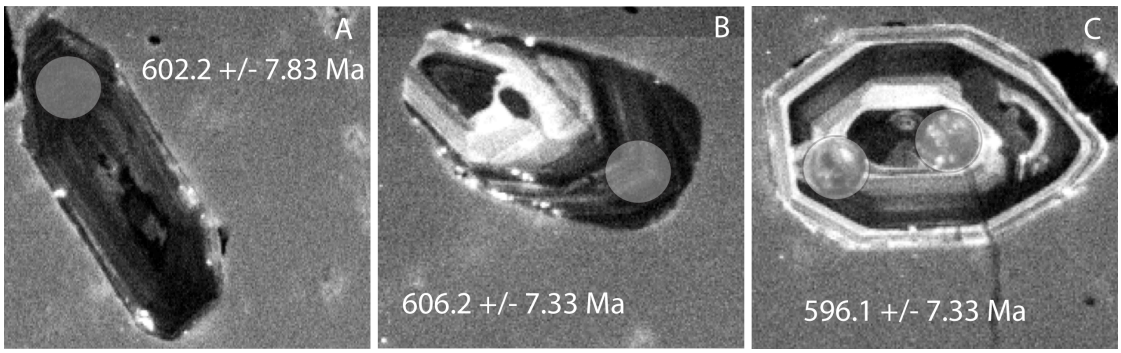

Figure 29. CL images of the three youngest zircons suggest a minimum depositional age of ca 600 Ma. These zircons show distinct oscillatory zoning and euhedral shape typical of igneous derived zircons. Spot sizes are 30 μm.

11.1.30 Concordia and probability density plot for Abt Fm sample

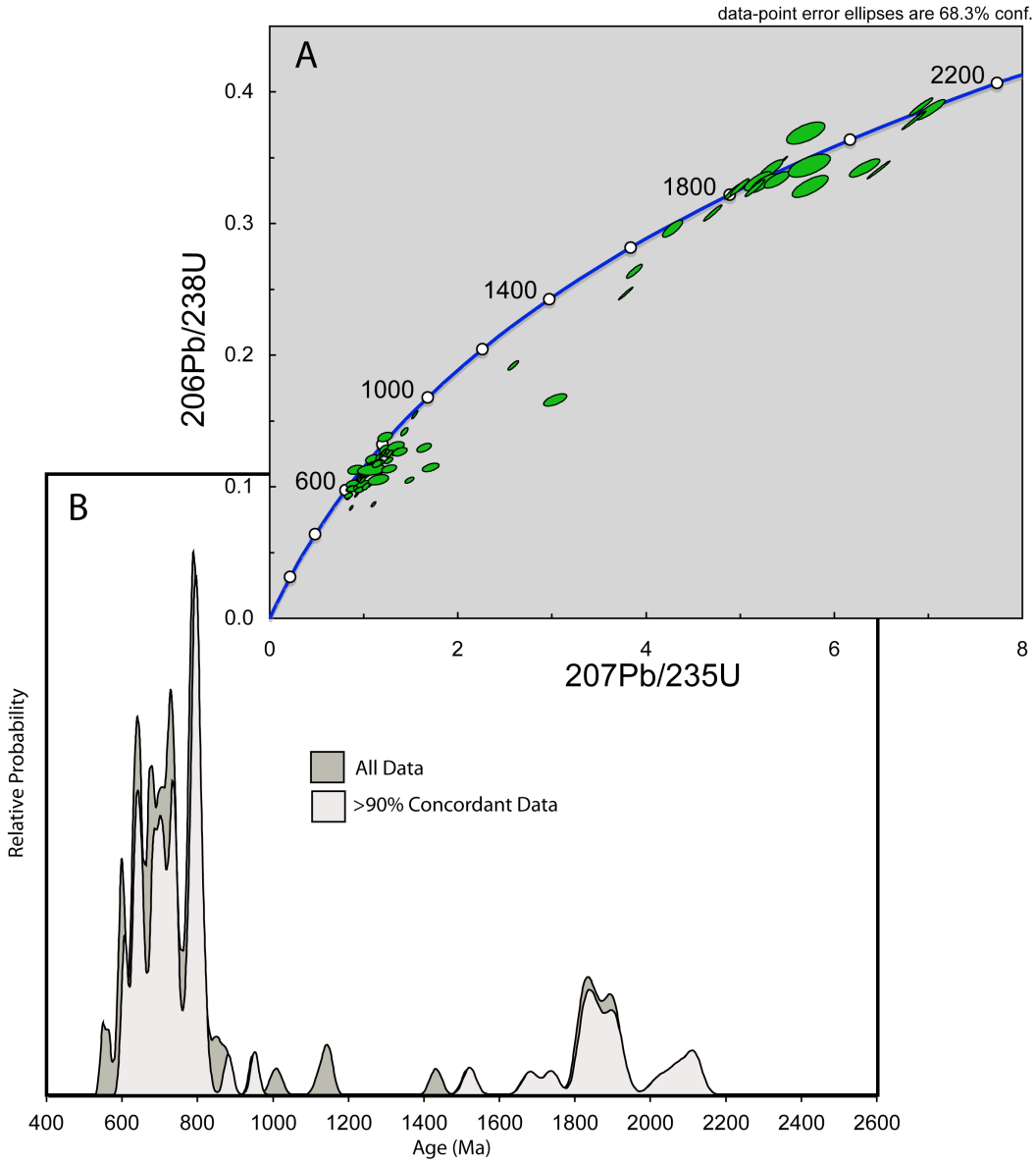

Figure 30. (A) Concordia plot of 92 analysed zircons from a pebbly conglomerate from the Abt revealing Neoproterozoic and Paleoproterozoic populations. (B) Probability density plot of detrital zircons, youngest grain was dated at 596.1 ± 7.33 Ma and was 97% concordant. Possible source rocks for these zircon populations can be found in the adjacent Afif and Ar Rayn Terranes (Fig. 32).

11.1.31 Concordia plot for Abt cobble clast

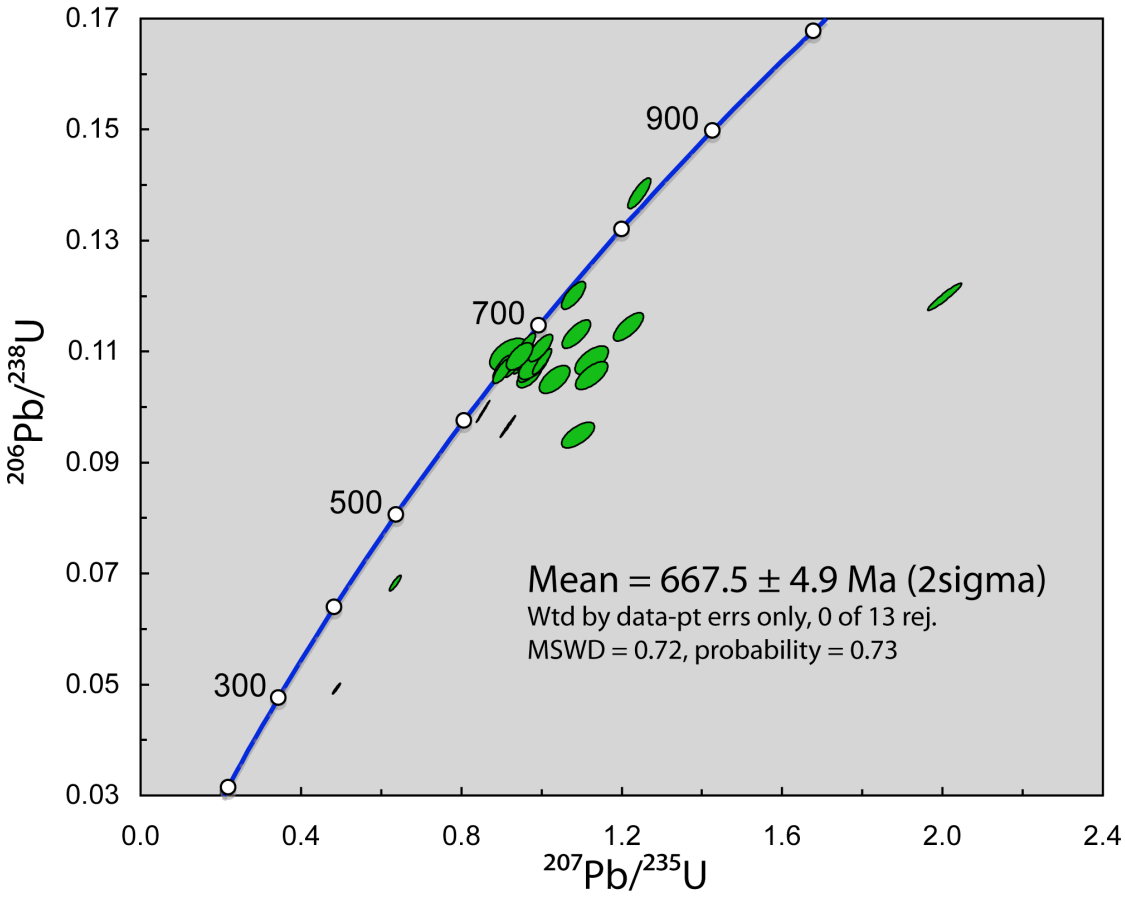

Figure 31. U-Pb concordia for all zircons from a sub-volcanic cobble clast obtained from the Abt immediately east of Jebel Tays. A mean $^{206}Pb/^{238}U$ calculated age of 657 ± 12 Ma was obtained based on 18 concordant (>90%) zircons out of a total of 29. A further refined age based on those zircons with >95% concordancy (n=13) produced a $^{206}Pb/^{238}U$ age of 667.5 ± 4.9 with MSWD of 0.72 which is interpreted as the crystallisation age for this cobble clast.

11.1.32 Arabian Nubian Shield age spectrum map

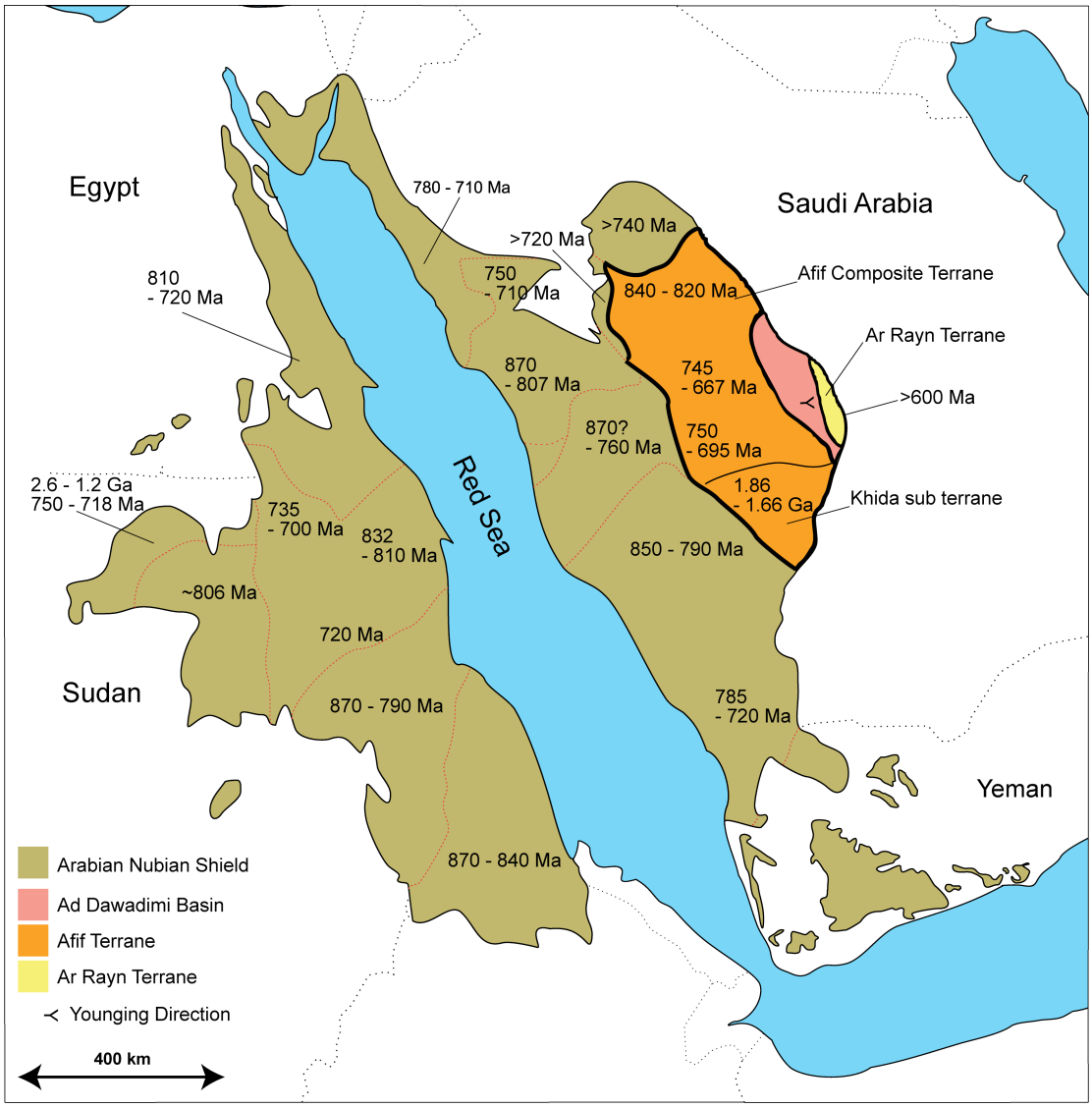

Figure 32. Terrane map of the ANS showing the spectrum of crystallisation ages for exposed basement rocks. The age spectrum of detrital zircons is consistent with derivation from the Afif or Ar Rayn Terranes. The Paleoproterozoic ages most likely come from the Khida (Afif) Terrane.

11.1.33 Concordia plot for Jebel Tays gabbro

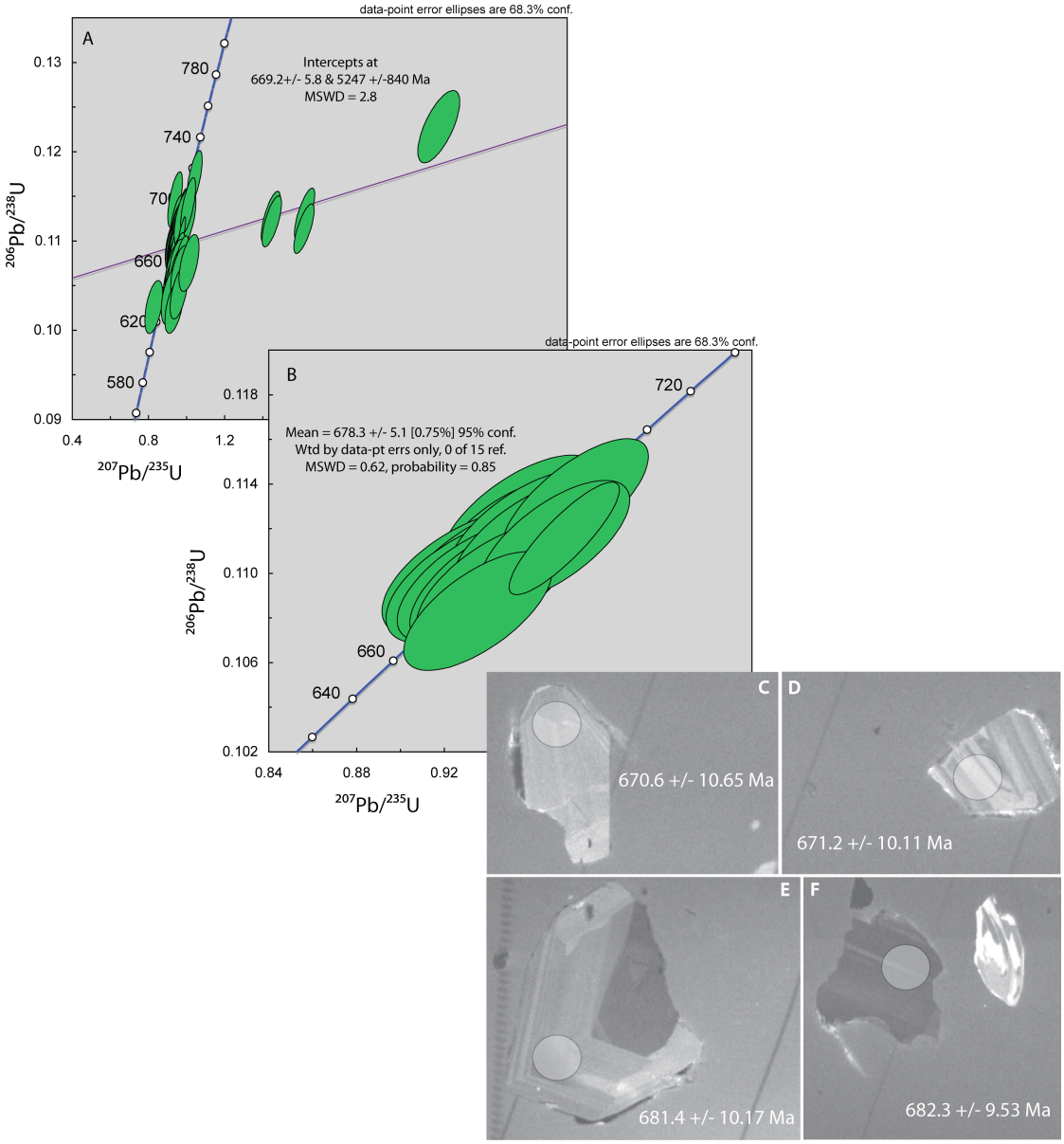

Figure 33. (A) Concordia of all 45 analysed zircons revealing both lead loss, inheritance and a common lead trend. (B) Concordia of those zircons which displayed better than 95% concordancy (n=15) and all produced ages within error of each other. These produced a mean $^{206}Pb/^{238}U$ of 678 ± 5.1 Ma (2σ) with a MSWD of 0.62 suggestive of a single zircon population. (C) Representative CL images of analysed zircons, shaded spot marks the position of the ablation spot, spot size was 30 μm. Individual dates are based on $^{206}Pb/^{238}U$ ages and where better than 95% concordant.

11.1.34 Concordia plot for Jebel Tays trondhjemite

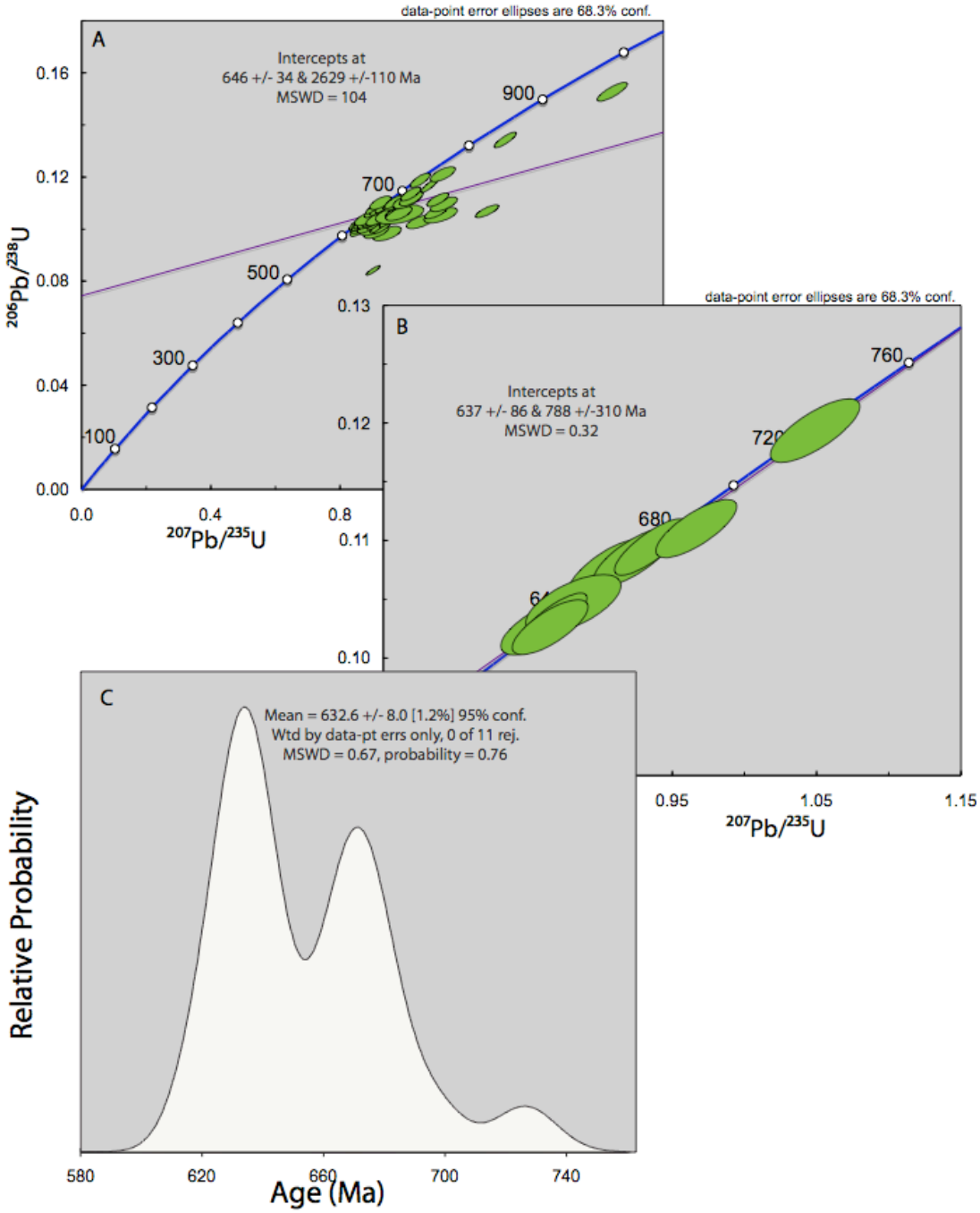

Figure 34. (A) Concordia diagram of all analysed zircons showing inheritance, lead loss and common lead (B) Concordia diagram of those zircons that were greater than 95% concordant, visually 3 distinct age populations are apparent. (C) Probability distribution plot provides statistical evidence for 3 distinct age populations. All mean ages shown are $^{206}Pb/^{238}U$.

11.1.35 CL images of inherited Archaean zircons

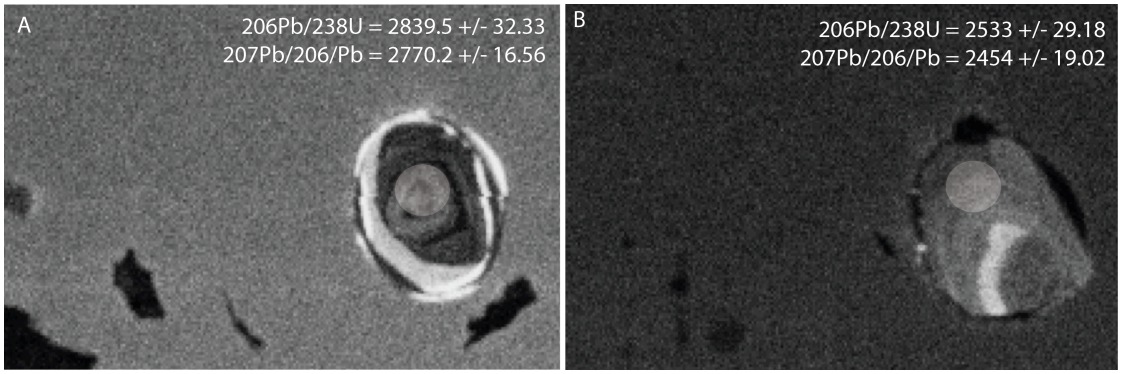

Figure 35. (A) Mesoarchaean zircon grain, analysis is from the low CL response oscillatory-zoned core. Spot size is 30 μm. (B) Neoarchaean zircon, analysis from oscillatory zoned rim, again a 30 μm spot size.

11.1.36 CL images of youngest trondhjemite zircons

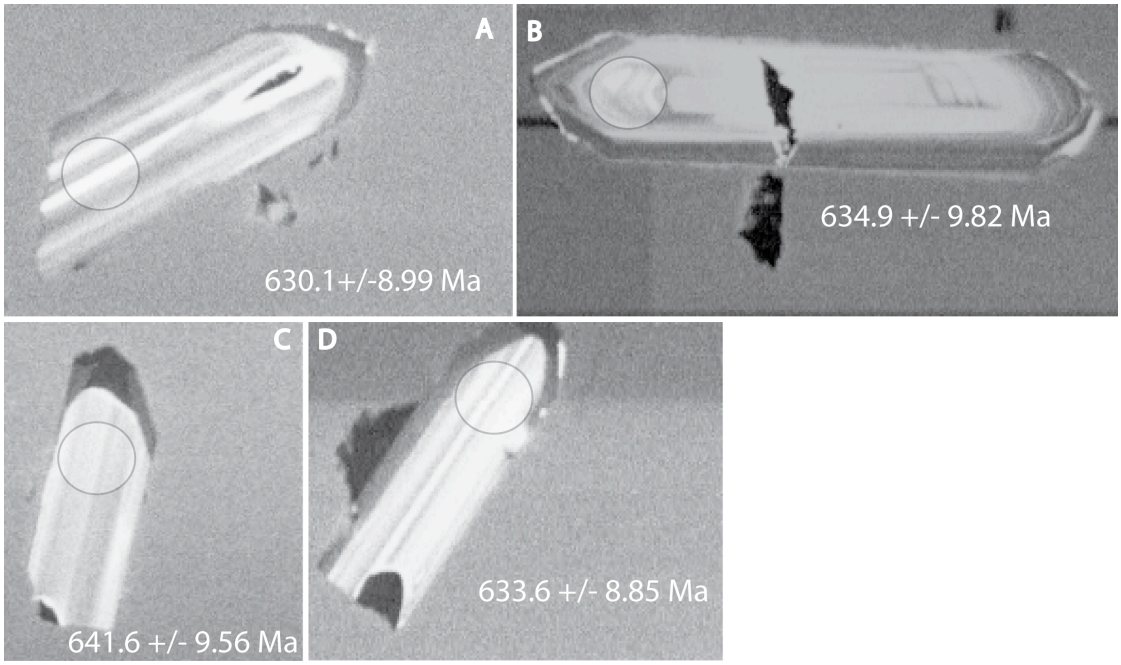

Figure 36. CL images of zircons obtained from a Jebel Tays trondhjemite sample, note the elongated euhedral morphology, strong CL response and igneous oscillatory zoning. Shaded circles mark the laser ablation spots, spots are 30 μm in diameter. Individual spot ages are $^{206}Pb/^{238}U$ and where better than 95% concordant.

11.1.37 Concordia plot of trondhjemite metamorphic monazites

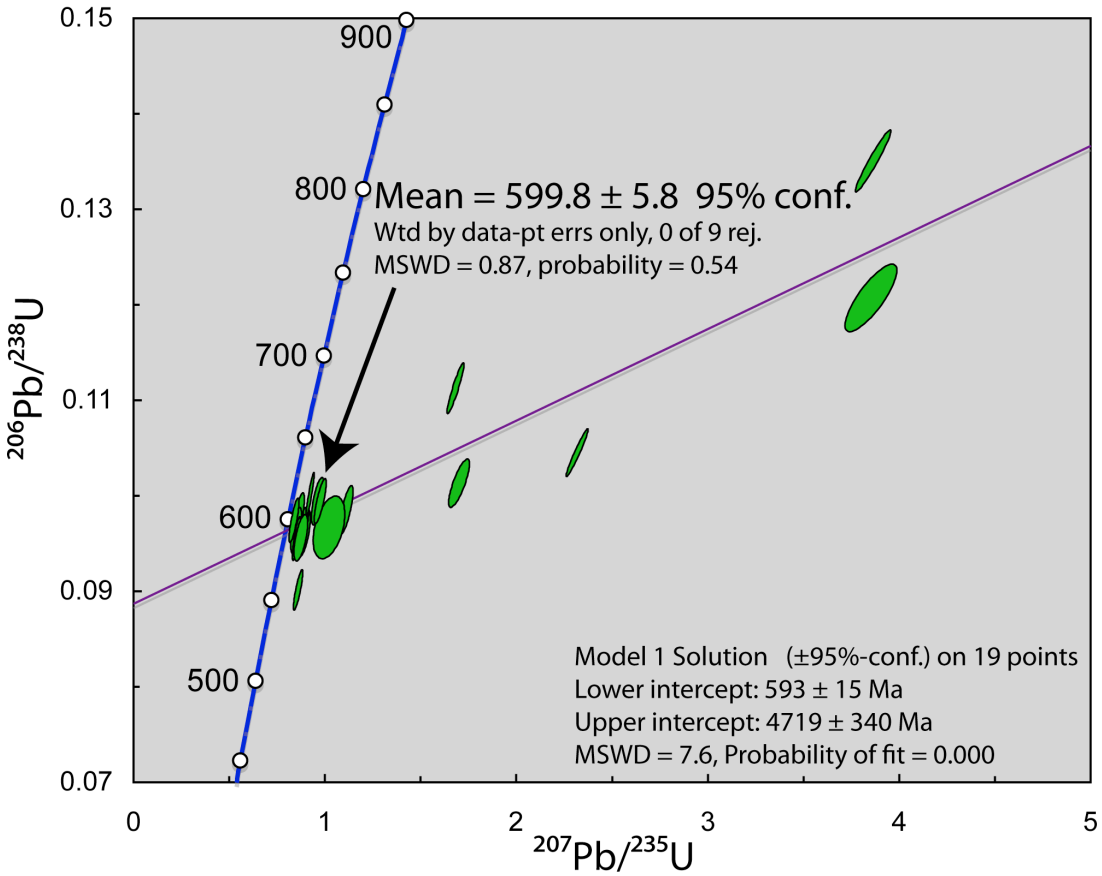

Figure 37. U-Pb concordia of analysed monazites from TTG type granitoid showing tight grouping of near concordant dates along with some showing characteristic common lead. Calculated mean ages are $^{206}Pb/^{238}U$.

11.1.38 Concordia plot for the Halaban diorite

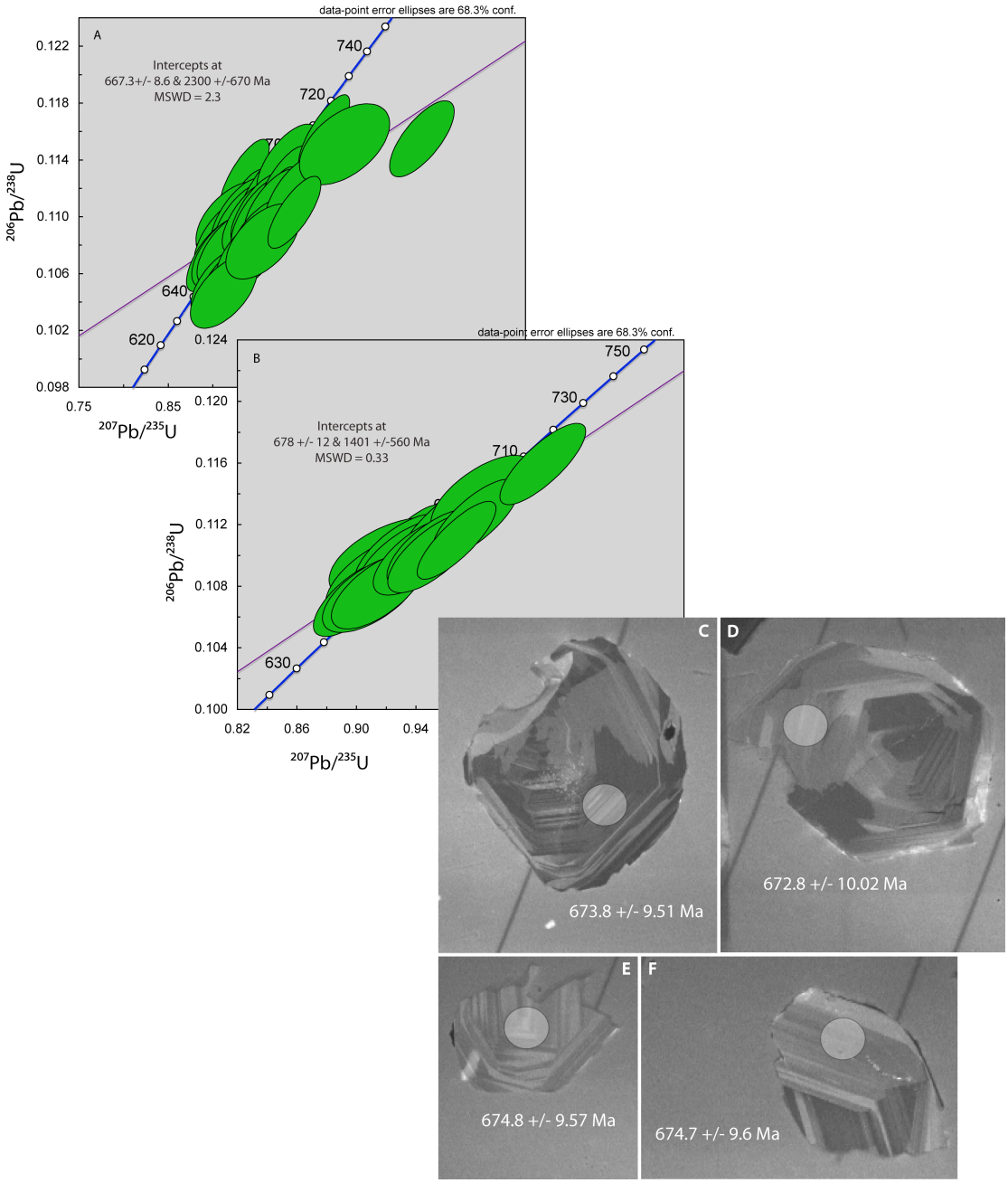

Figure 38. (A) Concordia of all analysed zircons showing considerable spread in the age data. (B) Reduction of age data to only those zircons that were better than 95% concordant still reveals multiple zircon populations. (C) CL images of the youngest zircons showing complex oscillatory zoning and euhedral morphology, individual ages are $^{206}Pb/^{238}U$. Utilising the youngest 9 zircons that lie within error of each other produced a mean weighted $^{206}Pb/^{238}/U$ age of 674.4 ± 5.8 Ma with a MSWD of 0.53 statistically suggestive of a single zircon population

11.1.39 Age compilation diagram for the eastern ANS

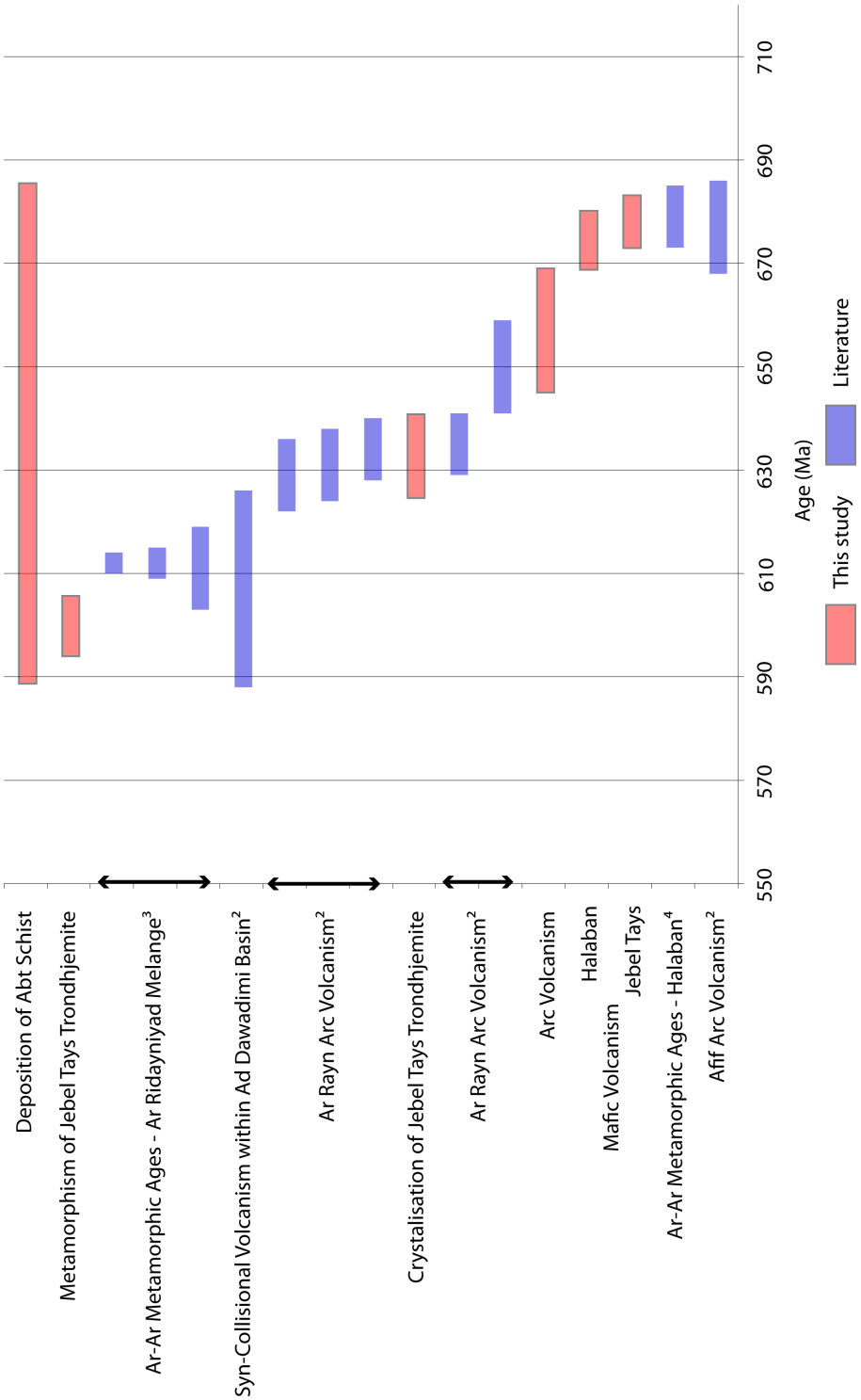

Figure 39. Geochronological framework for the Ad Dawadimi basin and the adjacent arc terranes of the Afif and Ar Rayn. Dates are from: (1) This study (2) Stacey et al. (1984) (3) Al-Saleh & Boyle (2001b) (4) Al-Saleh et al. (1998).

11.1.40 Images of classic serpentinite mud volcanism

Figure 40. (A) & (B) Fine serpentinite mud mélange interpreted to represent serpentinite mud volcanism. (C) Enlarged picture of (A) showing entrained angular mafic clasts in highly sheared serpentinite mud. (D) Larger cobbles to boulders that have been entrained within the serpentinite mud.

11.1.41 Schematic model of Jebel Tays obduction mechanism

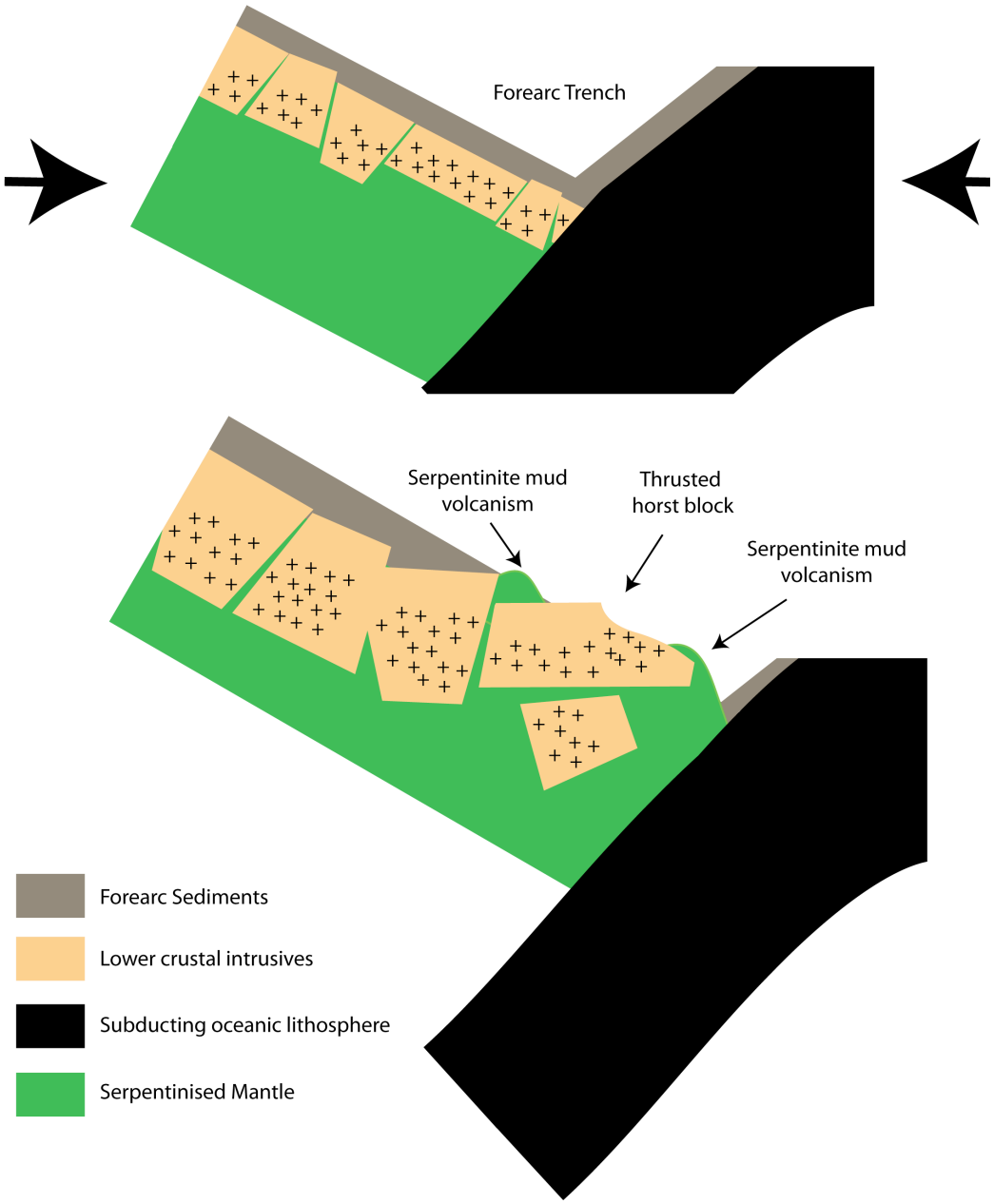

Figure 41. Serpentinite volcanism model for Jebel Tays modified after Fryer (2000). Top image represents the highly faulted base of the overriding plate at the base of the trench in a forearc setting. Entrained water and dehydration reactions serpentinise the upper mantle forming serpentinite mud that flows up fault conduits. Evidence from the IBM arc shows that many of the horst and graben structures are actually large mantle blocks and lower crustal intrusives.

11.1.42 Tectonic Model 1

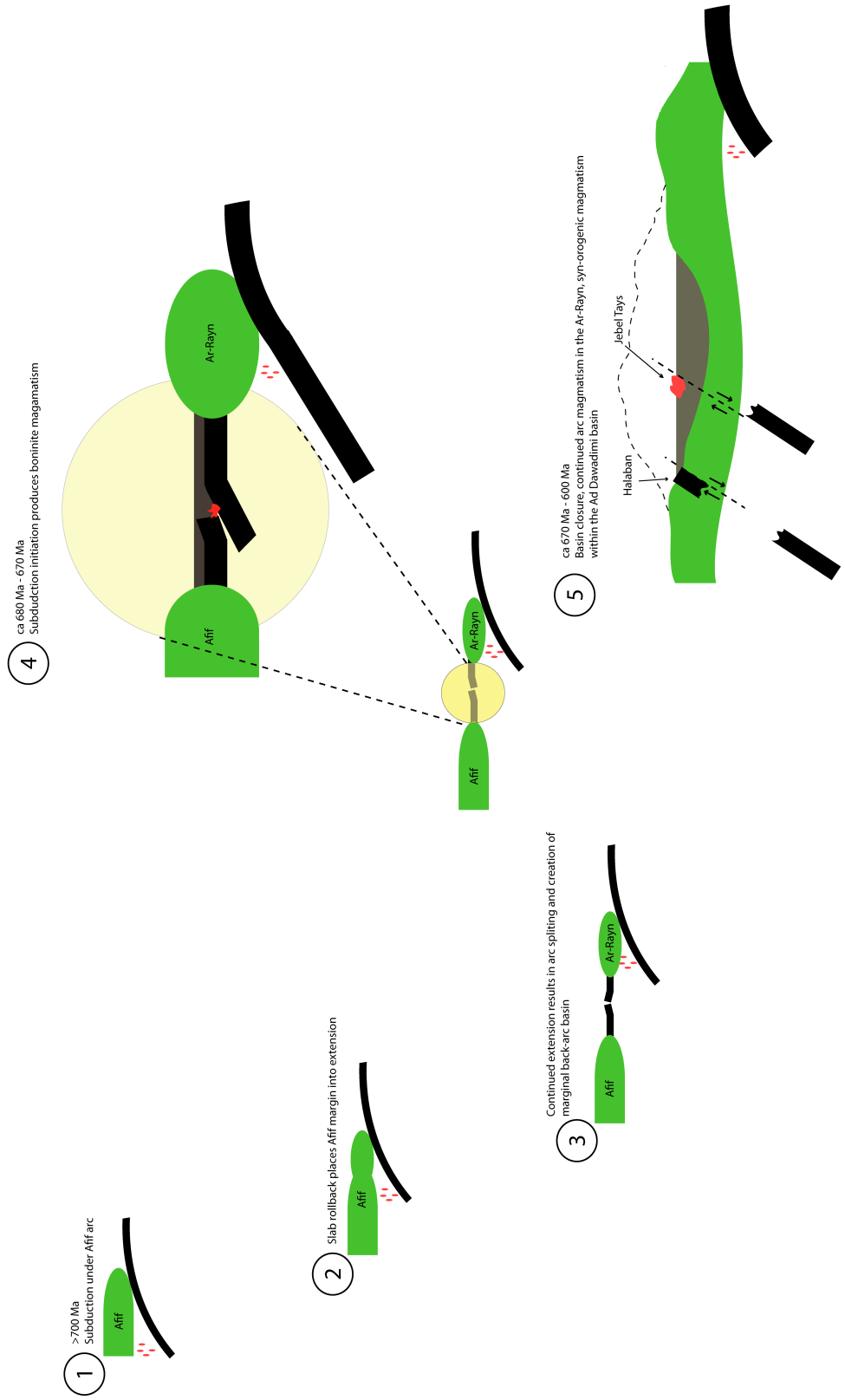

Figure 42. Tectonic model for Jebel Tays and the Ad Dawadimi basin based on arc-splitting and back-arc basin magmatism.

11.1.43 Tectonic Model 2

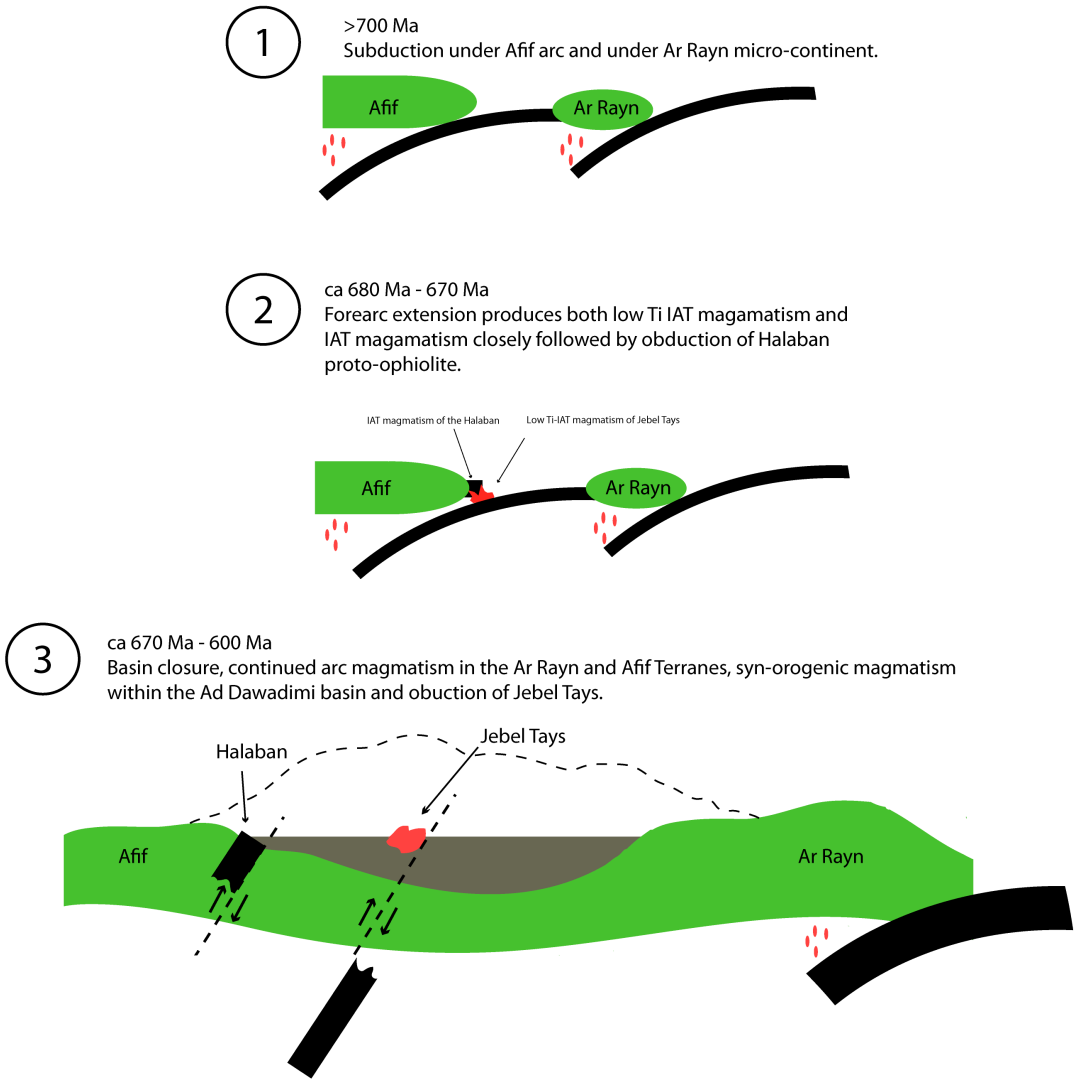

Figure 43. Tectonic model for Jebel Tays and the Ad Dawadimi basin based on an Ar Rayn micro-continent.